Energy Measurement and Strategy for a Trigger of Ultra High Energy Cosmic Rays Measured with Radio Technique at the Pierre Auger Observatory

von

Christian Glaser

Masterarbeit in Physik

vorgelegt der
Fakultät für Mathematik, Informatik und Naturwissenschaften
der
Rheinisch-Westfälischen Technischen Hochschule Aachen

im August 2012

angefertigt am

III. Physikalischen Institut A

Erstgutachter und Betreuer

Prof. Dr. Martin Erdmann
III. Physikalisches Institut A
RWTH Aachen

Zweitgutachter

Prof. Dr. Christopher Wiebusch
III. Physikalisches Institut B
RWTH Aachen

Contents

1 Introduction **1**

2 Cosmic Ray induced Air Showers **3**

2.1 Physics of Ultra High Energy Cosmic Rays 3

2.1.1 Energy Spectrum 3

2.1.2 Composition 6

2.1.3 Sources and Acceleration Mechanism 6

2.2 Extensive Air Showers 8

2.3 Radio Emission from Extensive Air Showers 12

2.3.1 GHz Emission from Extensive Air Showers 14

3 The Auger Engineering Radio Array at the Pierre Auger Observatory **17**

3.1 The Surface Detector 18

3.2 The Fluorescence Detector 19

3.3 Energy Calibration of the Surface Detector 22

3.4 Low Energy Enhancements 23

3.5 The Auger Engineering Radio Array 25

3.5.1 Self-Triggering 27

3.5.2 Calibration 28

4 Reconstruction of Radio Data **31**

4.1 The Software Framework Offline 31

4.1.1 Structure 31

4.1.2 Modules 33

4.2 Signal Processing 35

4.3 Directional Reconstruction 39

4.4 Electric Field Vector 41

5 Data Set and Cuts 43
5.1 Cosmic Ray Radio Events . . . 43

6 Properties of Cosmic Ray Radio Pulses 47
6.1 Definition of a Signal to Noise Ratio . . . 47
6.2 Simulation of Electric Field Traces . . . 50
6.3 Uncertainty of the Electric Field Vector . . . 53
6.3.1 Individual Uncertainty Calculation for Coincident Events . . . 56
6.4 Polarisation of Electric Field . . . 57

7 Energy Measurement 61
7.1 Method . . . 61
7.1.1 Correction for Incoming Direction . . . 61
7.1.2 Definition of Energy Estimator . . . 62
7.2 Uncertainties . . . 63
7.2.1 Energy Estimator . . . 63
7.2.2 Other uncertainties . . . 65
7.3 Energy Calibration . . . 65

8 Trigger Strategy using Wavelet Technique 69
8.1 Continuous Wavelet Transformation . . . 69
8.2 Method . . . 71
8.3 Implementation to Offline . . . 75
8.4 Determination of Background Reduction Rate . . . 76
8.5 Search for Cosmic Rays . . . 79
8.5.1 Geometry Discriminator . . . 79
8.5.2 Cone Cut Algorithm . . . 79
8.5.3 Wavelet Similarity Cut . . . 80

9 Summary 85

A Appendix 87
A.1 Influence of Thunderstorms on Radio Emission . . . 87
A.2 Additional Plots . . . 90

References 93

1. Introduction

Ultra high energy cosmic rays are the most energetic particles and one of the rarest phenomena in our universe. One hundred years after the famous balloon flights of Victor Hess in 1912 on which he found the first evidence for cosmic rays, the study of cosmic rays is still a vivid and interesting field in physics. Thereby, cosmic rays with increasing energies have been explored and particles with energies above 10^{20} eV have been observed so far. This energy is three orders of magnitude higher than the energy achieved by even the largest and most recent particle accelerators on earth[1] and will not be producible on earth in conceivable time.

Although this phenomena has been a major research field for many years, our knowledge about these high energetic particles is still incomplete. "Where do they come from?" or "What processes can accelerate particles to such high energies?" are some of the thrilling questions that still need to be answered.

Ultra high energy cosmic rays are very rare ($\sim$1 particle per century per square kilometre with an energy above 10^{20} eV) but, eventually, after their long journey through the universe, some of them hit the earth resulting in extensive air showers consisting of millions of particles in our atmosphere. The detection of such rare events requires very large detectors. The largest cosmic ray detector - the Pierre Auger Observatory in Argentina - covers an area of 3000 km^2 which is bigger than the size of the German federal state Saarland and, thus, enables the investigation of cosmic rays at the highest energies. The two baseline detector components, the fluorescence and surface detector, are thoroughly calibrated and, therewith, provide a perfect environment for the development and calibration of future detection technologies.

One of the most promising candidates for future cosmic ray detectors is the detection of MHz radio emission from extensive air showers. In principal, it enables a measurement of the shower development - which is a measure of the species of the primary cosmic ray - with a 100% duty cycle. However, technical challenges in the detection and data analysis are still to be solved.

The Auger Engineering Radio Array (AERA) located at the Pierre Auger Observatory is one of the largest experimental efforts in MHz radio detection of cosmic rays. It will and already does essentially contribute to both the theoretical understanding of radio emission from extensive air showers and the technical progress to build and run such a detector.

[1] The LHC will achieve a centre of mass energy of 7+7 TeV for protons which corresponds to an energy of 10^{17}eV in a fix target experiment [1].

One of the challenges of AERA as a self-triggered detector is to identify the cosmic ray signals out of the large number of background events. In this thesis, a new trigger strategy using wavelet technique is developed. We will demonstrate that the background can be reduced significantly with this method and will apply this trigger strategy to our data set to identify cosmic ray signals.

A major quantity of interest is the energy of the cosmic ray. In this thesis, a method to reconstruct the cosmic ray energy using radio technique is elaborated and the information from the well calibrated surface detector of the Pierre Auger Observatory is used to calibrate the developed energy estimator.

2. Cosmic Ray induced Air Showers

Cosmic rays name energetic particles that come from outside our solar system. The energies of cosmic rays can reach 10^{20} eV which is seven orders of magnitudes higher than the energy that can be produced in the largest particle accelerator on earth. When such a cosmic ray hit the earth it will collide with air nucleus and produce a cascade of secondary particles called an air shower.

During their way through the universe, cosmic rays are diffusely deflected by magnetic fields. Thereby, the deflection gets smaller the higher the energy of the cosmic ray is. This makes the study of cosmic rays at the highest energies especially interesting because these cosmic rays are little influenced by magnetic fields and, thus, probably point back to their source.

Within the scope of this thesis we will focus on the cosmic rays at the highest energies, the so-called ultra high energy cosmic rays (UHECRs). In the first section of this chapter we will give a short introduction to the physics of UHECRs. The second section deals with extensive air showers. The third section then focuses on the radio emission from extensive air showers.

2.1 Physics of Ultra High Energy Cosmic Rays

Exactly 100 years ago in 1912 Victor Hess for the first time found an indication that the radiation measured in the air does not originate from the earth [2]. Before his famous balloon flights on which he measured that radiation increases with increasing height, it was believed that the radiation in the atmosphere has its only origin in radioactive elements in the surface of the earth.
Pierre Auger and Werner Kohlhörster found in the 1930s that the measured radiation is mainly due to secondary particles that originate from a single high energy particle [3, 4]. Pierre Auger e.g. placed two particle detectors with a maximum distance of 300 m at the Jungfraujoch (3500 m a.s.l.) and measured several events in coincidence. Thereby, the coincidence rate decreased with increasing distance. He also calculated the energy of the shower to be 10^{15} eV which is impressive because the highest known energies at this time were in the order of MeV coming from nuclear decays.

2.1.1 Energy Spectrum

The energy spectrum is usually expressed in a differential flux J which is the number of cosmic rays per energy, area, solid angle and time. Figure 2.1 shows the energy

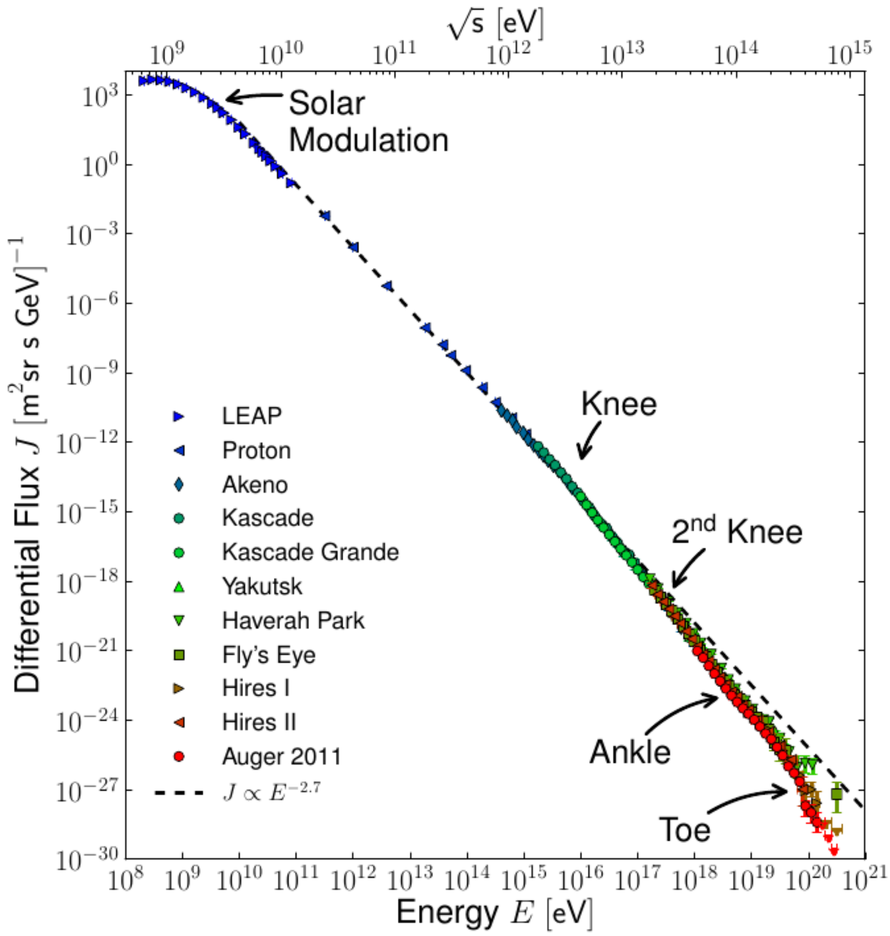

Figure 2.1: Cosmic ray energy spectrum. From Ref. [5].

spectrum of cosmic rays over more than ten orders of magnitude in energy. It is remarkable that most of the spectrum can be expressed with the simple power law:

$$J \propto E^{-\gamma}\,, \quad \text{with } \gamma = 2.7\,. \tag{2.1}$$

This means that the cosmic ray flux drops approximately by a factor of 1000 per energy decade. This steep decrease of the cosmic ray flux requires different detection techniques for different energy ranges. Thus, cosmic rays with energies up to $\sim 10^{14}$ eV can be measured directly with balloon experiments at the top of the atmosphere [6] or spaceborne detectors like the PAMELA satellite [7] or the AMS-2 detector at the International Space Station [8].
Because of the low rate of cosmic rays at higher energies and the limited size of balloon or spaceborne detectors, the detection of high energy cosmic rays has to rely on the indirect measurement of cosmic ray induced air showers on ground level. As cosmic rays become rarer at higher energies, detectors have to cover large areas to measure high energy cosmic rays at a reasonable time. E.g. the cosmic ray flux for energies above 10^{20} eV is only one cosmic ray per square kilometre and century.

A closer inspection of figure 2.1 shows that the slope of the cosmic ray spectrum exhibits some features. At a few times 10^{15} eV - the so-called knee - the cosmic ray

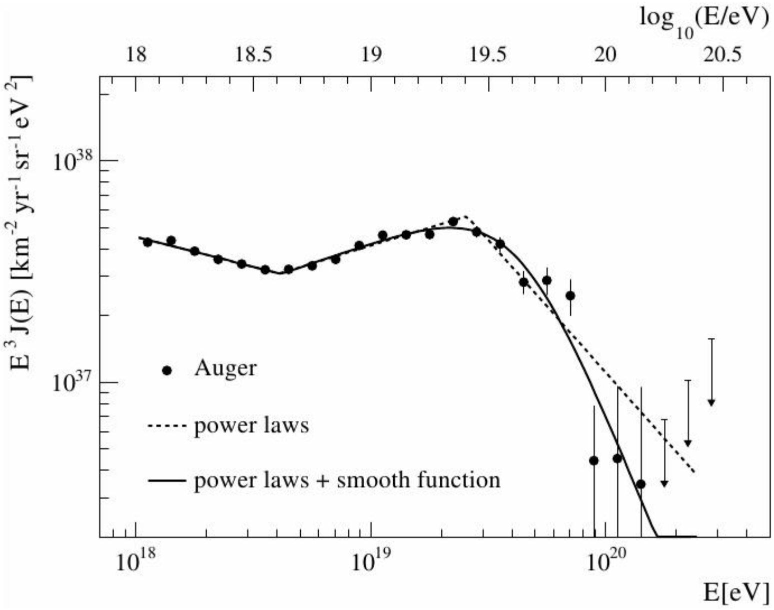

Figure 2.2: Latest auger energy spectrum. The cosmic ray flux is multiplied with the cosmic ray energy cubed to emphasize the change of the slope. From Ref. [10].

spectrum steepens to a spectral index of $\gamma \approx 3.1$. At the "second knee", the spectrum shows an additional slight steepening. The exact reason for the "knee" is uncertain. A possible explanation is a change in the source spectrum (i.e. a superposition of different sources with different spectra).
Another possible interpretation of this feature is a change in the primary mass composition. At some energy, the charged particles are not anymore confined by galactic magnetic fields. Thus, protons start to leak out of the galaxy followed by heavier elements[1] [9, p. 13].

At even higher energies, the cosmic ray spectrum exhibits further features. Figure 2.2 shows the latest energy spectrum measured by the Pierre Auger Observatory. Note that the cosmic ray flux is multiplied with E^3 to emphasize the change of the slope. At $4{\cdot}10^{18}$ eV (the ankle) the spectrum flattens back to a spectral index of $\gamma \approx 2.7$. At an energy of $2.6{\cdot}10^{19}$ eV - the so-called toe - the spectrum drops rapidly.

The change of the slope at the ankle is believed to be due to an extragalactic contribution which becomes dominant at these energies. The rapid drop-off of the spectrum can have two different explanations. The first is the Greisen-Zatsepin-Kuzmin (GZK) cutoff [11, 12]. This is a cutoff of the cosmic ray flux because of interactions with the cosmic microwave background and was already predicted in the 1960s. Protons mainly loose energy by pion production via a $\Delta^+(1232)$ resonance [13] and nuclei decay due to photodisintegration [14]. Independent on the initially energy, after a propagation length of $\sim$100 Mpc the cosmic ray energy drops below 10^{20} eV [15]. This implicates that cosmic rays at the highest energies ($E > 10^{20}$ eV) must originate from relatively close sources.

[1]The Lorentz force is proportional to the charge of the particle. Thus, protons are less influenced by magnetic fields than heavier elements.

However, another possible interpretation is just a change in the injection spectrum of cosmic ray sources.

2.1.2 Composition

The chemical composition of cosmic rays in the energy range between several GeV and a few 100 TeV is well known because the particles can be detected in direct measurements. The cosmic rays are composed of 79% protons, 15% helium and a small fraction of other, heavier elements. Thereby, the fraction of heavier elements decreases with increasing mass [16]. The amount of leptons is suppressed due to energy loss by synchrotron radiation in the galactic magnetic fields.

A measurement of the composition at higher energies is difficult because cosmic rays can only be measured indirectly. One has to draw conclusions from the air shower development on the mass of the primary particle. Different primary particles show indeed a different shower development but the fluctuations, mainly due to the hadronic interactions, are huge. Thus, for instance, a proton initiated air shower could look like an average iron initiated air shower. Hence, it is not possible to measure the mass of a cosmic ray on an event-to-event basis but the average mass composition can be determined.

One potential discriminator is the muon component at ground level. Heavier elements produce more high energy muons in the initial hadronic interaction. The Kascade and Kascade-Grande experiments at the Karlsruhe Institute of Technology (KIT) have used this method to study the composition in the energy range between the first and second knee. It is found that the "knee" is due to a steeper light particle spectrum [17, 18]. Furthermore, a steepening in the cosmic ray energy spectrum of heavy primary particles at about $8 \cdot 10^{16}$ eV is observed [19].
This behaviour was expected if the steepening of the energy spectrum at the knee is due to the leakage of protons out of the galaxy. When protons leak out of the galaxy at an energy E_C^p then an element with the charge Z leaks out of the galaxy at an energy $E_C^Z = Z \cdot E_C^p$.

Another discriminator of the mass composition is the measurement of the longitudinal shower development. An air shower initiated by a heavy primary particle reaches its maximum higher in the atmosphere than air showers from light primary particles. Furthermore, the shower to shower fluctuations are less for heavier primary particles. The Pierre Auger Observatory investigates the mass composition at highest energies. It measures the longitudinal shower profile by detecting the fluorescence light that is produced when the shower traverses the atmosphere. The result of this measurement is presented in figure 2.3. A clear trend towards a heavier mass composition at higher cosmic ray energies is observed.

2.1.3 Sources and Acceleration Mechanism

The question of possible sources for ultra high energy cosmic rays is intimately connected with possible acceleration mechanisms. A favoured model is the first order Fermi acceleration [21], which is a modification of the initially proposed process by

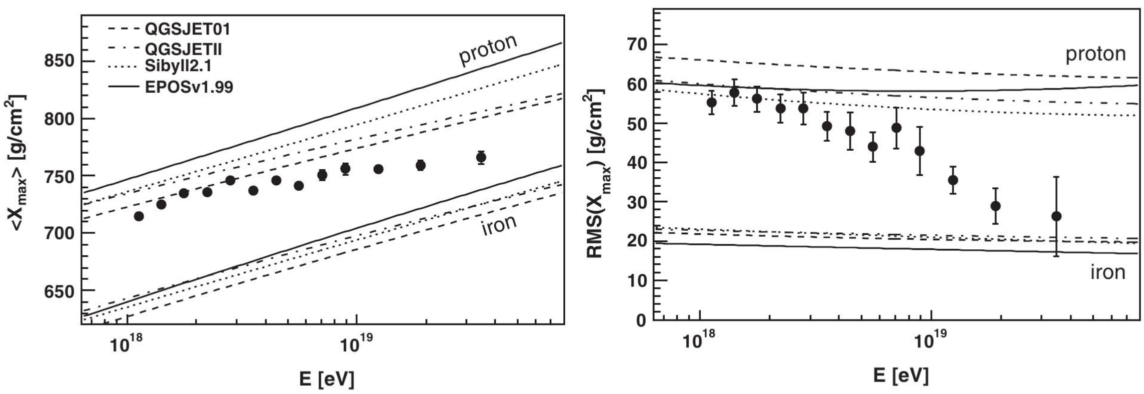

Figure 2.3: The mass composition of cosmic rays measured by the Pierre Auger Observatory (see text for details). From Ref. [20].

E. Fermi in 1949 [22]. In this model, cosmic rays are accelerated by a shock front that move with supersonic speed through a medium. Because the cosmic rays are bend by magnetic fields, the shock front can be passed several times. At each cycle, i.e. a passing from the unshocked region to the shocked region and back, the relative energy gain is constant and proportional to the speed of the shock front:

$$\frac{\Delta E}{E} = \frac{4}{3} \cdot \beta_s \quad , \tag{2.2}$$

where β_s is the speed of the shock front in units of the speed of light c.
At each cycle there is a probability that a particle leaves this process. Thus, the high energy particles are the ones that pass through a lot of cycles.

The maximum achievable energy is determined by the size and the magnetic field of the shocked medium. The greater the energy of the particle, the larger is its Larmor radius

$$r_L = 1.08 \text{ pc } \cdot \frac{E/PeV}{Z \cdot B/\mu G} \quad , \tag{2.3}$$

where E and Z are the energy and the charge number of the particle and B the magnetic field of the medium. Hence, to keep particles with higher energies in the acceleration process, the magnetic field or the size of the acceleration medium have to be large enough. For the maximum achievable energy holds:

$$E_{max} \simeq 10^{18} eV \cdot Z \cdot \beta_s \cdot \left(\frac{R}{kpc}\right)\left(\frac{B}{\mu G}\right) \quad . \tag{2.4}$$

Possible sources can thus be selected by their size and their magnetic fields. In figure 2.4, the famous Hillas plot gives an overview of possible sources for UHECRs. A comprehensive review of possible astrophysical sources can be found in [23].

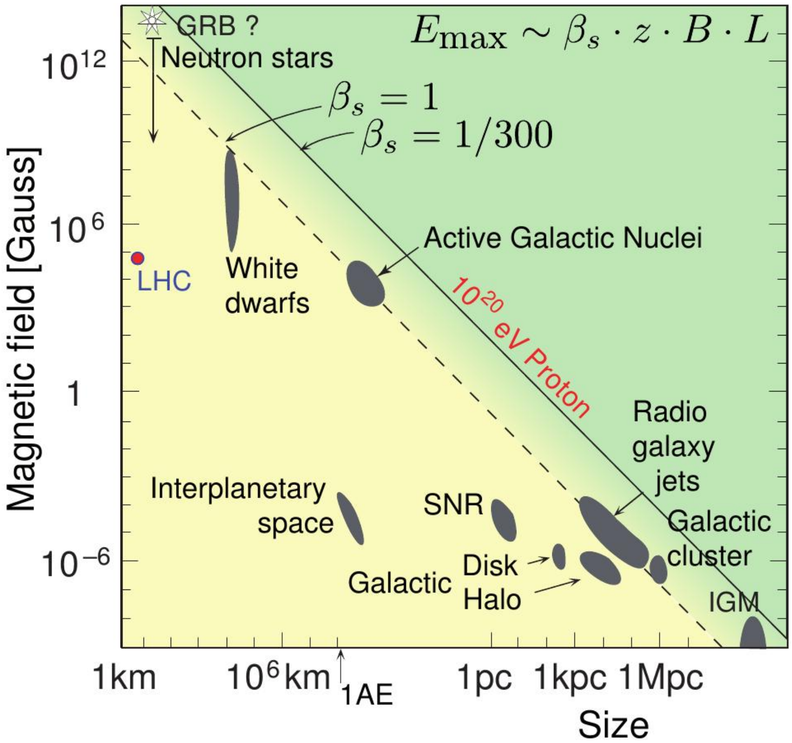

Figure 2.4: Hillas plot of possible sources of UHECRs. Astrophysical sources are inserted by their size and magnetic fields. To accelerate a proton to an energy of 10^{20} eV via shock acceleration with a speed of the shock front of $\beta_s = 1/300\ c$ the source must lie above the diagonal line. From Ref. [5]. Originally published in [24].

2.2 Extensive Air Showers

When an ultra high energy cosmic ray hits the earth, it creates one of the rarest phenomena on earth. The collision of a UHECR with an air nucleus (N_2, O_2, Ar) will initiate an extensive air shower (EAS) in our atmosphere. This is a shower of millions of elementary particles that move with almost the speed of light towards the earth. Such an extensive air shower is accompanied by air Cherenkov, air fluorescence and radio emission which enables the study of the shower development [9].
Within the scope of this thesis, we will focus only on hadron initiated air showers but, in principle, also high energy gamma rays or neutrinos can initiate air showers. The different initial particles lead to a different shower development which enables a differentiation. Gamma rays do not reach the energies of UHECRs. Therefore, the air shower is smaller and can only be detected by its Cherenkov light. Gamma ray astronomy is a vivid field, e.g. a new large detector, the Cherenkov Telescope Array (CTA), is currently under development [25]. Neutrino initiated air showers are supposed to evolve much deeper in the atmosphere but have not been knowingly detected so far [9, p. 26].

Figure 2.5 shows a sketch of an extensive air shower. The hadronic interactions with the air nuclei produce secondary particles that move with almost speed of light in the direction of the primary momentum. The secondary particles interact again with

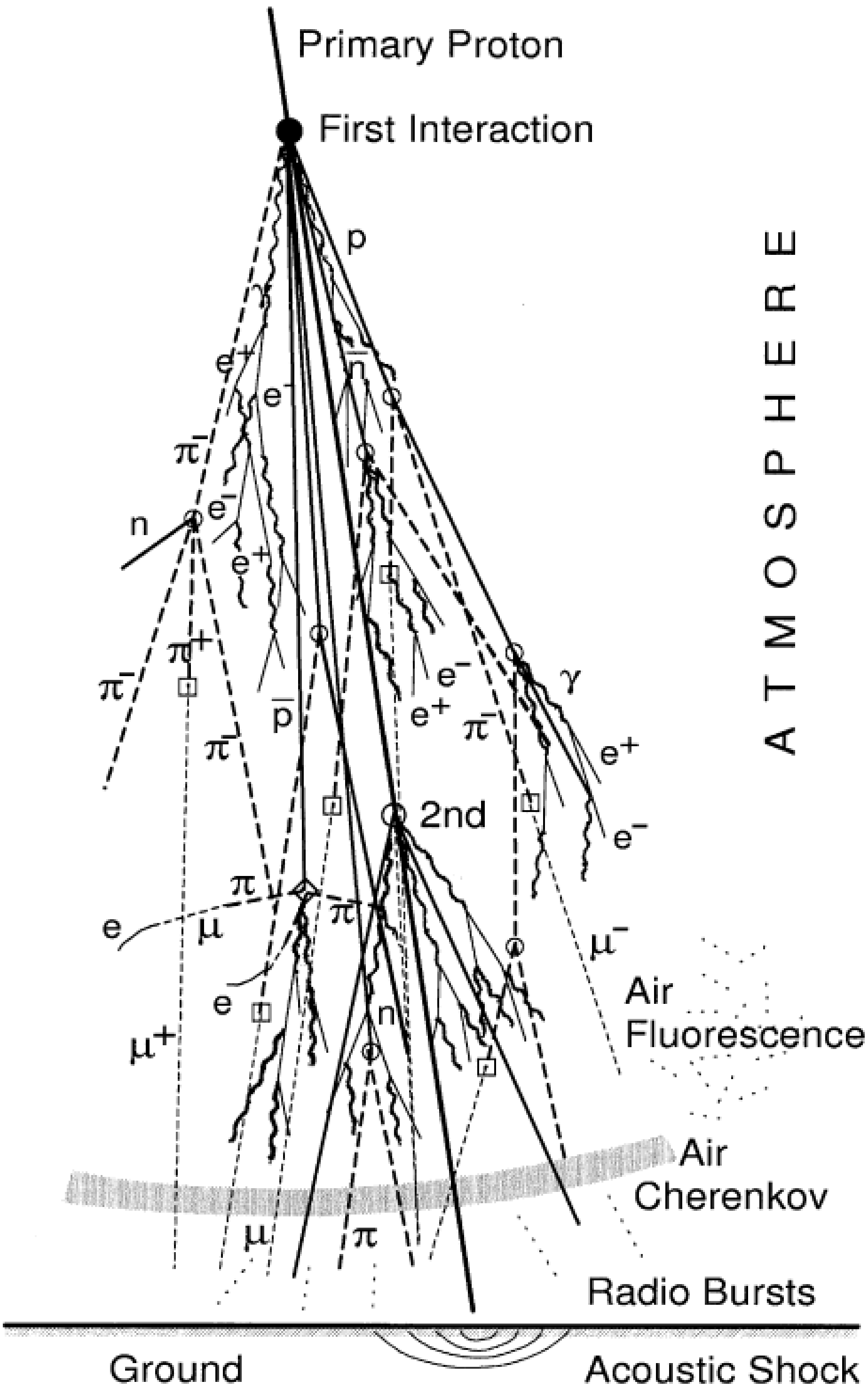

Figure 2.5: Simplified schematic plot of the longitudinal and lateral development of an extensive air shower in the atmosphere, showing the commonly detectable components. On average a vertically incident high energy proton is subject to about 12 interactions before reaching ground level (neutrinos are not shown). Image and Caption from Ref. [9].

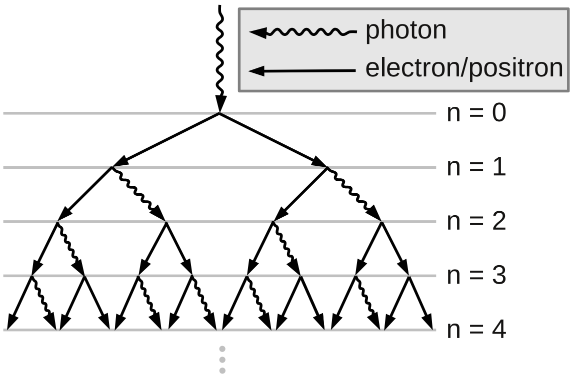

Figure 2.6: Illustration of the Heitler model of air shower development.

air nuclei producing itself new particles as they propagate deeper and deeper into the atmosphere. This is called a hadronic cascade.

Besides the hadronic cascade, also muons and neutrinos are produced mainly by the decay of charged pions. Neutrinos remain undetected in all current UHECR observatories. The "invisible" energy that is taken away by the neutrinos has to be considered in reconstructing the total energy of the air shower

The decay of neutral pions and, to a smaller extend, the decay of muons open a channel to electro-magnetic cascades. Thereby, a significant amount of energy is converted from the hadronic cascade into photons and electrons (and positrons) which generate a large number of secondary particles via pair production and bremsstrahlung.

Heitler Model

An electromagnetic cascade can be described most simply by the Heitler model. This model uses the fact that the interaction length for pair production and bremsstrahlung is very similar at high energies. In this model, each photon decays after a distance X_0 into an electron positron pair where the energy is distributed equally to both particles. Each electron and positron will emit a bremsstrahlungs photon with the half of the electron (positron) energy after the distance X_0. The interaction length in air is $X_0 \approx 36.2$ g/cm^2. Such a cascade is illustrated in figure 2.6.

Thus, after each interaction length X_0 the number of particles doubles. The number of particles after n interaction lengths X_0 is given by $N = 2^n$ where the energy of each particle is $E_n = E_0/2^n$ (E_0 is the energy of the primary particle). The cascade will evolve until the energy E_n is fallen under a critical energy E_{crit} where no further e^+-e^- production or bremsstrahlung is possible. The critical energy of $\sim$100 MeV is the energy where bremsstrahlung becomes the dominant energy loss process in air. Hence, the shower maximum is given by

$$n_{max} = \frac{ln\left(\frac{E_0}{E_{crit}}\right)}{ln(2)} \tag{2.5}$$

and the total number of particles in the shower maximum is

$$N_{max} = 2^{n_{max}} = \frac{E_0}{E_{crit}} \quad . \tag{2.6}$$

Even though this is a simplified model, the correct proportionalities are obtained. A realistic modelling of an electro-magnetic cascade shows that the maximum number of particles is proportional to the energy of the primary particle and the depth of the shower scales with $ln(E_0)$.

Longitudinal Profile

The longitudinal shower development can be studied by measuring the fluorescence light which accompanies the air shower. The charged particles excite nitrogen molecules when traversing through the atmosphere. When the nitrogen molecules de-excite, fluorescence light between ~300 nm and ~430 nm is emitted isotropically and the observed intensity is proportional to the number of particles in the shower front. Because of the omnidirectional emission, the intensity observed on ground is very low. Hence, only air showers with energies above 10^{17} eV can be detected with this method.

The longitudinal profile can be described with the Gaisser-Hillas function [26]

$$f_{GH}(X) = dE/dX_{max} \left(\frac{X - X_0}{X_{max} - X_0} \right)^{\frac{X_{max}-X_0}{\lambda}} \cdot e^{\frac{X_{max}-X}{\lambda}} \quad , \tag{2.7}$$

where X is the slant depth[2] and X_{max} the position of the shower maximum. X_0 and λ characterize the shape of the function. Note that here X_0 is not the interaction length. The integral over this function gives the calorimetric energy of the air shower.

Lateral Profile

The transverse momentum of the scattered particles will lead to a lateral extend of the air shower. This causes a pan-cake form of the shower front as visible in figure 2.7a. The thickness of the shower front is ~1-3 m and broadens with larger radial distance. The broadening is caused by the fact that at larger radial distances the energy per particle is lower and that the fluctuations of the free path length rise with lower energy. For very large air showers a slight curvature is observed.
Figure 2.7b shows that all particles of the air shower arrive within a few nano seconds with respect to the shower tangent plane. The tail is almost exclusively due to low energetic particles.

The lateral profile can be described by the Nishimura-Kamata-Greisen (NKG) formula [27] [28]

$$S(r) \propto \left(\frac{r}{r_0} \right)^{-\alpha} \left(1 + \frac{r}{r_0} \right)^{-(\eta-\alpha)} \quad , \tag{2.8}$$

where $S(r)$ is the particle density on the ground, r is the distance to the shower axis and α, r_0 and η has to be determined by the measurement.

The charged particles of the air shower can be measured with particle detectors on the ground, so-called surface detectors. A simultaneous measurement of the same air shower at different positions enables the reconstruction of the arrival direction and the energy of the air shower. This is an approved technique and has been used in several air shower experiments [29, 30, 31].

[2] The amount of traversed atmosphere counted from the top of the atmosphere.

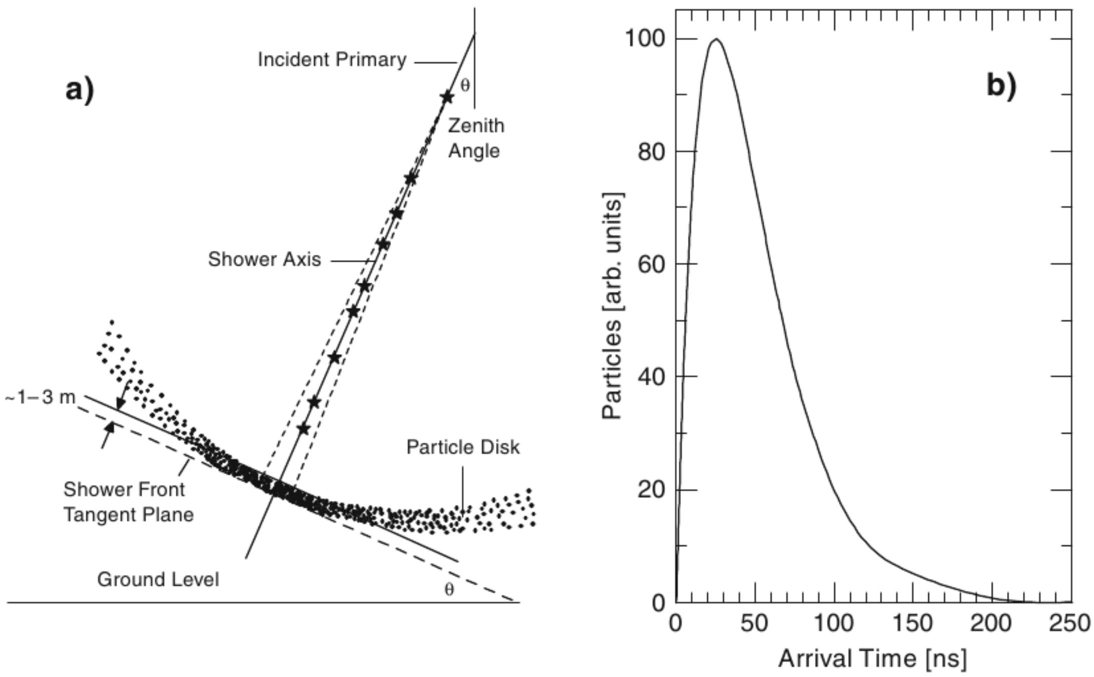

Figure 2.7: (a) Longitudinal profile of an air shower on the left. Shown is the curved shower front and thin particle disk of a moderately inclined shower near ground level impact. (b) The right hand figure shows the approximate time profile of an average shower at ground level, including all particles, with respect to the shower tangent plane. Image and Caption from Ref. [9].

2.3 Radio Emission from Extensive Air Showers

An extensive air shower is accompanied by electro magnetic emission in the MHz regime. The idea to measure radio emission from extensive air showers was first proposed by Jelley in 1958 [32]. A theoretical description was first given by Askaryan in 1962 [33] and shortly after detected by Jelley et. al. in 1964 [34]. A few years later in 1970 Allan et al. performed a more detailed measurement of radio emission from EAS in the MHz regime at the Haverah Park experiment [35]. He first correlated the measured radio amplitude with the cosmic ray energy and found e.g. that the emission strength depends on the angle between the incoming direction of the air shower and the magnetic field of the earth. As signal processing was not so much evolved in those days and the radio regime exhibit strong noise background especially in urban regions, this detection method was abandoned for many years. See [36] for a comprehensive review of the early work.

With new technical capabilities, the measurement of radio emission from extensive air showers experienced a revival in recent years. Experiments such as Lopes [37] at the Kascade detector [30] at the Karlsruhe Institute of Technology or Codalema in France [38] showed that EAS can be measured via their radio emission and that this measurement is sensitive to important shower properties like the incoming direction or the longitudinal shower development and, therefore, the mass of the primary particle [39].

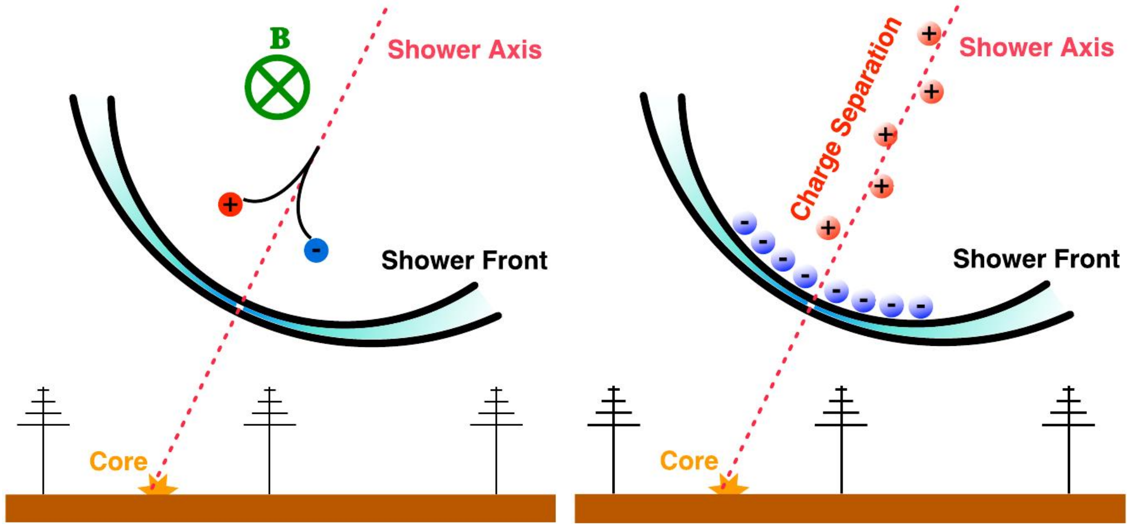

Figure 2.8: Illustration of the two dominant emission processes. (*left*) Geo-magnetic radiation: Electrons and positrons are deflected in the magnetic field of the earth. (*right*) Charge excess: A negative charge excess accumulate in the shower front. See text for details. From Ref. [40].

The measurement of radio emission from extensive air showers has major advantages compared to the detection technique of a fluorescence or surface detector. A radio detector has a duty cycle of almost 100%, such as surface detectors, but is simultaneously sensitive to the longitudinal shower development, such as fluorescence detectors, which can only operate during clear moonless nights. However, a strong noise background and an insufficient theoretical description of the radio emission and lateral signal distribution complicates the reconstruction of air shower properties.

The observed radio emission is due to different emission processes. The most prominent processes are the geo-magnetic emission and the charge excess and are illustrated in figure 2.8. The different emission processes can be distinguished by the polarisation of the radio pulse. The dominant emission process in the frequency range of ∼30 - 80 MHz[3] is the geo-magnetic emission [40]:
The charged particles of an extensive air shower are deflected by the Lorentz force in the magnetic field of the earth when traversing the atmosphere at almost speed of light. In a microscopic point of view, one can think of synchrotron radiation emitted by the charged particles[4]. The radiation of each particle add up coherently and form the radio pulse. This interpretation was first introduced by Falcke and Gorham [41]. On the other hand, in a macroscopic point of view, one can think of a net current flowing in the direction of the Lorentz force, due to the opposite direction of deflection for positive and negative particles. This induction of a transversal current causes the radio emission.

[3]This is the frequency range of the AERA detector.

[4]This is not 100% correct because the electrons and positrons in the shower front are also accelerated, decelerated and deflected due to collisions with air nucleus.

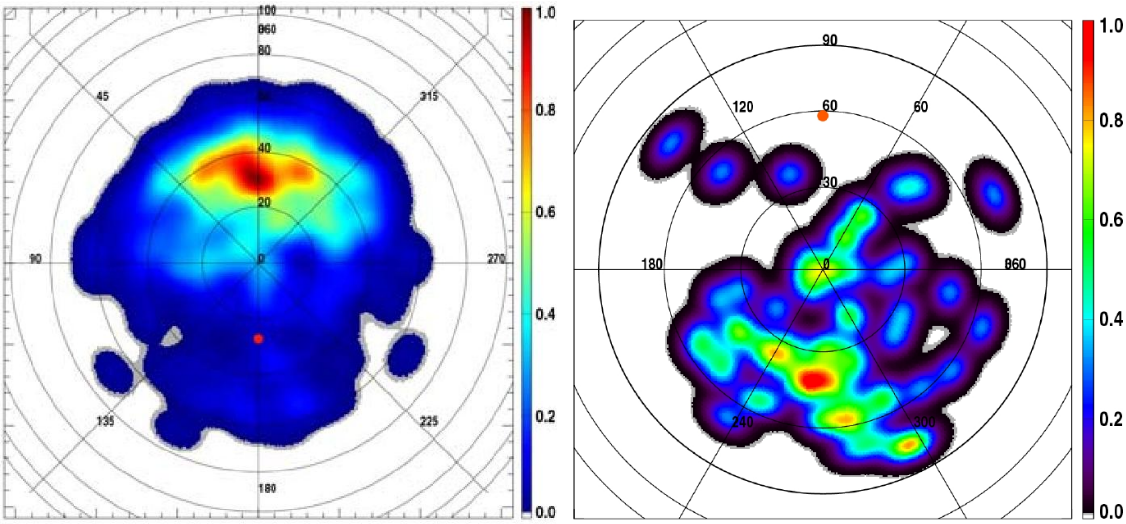

Figure 2.9: North-south asymmetry of cosmic ray events due to the geo-magnetic emission process. (*left*) Measurement at Codalema in France. (*right*) Measurement at the Pierre Auger observatory in Argentina. Each event is smeared with Gaussian window. The red dot indicates the direction of the magnetic field. From Refs. [42] and [43].

This emission process implicates that the emission strength depends on the angle α between the shower axis and the earth's magnetic field:

$$E \propto \sin \alpha \,, \tag{2.9}$$

where E is the electric field strength. Hence, a north-south asymmetry in the arrival directions of cosmic rays is to be be observed. For a detector on the northern hemisphere, more events coming from the north are expected, whereas, for a detector on the southern hemisphere, more events from the south are expected. Measurements at Codalema in France [42] and at the Pierre Auger Observatory in Argentina [43] clearly show this asymmetry (cf. fig. 2.9).

Another emission process is the negative charge excess in the shower front which was already predicted in 1962 by Askaryan [33] (see figure 2.8right for an illustration). Two processes lead to this effect: On the one hand, electrons from air molecules are knocked out when the shower traverses through the atmosphere. On the other hand, positrons annihilate in the shower front. A recent study of the polarisation of radio signals shows that the charge excess contribution is $\sim$12% for an air shower with an incoming direction perpendicular to the magnetic field of the earth [40].

2.3.1 GHz Emission from Extensive Air Showers

Another possible future detection technique for extensive air showers is measuring electro magnetic radiation in the GHz range. This idea was triggered by a measurement by Gorham et. al. in 2004 at the Stanford Linear Accelerator (SLAC) [44]:

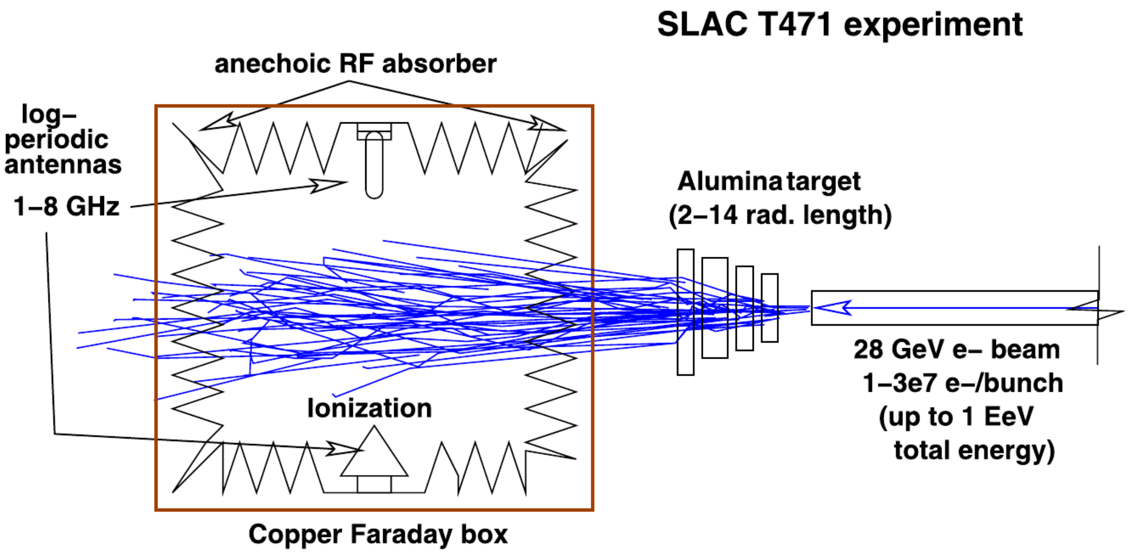

Figure 2.10: Schematic view of the GHz emission experiment at the Stanford Linear Accelerator. An electron beam enters from the left through an alumina target into an anechoic Faraday chamber (see text for details). From Ref. [44].

Figure 2.10 illustrates the test setup. A 28 GeV electron beam with a charge per bunch of $\sim 2\times10^{7}$ eV, resulting in a total shower energy of $\sim 6\times10^{17}$ eV, was collided with a target consisting mainly of alumina (Al_2O_3). A shower will evolve in the target and the shower age can be controlled by the amount of target material. After the target material, the shower enters a 1 m^3 copper anechoic Faraday chamber, filled with air, which is shielded from outside electromagnetic radiation. A strong emission in the 1.5 - 6 GHz band was observed that is not due to transition or radio Cherenkov radiation. Thereby, the emission strength depends on the shower depth (i.e. the amount of target material). Furthermore, a quadratic scaling of the microwave energy with the beam energy is observed.

The established explanation for the observed radiation is Molecular Bremsstrahlung Radiation (MBR). The air shower creates a weakly ionized plasma and these low energy electrons ($E_e \sim 10\,eV$) radiate bremsstrahlungs photons by interaction with the air molecules.
If MBR would be the dominant emission process, detecting GHz radiation would be a great opportunity. The MBR is isotropic, thus, the longitudinal shower development can be observed exactly as with fluorescence telescopes. Furthermore, the atmosphere is almost transparent for GHz radiation and this frequency range has very little noise background resulting in a possible duty cycle of 100% [45].

The SLAC measurement triggered many experimental efforts to verify GHz emission from cosmic ray induced air showers. AMBER first located in Hawaii and now at the PAO, EASIER also at the PAO [46] and CROME in Karlsruhe [47] are just a few currently run experiments. Some of them have indeed detected GHz emission accompanying an extensive air shower, but it remains unclear which physical process causes the observed GHz emission. Another explanation, besides MBR, would be

Cherenkov radiation. This effect implicates that the radiation can only be observed along the Cherenkov ring on ground. Hence, a measurement of the longitudinal shower development would not be possible. This explanation is supported by recent results from the CROME experiment [48]. However, current experimental results are too few to make a reliable statement about the origin of GHz radiation from air showers.

3. The Auger Engineering Radio Array at the Pierre Auger Observatory

The Pierre Auger Observatory (PAO) in Argentina is the world's largest detector for ultra high energy cosmic rays. It is located in the province Mendoza near the town Malargüe in the so-called Pampa-Amarilla. This is a sparsely populated flat plateau at 1400 m above see level to the right of the Andes. Downwinds from the Andes with its peaks with heights above 4000 m lead to steady weather conditions. These qualities constitute a perfect environment for the hybrid cosmic ray detection approach of the Pierre Auger Observatory.

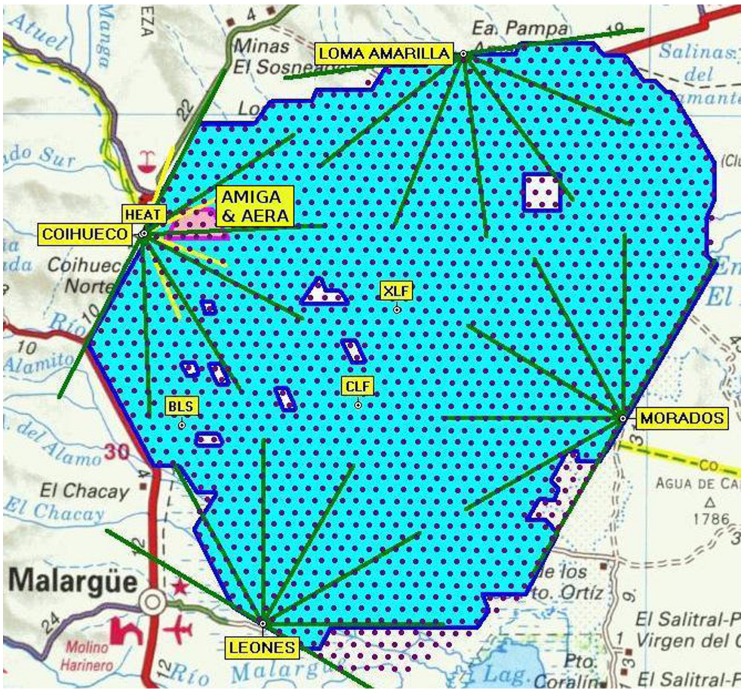

Figure 3.1: Map of the Pierre Auger Observatory. Blue dots are the surface detector stations. All stations within the turquoise background are actually deployed. The green lines indicate the field of view of the fluorescence telescopes that are placed at four positions at the perimeter of the array. From Ref. [49].

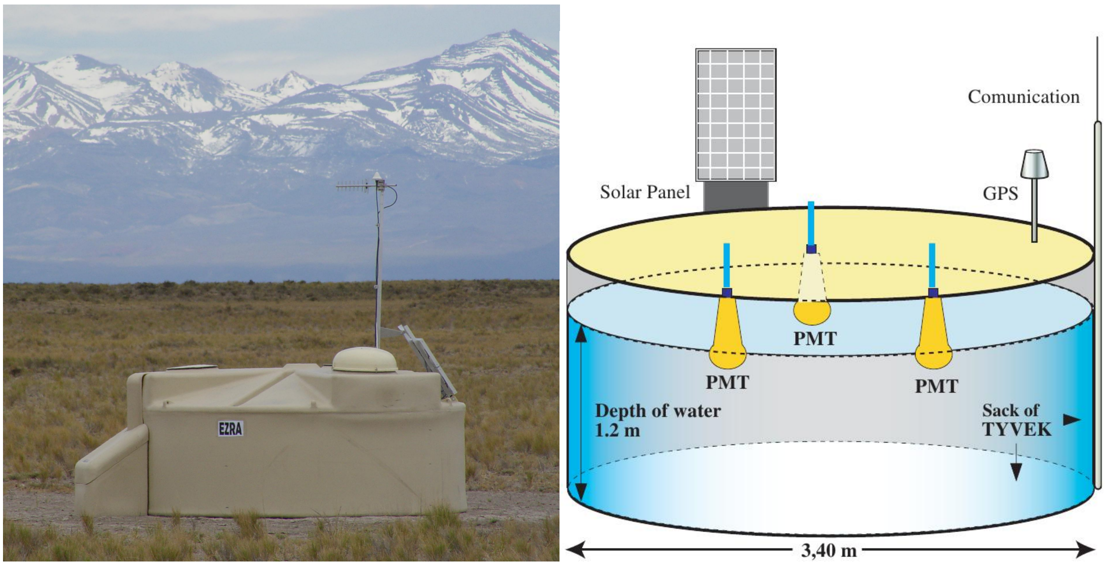

Figure 3.2: (left) Surface detector tank "EZRA" of the Pierre Auger Observatory. The Andes can be seen in the background. (right) Schematic sketch of a SD tank. From Ref. [50].

The Pierre Auger Observatory combines two complementary detection methods. On the one hand, it consists of more than 1600 water Cherenkov tanks - the surface detector (SD) - measuring the particle content of the air shower on ground level. On the other hand, 27 fluorescence telescopes (FD) located at four positions at the edges of the SD array measure the longitudinal development of the air shower. Thus, the advantage of a 100% duty cycle of the surface detector is combined with a calorimetric measurement of the shower development (FD).

3.1 The Surface Detector

Figure 3.2 left shows a picture of one of the water Cherenkov tanks. More than 1600 of these tanks, arranged in a hexagonal grid with 1500 m spacing, form the surface detector. Each SD tank is an autonomous detector station. The schematic view in figure 3.2 right shows that each station is equipped with a solar panel for power supply, a GPS unit for accurate timing and a wireless communication system. Each tank is filled with 12 m^3 pure water.

The charged particles of the air shower are measured via the effect of Cherenkov radiation: When a charged particle passes a dielectric medium (the water inside the SD tanks) at a speed greater than the phase velocity of light in that medium electromagnetic radiation is emitted [51]. The resulting Cherenkov light is detected by three photo multipliers (PMTs) looking downwards into the water. The PMT signals are digitised by 40 MHz 10-bit Flash-Analog to Digital Converters (FADCs).

The dominating background are atmospheric muons[1] that cause a signal in the SD tanks with a frequency of 3 kHz. A sophisticated trigger logic, however, can reduce the trigger rate to reasonable values [52]. Two independent trigger strategies are currently implemented and are described in the following:

The first trigger is a simple signal over threshold trigger which is particularly effective to inclined air showers where the muon component is dominant. All PMTs of one tank have to measure a signal above a certain threshold in coincidence. The threshold is adjusted to achieve a trigger rate of 20 Hz. This limitation of the trigger rate is necessary because of the limited bandwidth of the wireless communication. The single station triggers are forwarded to a central data acquisition (DAQ) and, if at least four spatial connected stations report a signal, the FADC traces are read out and saved in a central DAQ system. With this trigger logic $\sim$1200 events per day are recorded out of which 10% are cosmic rays.

The second trigger is a time over threshold (ToT) trigger. If in two PMTs 13 FADC samples[2] are above threshold within a 3 μs sliding window, a trigger is fired. This trigger is sensitive to nearby low energetic showers and to distant high energetic showers. The signal dispersion is caused by scattering of the electromagnetic component in the first case and the dispersion of particles and photons in the latter case. The ToT triggers that occur with a frequency of 2 Hz are again forwarded to the DAQ and if at least three spatial connected stations report a signal, the event is saved in the central DAQ system. This trigger is extremely pure and most efficient to showers with zenith angles below 60°. Out of the $\sim$1600 recorded events per day 90% are cosmic rays.

The trigger rate can be reduced further by an offline physics trigger taking into account space and time configurations of the detector stations. The surface detector reaches full efficiency for cosmic rays with energies above $3 \cdot 10^{18}$ eV.

The angular resolution depends on the number of stations and energy of the primary particle. Thus, for threefold events with cosmic ray energies below 4 EeV the angular resolution is better than 2.2°. For cosmic ray energies above 10 EeV and more than five triggered stations the angular resolution gets even better than 1° [53].

3.2 The Fluorescence Detector

The SD array is overlooked by 24 fluorescence telescopes measuring the fluorescence light produced by an air shower when traversing through the atmosphere (cf. chapter 2.2). The major advantage of this detection technique is that it allows a direct measurement of the calorimetric energy of an air shower. The restriction, on the other hand, is that the fluorescence light can only be observed in dark moonless to half-moon nights resulting in a duty cycle of 13%.

Each six telescopes form one "eye" that is placed at four positions at the perimeter of the Auger array (fig. 3.1). Figure 3.3 shows one of the FD buildings with closed

[1] These muons are produced by low energy cosmic rays with energies well below the detector threshold.

[2] The width of one FADC sample is 25 ns.

Figure 3.3: One of the four fluorescence telescope buildings.

shutters. Each telescope has a $30° \times 28.6°$ field of view resulting in a 180° field of view in azimuth of the whole "eye". Thus, the complete atmosphere above the SD array can be observed.

Figure 3.4 right shows a schematic view of a fluorescence telescope. Nitrogen fluorescence light enters from the left through a UV-filter into a clean climate controlled building. The light is focussed by a 12 m^2 mirror onto a camera. The camera consists of 440 photo multipliers that are arranged in a 22 x 20 matrix. Each pixel has a field of view of 1.5° x 1.5° resulting in a field of view of 30° in azimuth and 28.6° in zenith for the whole telescope. The amount of light collected by the photo multipliers is

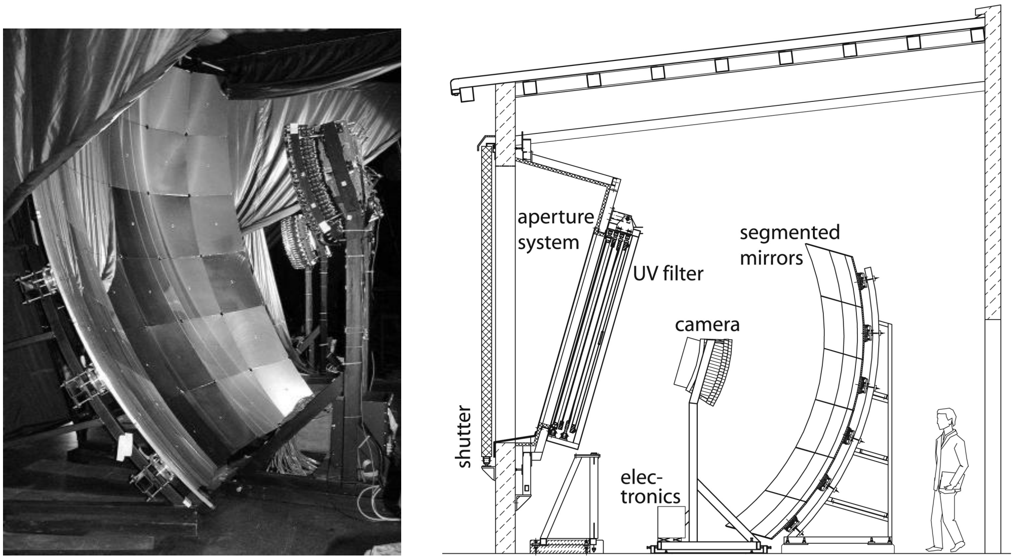

Figure 3.4: (*left*) Mirror and camera of a FD telescope. (*right*) Schematic sketch of a fluorescence telescope. See text for details. From Ref. [54].

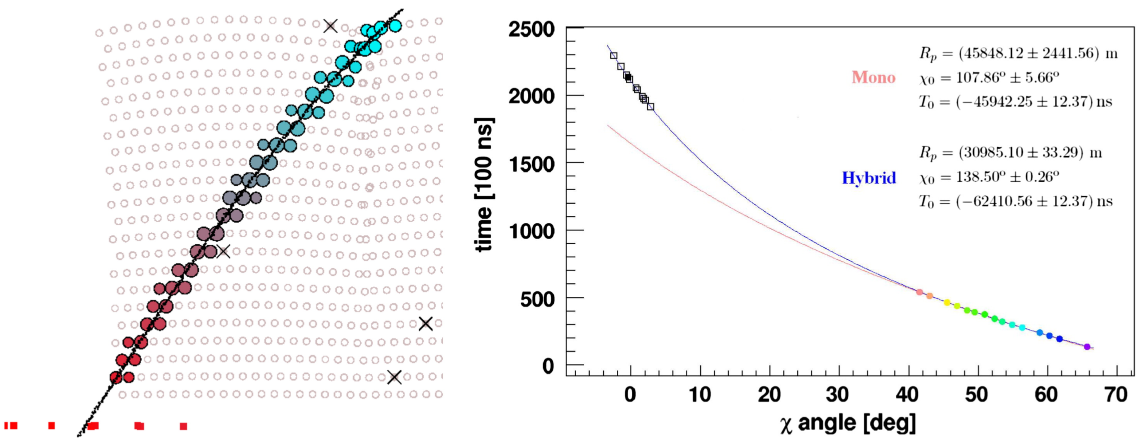

Figure 3.5: *(left)* Light track of a cosmic ray air shower measured by the 440 pixel camera of a fluorescence telescope. Colour coded is the signal time. Black crosses mark pixels with signal that are rejected by the reconstruction algorithm. *(right)* Reconstruction of the geometry of an air shower. χ is the angle of observation within the shower detector plane which is the plane spanned by the shower axis and the FD telescope. The time information of the camera pixels (coloured circles) and of the SD tanks (squares) are shown. The SD station with highest signal is the full square. A hybrid reconstruction (blue line) improves the quality of the reconstruction. From Ref. [54].

digitised and sampled with a frequency of 10 MHz. Finally, a hierarchical trigger logic leads to the detection of cosmic ray air showers.

The best geometry reconstruction can be achieved using not only the timing information of the FD pixels but also the information of the "hottest"[3] SD tank. Thus, the reconstruction profits strongly by the hybrid approach of the Pierre Auger Observatory. Figure 3.5 left shows a light track measured by the camera of a FD telescope. Colour coded is the timing sequence of the triggered pixels. Figure 3.5 right emphasizes the improvement of the geometry reconstruction using the timing information from the surface detector in addition. The observation of the same air showers at different positions leads to a large lever arm resulting in an angular resolution of better than 0.5° [55].

Once the geometry is fixed, the light collected in the individual pixels is converted into the energy deposit at the shower as a function of slant depth. To do so, several corrections have to be applied. First, the measured amount of light has to be corrected for Cherenkov and scattered light (fig. 3.6 left). Second, the attenuation in the atmosphere has to be determined which requires knowledge about the geometry and the current atmospheric conditions. Therefore, the atmosphere above the Auger array is constantly monitored [56].
With the knowledge of the fluorescence yield that can be measured in the lab for different atmospheric conditions [57] [58], the emitted fluorescence light at the shower can be converted into energy deposit as shown in figure 3.6 right. The energy de-

[3]The SD station with the highest signal.

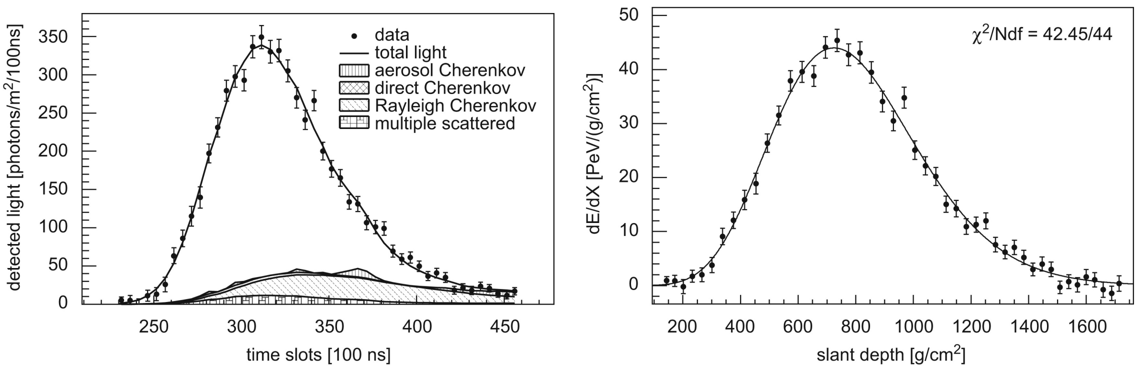

Figure 3.6: (*left*) Example of a light-at-aperture measurement (dots) and reconstructed light sources (hatched areas). (*right*) Energy deposit profile reconstructed from the light at aperture shown in the left figure. The line shows a Gaisser-Hillas fit of the profile. The energy reconstruction for this shower was $3.0 \pm 0.2 \times 10^{19}$ eV. Figures and captions adopted from Ref. [54].

posit profile can be described with a Gaisser-Hillas function [26]. The integral over the energy deposit is the calorimetric energy of the air shower except for about 9% "invisible" energy carried away by neutrinos and high energy muons. The amount of "invisible" energy is determined in Monte Carlo simulations.

The statistical uncertainty on the cosmic ray energy is 7.6% and it is almost constant with energy [59]. The statistical uncertainty depends mainly on the uncertainty of the light flux, the changing amount of invisible energy due to shower to shower fluctuations, atmospheric conditions and the geometry.
The systematic uncertainty on the energy scale is 22%. The main contributions are the uncertainty of the absolute fluorescence yield (14%), systematics in the reconstruction method used to calculate the longitudinal shower profile (10%) and the calibration of the fluorescence telescopes (9%) [59].

3.3 Energy Calibration of the Surface Detector

The independent measurement of the same air shower with two complementary detectors permits a cross calibration. Within the scope of this thesis, the energy calibration of the surface detector is presented roughly.

In general, the cosmic ray energy can be related to the signal strength measured by the surface detector. Figure 3.7 left shows the signal measured in the surface detector tanks plotted versus the lateral distance to the shower axis. The signal is interpolated with a Nishimura-Kamata-Greisen (NKG) [27] [28] function (cf. chapter 2.2). Studies have shown that the signal strength at 1000 m away from the shower axis *S(1000)* is the best estimator for the cosmic ray energy for the current spacing of the SD tanks of 1500 m [60].
The quantity *S(1000)* still comprises a zenith angle dependency because of the different attenuation in the atmosphere. Thus, *S(1000)* is corrected to the signal strength S_{38} the shower would have produced if it had arrived at $\theta = 38°$. The quantity S_{38}

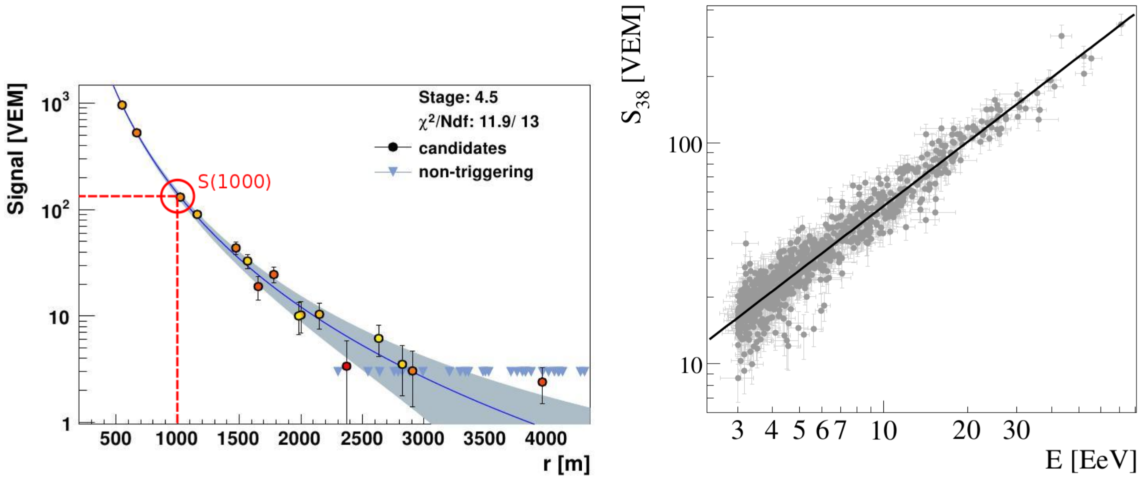

Figure 3.7: (*left*) Lateral signal falloff as measured by the surface detector. The LDF fit takes also the non-triggered stations into account. (*right*) Energy calibration of the surface detector. S_{38} (the signal strength at 1000 m away from the shower axis if the shower would have arrived from 38° zenith) is correlated with the cosmic ray energy measured by FD. Adopted from Ref. [59].

is then correlated with the direct measurement of the cosmic ray energy of the FD. The outcome is the calibration curve shown in figure 3.7 right.
The relative energy resolution (only statistical uncertainty) is determined to 15.8% for energies between 3 EeV and 6 EeV, 13% for energies between 6 EeV and 10 EeV and 12% for energies above 10 EeV. The systematic uncertainty on the energy scale is 22% [59].

3.4 Low Energy Enhancements

The Pierre Auger Observatory has several efforts to extend the energy range down to smaller energies. The energy region from 10^{17} eV to 10^{18} eV is of great interest because here the transition from galactic to extra galactic sources is expected.
Both standard detectors of the PAO (SD, FD) have a low energy extension. The Auger Muons and Infill for the Ground Array (AMIGA) extends the regular SD array with additional Cherenkov tanks with a smaller spacing and muon detectors. The High Elevation Auger Telescopes (HEAT) are three additional fluorescence telescopes with a higher viewing angle of 30° to 60° in zenith. Both extensions are located in the north west of the Auger array (cf. fig 3.1) allowing a hybrid detection also for low energetic showers.

Figure 3.8 shows the three HEAT telescopes placed next to the regular FD site at Coihuecco. As air showers with lower energy evolve higher in the atmosphere, HEAT provides a field of view of larger elevation angles. This is achieved by tilting the whole building that contains the fluorescence detector by 29°. This has the advantage that most of the technology and design of the regular FD can be used. Another advantage of this design is that HEAT can be run in tilted and untilted

Figure 3.8: The three HEAT telescopes in tilted mode with closed shutters. From Ref. [61].

mode. The latter mode allows a cross calibration with the regular FD telescope as the field of view is the same. HEAT is fully commissioned and taking data since September 2009 [61].

The additional infill stations of the AMIGA extension are placed in a hexagonal grid with a spacing of 750 m between the existing tanks and cover an area of 23.5 km^2 (fig. 3.9 left). The water-Cherenkov tanks used for the infill are identical to those of the regular SD. Thus, calibration of the individual stations, trigger strategy, data acquisition and reconstruction methods can be mostly adopted from the approved surface detector. However, the energy reconstruction requires some modifications.

The LDF function which describes the lateral signal falloff has to be modified slightly and the optimal distance for the energy estimator changes. Studies in [10] show that the signal strength at a lateral distance of about 450 m leads to the best energy estimator. This requires also a new energy calibration with the fluorescence detector. A detailed study of the systematic uncertainties is currently under development.

Figure 3.9 right shows that the infill array reaches full efficiency at $3 \cdot 10^{17}$ eV and, thus, reduces the energy threshold of the PAO by one order of magnitude.
A second infill extension with a spacing of 433 m is planned. As the cosmic ray flux increases rapidly with decreasing energy the second extension will cover an area of only 5.9 km^2. This will reduce the energy threshold further to 10^{17} eV.

Each infill station should be accompanied with a muon detector. Measuring the muon component gives important information about the air shower development and, thus, information about the particle species of the cosmic ray (cf. chapter 2.1.2). Each muon detector is a 30 m^2 scintillator buried at a depth of 2.3 m. Only muons with energies above 1 GeV can traverse the soil and reach the scintillator. Three prototype 10 m^2 detectors are currently in operation. The deployment of a complete test cell consisting of seven detectors below the associated infill stations is in progress.

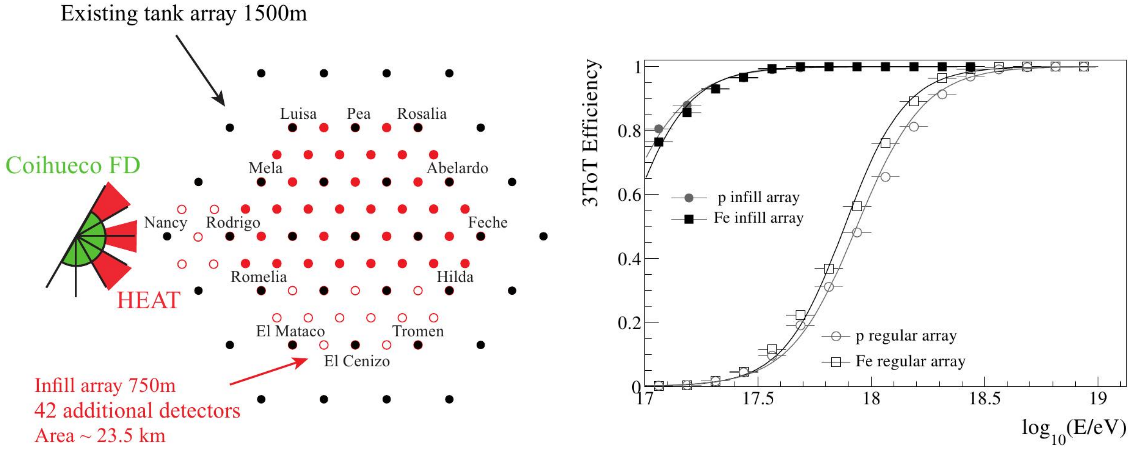

Figure 3.9: (*left*) Map of the SD infill array. The black dots are the regular SD tanks. The red dots are the infill SD stations with a spacing of 750 m. The red circles are the infill stations that had not been deployed at the time of this publication. (*right)* Simulated trigger efficiency for the regular and infill SD array. From Ref. [61].

3.5 The Auger Engineering Radio Array

The Auger Engineering Radio Array (AERA) is one of the world largest efforts in the detection of UHECRs with MHz radio technique. AERA is located in the north-west of the Pierre Auger Observatory (cf. fig. 3.1) within the low energy extension AMIGA and in the field of view of HEAT. AERA currently consists of 21 autonomous self-triggered stations arranged in a triangular grid with a spacing of 150 m. A further extension with in total 150 stations is planned for the end of this year (fig. 3.10). With this size of the radio array, several thousand cosmic ray events per year with energies above 10^{17} eV are expected [49]. The first stage of expansion with its 21 stations is successfully operating since April 2011.

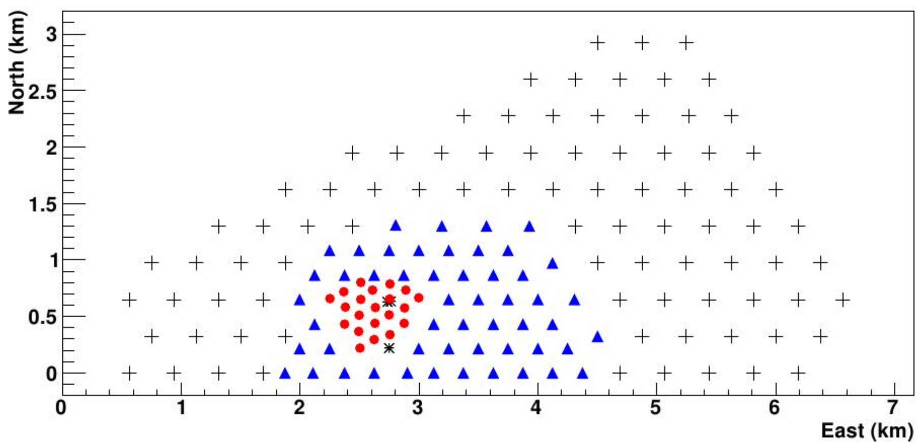

Figure 3.10: Map of AERA. Red dots are the 21 currently deployed stations with a spacing of 150 m. Blue triangles and black crosses are the planned stage of extension with 250 m and 375 m spacing respectively. From Ref. [62].

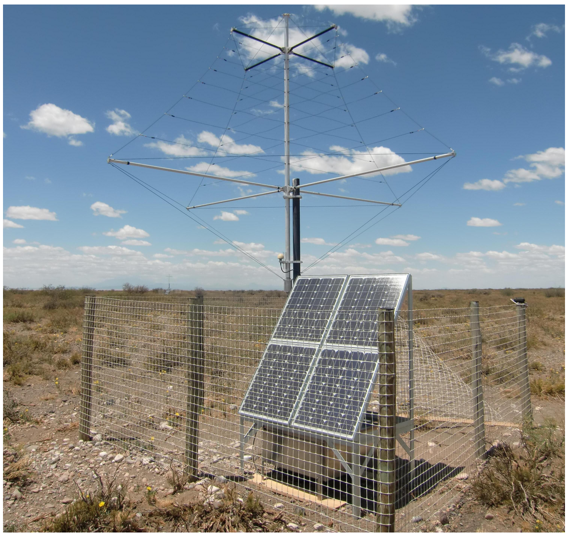


Figure 3.11: (*left*) AERA radio station. (*right*) Central Radio Station: This container hosts the central data acquisition system.

Figure 3.11 left shows a picture of one of the AERA radio stations. Each radio station consists of two log periodic dipole antennas (LPDA) integrated in one mechanical structure which have been developed and build at RWTH Aachen university [63]. As depicted in figure 3.12 left, one antenna is east-west and the other north-south polarised according to magnetic north. The alignment was carried out very precisely and achieved a precision of better than 1° [64].
The LPDA is particular suitable for the detection of UHECRs. It is mostly sensitive to frequencies from 30 MHz to 80 MHz which is a relative radio quiet region between the short-wave and the FM bands. Furthermore, the galactic radio background decreases with higher frequencies and is sufficiently low above 30 MHz. Its directional gain is such that it is most sensitive to upward directions. The sensitivity towards the ground is low which minimizes the dependency of the antenna characteristics to the specific ground conditions[4]. A detailed study of suitable antenna types for the MHz radio detection performed with respect to AERA can be found in [65].

Each radio station forms an autonomous detector. Thus, it is equipped with solar power supply and a GPS antenna for precise timing. The station electronics are housed in a “dust-save” metal box and are shielded by a radio-frequency tight chamber to prevent triggering on self-made noise. The antenna stations are connected by an optical fibre to a so-called central radio station (CRS) shown in figure 3.11 right. The CRS houses the central data acquisition (DAQ) and comprises a wireless link to one of the FD telescopes. Thus, a communication with the DAQ system of SD and FD is possible which enables a combined trigger logic or a remote access through internet.

As AERA is an engineering array, different hardware is tested. For instance, two different versions of the station electronics are developed and currently deployed. One

[4]The reflectivity of the ground changes for example with humidity

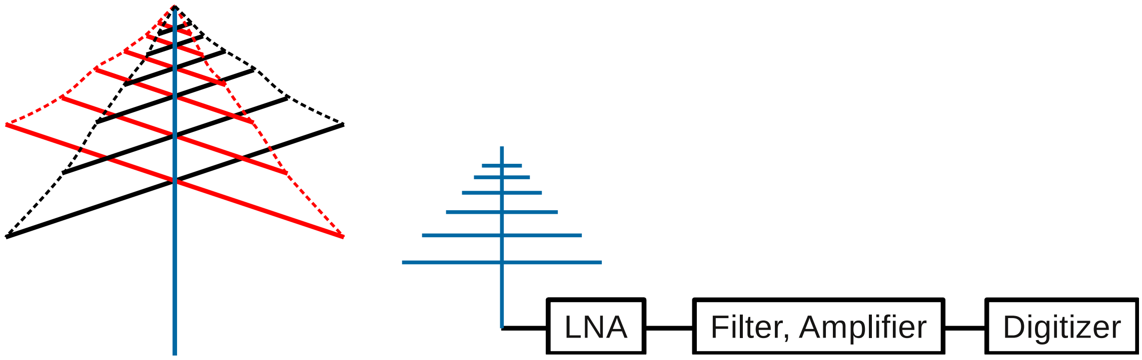

Figure 3.12: (left) Each AERA radio station consists of two antennas (east-west and north-south polarised. (right) Signal chain of a radio station.

version of the station electronics is developed by the Radboud University Nijmegen and is referred to as “Dutch” electronics. The other one is developed by the Karlsruhe Institute of Technology (KIT) and Bergische Universität Wuppertal (BUW) and is referred to as “KIT/BUW” electronics. The most important innovation of the latter version is the implementation of an external trigger by the surface detector. As in this thesis only data taken with the “Dutch” electronics is analysed, the following description of the detector will describe only the details of this electronic version. However, the exact specifications differ only slightly so that in general the description holds also for the “KIT/BUW” electronics.

Figure 3.12 right shows the signal chain of a radio station. The measured signal is amplified by a low noise amplifier (LNA) with integrated band pass filter [66] [67]. Then, the signal passes through band-pass filters and is amplified in a second stage. Finally, the signal is digitised by a 12-bit analogue to digital converter (ADC) with a sampling frequency of 200 MHz.

3.5.1 Self-Triggering

Even in the relatively radio quite location of the AERA detector, various transient noise sources are omnipresent. Thus, a simple threshold trigger is insufficient. A field programmable gate array (FPGA), which is part of the station electronics, allows the implementation of advanced trigger algorithms. The development of a pure and efficient trigger is very challenging and still under development. However, trigger strategies made good progress in the recent year:

Before the actual trigger, narrow band noise sources are filtered out. Different techniques such as a notch filter, a median filter [68] or a FIR filter based on linear prediction [69] are implemented for the FPGA. The filtering leads to a significant improvement of the signal to noise ratio (cf. fig. 4.4). Note that the filtered signal is only used for triggering but the unfiltered signal is saved for offline analysis.

The actual trigger logic on station level is visualized in figure 3.13. In simple words, the station trigger does the following: The signal has to cross some threshold T1. Before that threshold crossing no other T1 crossing must occur. After the T1 threshold crossing only a limited number of T2 threshold crossing may occur. The value

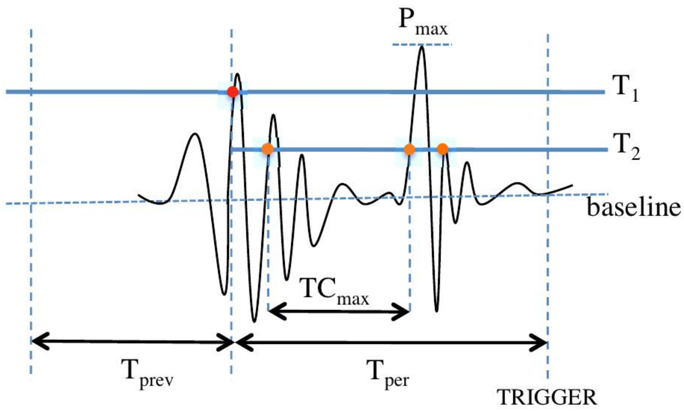

Figure 3.13: Illustration of trigger logic. See text for details. From Ref. [68].

of the thresholds is dynamically adjusted depending on the actual noise level. A detailed description of the trigger logic can be found in [68].

Another technique to veto man-made radio-frequency interference (RFI) is the periodic filtering. A detailed survey of the noise sources at the AERA site has shown that most RFI pulses come periodically with 50 Hz or multiples of this frequency. As probable RFI sources, a power line pole and a transformer station is recognised [70]. These sources also explain the periodicity of the RFI pulses as the power grid frequency of Argentina is 50 Hz.

The station triggers (including a GPS time stamp) are forwarded to the central radio station. If at least three spatial and time coincident station triggers occur, an event trigger is formed.
At this stage the background can be reduced further by directional filtering. The signal time information of three stations is sufficient to estimate the arrival direction of the observed radio pulse. Unlike cosmic rays, most RFI pulses come from hotspots from the horizon. Thus, a lot of RFI can be vetoed by rejecting signals coming from the horizon or specific directions respectively.

If an event passes all triggers, the DAQ system requests and saves the measured voltage trace from the radio stations. Note that the aforementioned trigger strategies are still under development and the data used in this thesis has been recorded with differing trigger settings.

3.5.2 Calibration

The AERA radio stations are thoroughly calibrated through the entire signal chain. This precise knowledge of the antenna and electronic characteristics enables the reconstruction of the three dimensional electric field which is the major quantity of interest and one of the advantages of AERA.
Thus, each LNA and the station electronics have been measured individually [71]. The measurement of the antenna characteristics is much more challenging why the reconstruction of the electric field is currently based on detailed simulations using

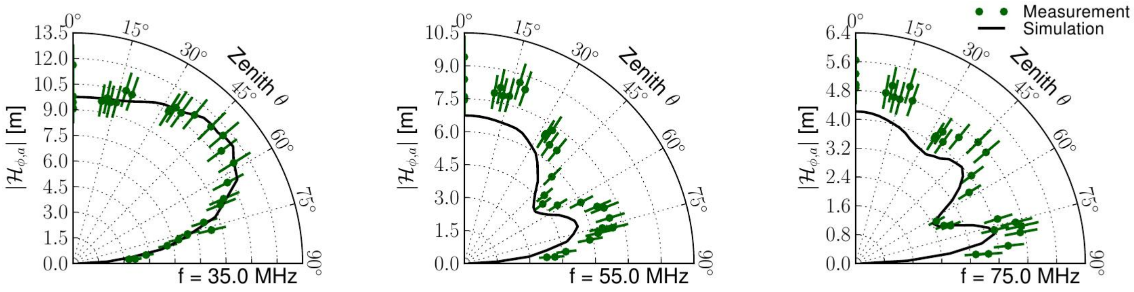

Figure 3.14: Result of the calibration measurement and simulation of the LPDA for three selected frequencies. The vector effective length $\vec{H}$ gives the conversion between the incident electric field strength and the voltage measured at the antenna output terminals and is directly related to the gain of the antenna. From Ref. [65].

the software NEC2 [72]. Several measurements have been performed to cross check the simulation, though [73] [65].

The antenna characteristic can be determined by measuring the transmission between a second already calibrated antenna and the antenna under test (AUT). Thereby, the calibrated antenna is placed at different positions around and above the AUT to measure the directional dependent gain.
The experimental challenge for an antenna calibration measurement is to realize a large distance between the calibrated transmitter and the antenna under test (AUT). A large distance is necessary so that the emitted wave fulfils the plane wave approximation at the AUT. The needed distance depends on the maximal considered wavelength. For AERA this is $\lambda = 10$ m which requires a distance of at least 30 m.

Figure 3.15 shows an overview of the experimental setup. A helium balloon is used to lift up the calibrated biconical transmitting antenna. A rope construction forces the balloon to move on a circle around the antenna and serves for a parallel orientation between both antennas.
Signals with different frequencies are emitted and measured by the AUT using a vector network analyser [74]. The impact of cables is considered in a null calibration. The LNA is included in the measurement but its amplification can afterwards easily be unfolded. Hence, the zenith and frequency dependent gain of the AUT can be measured.

Figure 3.14 shows the result of the measurement for three selected frequencies. The measurement reproduces remarkably good the simulated antenna pattern. For all frequencies and zenith angles, the measurement agrees with the simulations within $\pm 20\%$.

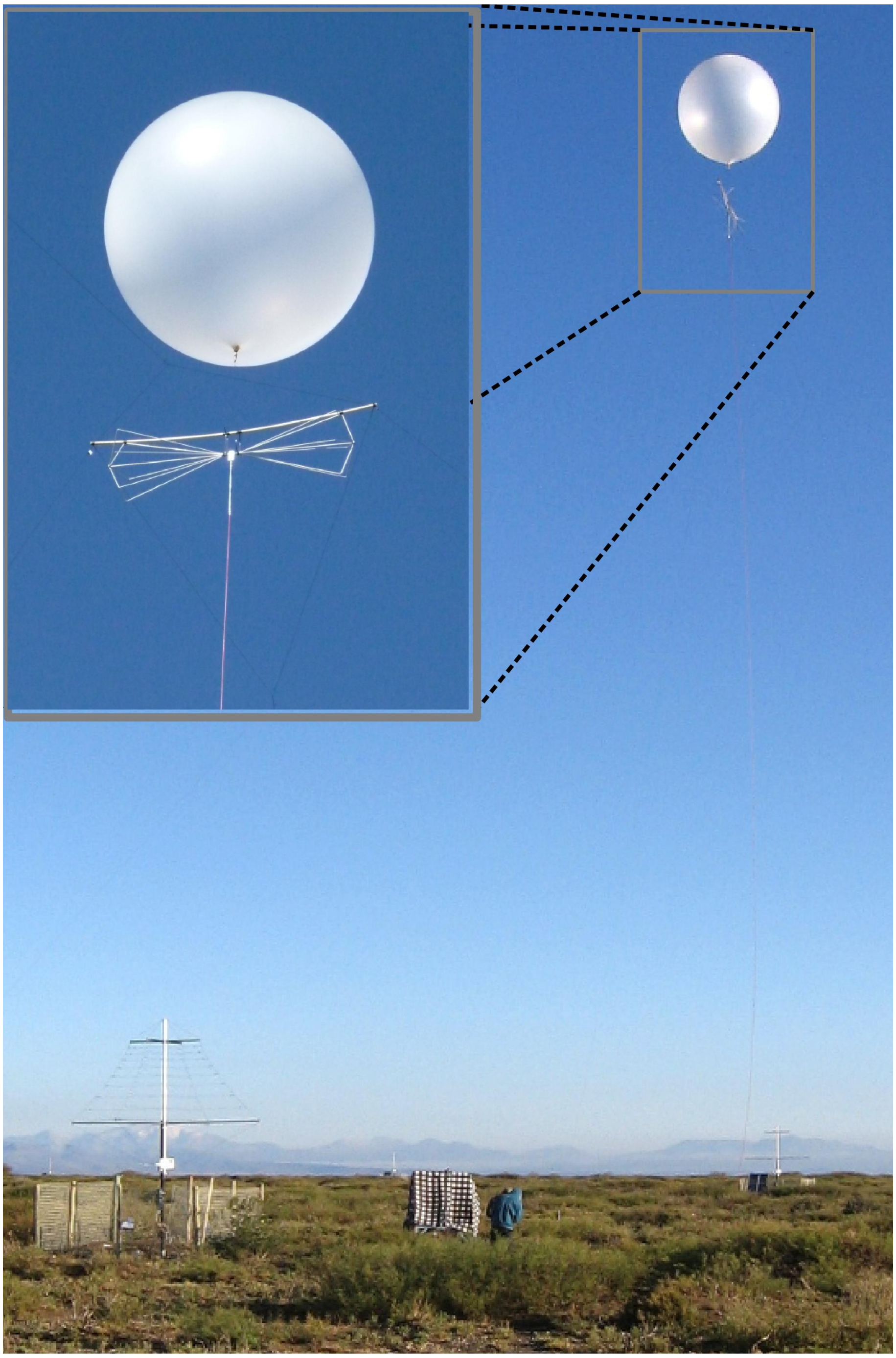

Figure 3.15: Overview of the calibration measurement performed at AERA in Argentina (see text for details). Adapted from Ref. [65].

4. Reconstruction of Radio Data

4.1 The Software Framework Offline

$\overline{\text{Off}}\underline{\text{line}}$ is the modular C++ software framework of the Pierre Auger experiment [75]. It was developed to enable the reconstruction of the fluorescence and surface detector data within one single software framework. It comprises a very flexible structure which makes it possible to extend the software to other detector components such as radio. Hence, in 2010 $\overline{\text{Off}}\underline{\text{line}}$ was extended by a radio part [76].
The following description will mainly focus on the radio part. A comprehensive description for the other detector components can be found in [75].

4.1.1 Structure

The $\overline{\text{Off}}\underline{\text{line}}$ framework consists of three principal parts as depicted in figure 4.1: First, a detector description providing access to configuration and performance data of the detector. Second, an event structure accumulating detected, simulated and reconstructed event information. Third, a collection of data processing modules.

The modules are designed to have no direct interface to each other but relay data to one another through the event structure. This approach serves to separate data from the algorithms and offers a clear modularisation. Hence, different modules can be exchanged easily to test different methods and any reconstruction pipeline can be extended without difficulty by a further reconstruction module.
Furthermore, the differentiation between the well defined event structure, the detector description and the data processing modules permits the reconstruction and analysing of data from different experiments as well as from simulations.

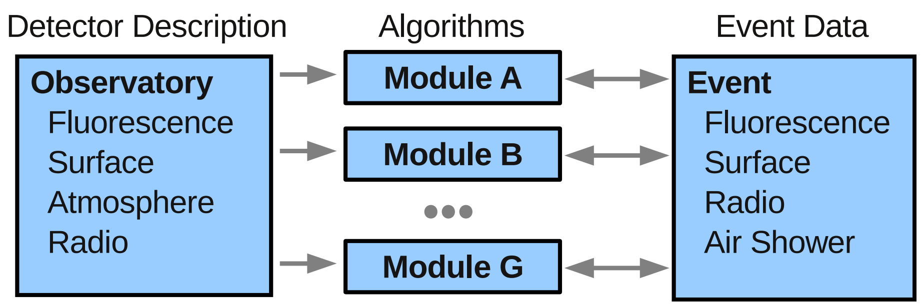

Figure 4.1: The three principal parts of the Offline framework.

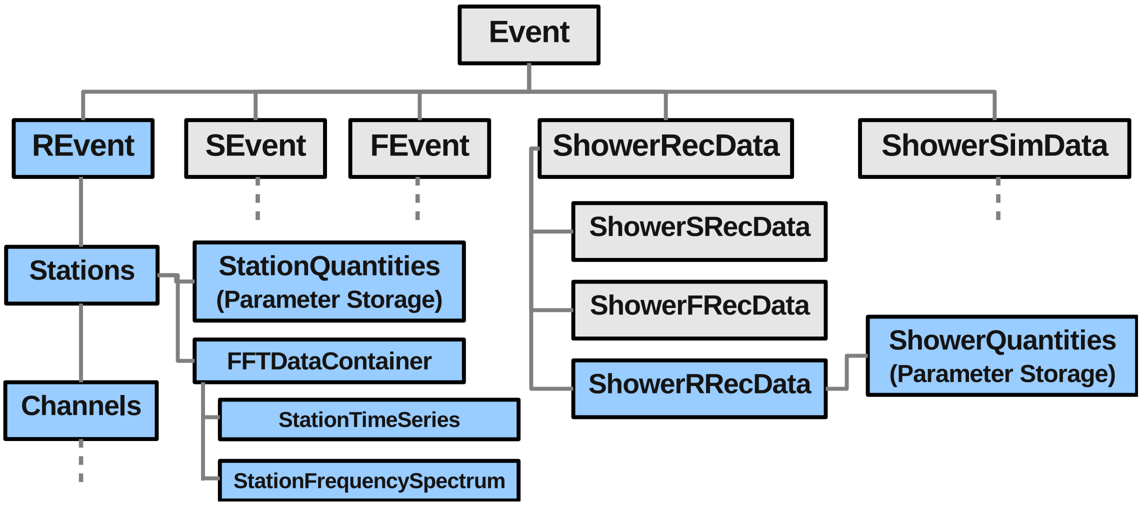

Figure 4.2: Offline Event Data Structure. The elements belonging to the radio part are highlighted in blue.

These three parts are complemented with a variety of foundation and utility classes such as error logging, physics and mathematical manipulations or a geometry package. Thus, for example classes to represent signal traces and utilities for Fourier transformations are available.

Event Structure

Figure 4.2 depicts the event structure that stores all raw, reconstructed and Monte Carlo data. An *Event* consists of an event class for each detector component (SD, FD, Radio), a class for simulated and a class for reconstructed showers.
The radio event class (*REvent*) comprises various *Stations* (the AERA radio stations) which in turn consist of a number of *Channels* (the low and high gain channel of the east-west and north-south polarised antennas).
A *Channel* stores mainly the time series that is recorded at an antenna. A *Station* stores the reconstructed three dimensional electric field trace (*StationTimeSeries*) and reconstructed quantities such as signal to noise ratio, signal amplitude or signal time.

As it is more effective for some algorithms to operate on the frequency spectrum rather than on the time series, the access to the time series and frequency spectrum is implemented through a so-called *FFTDataContainer*. Depending on what is requested and which representation was changed last, a fast Fourier transformation (FFT) is performed on-the-fly.

Parameter Storage

In contrast to the SD and FD part, the reconstructed quantities on station and shower level are stored via a parameter storage class. This class can not only store the values but also the covariances between an arbitrary number of quantities via a simple interface. Defining a new quantity is as simple as it could possibly be.

The only thing to do is to add the name of the quantity to an "enum". The class then provides "getter" and "setter" functions for the value of the quantity and the covariances. One simply has to write (in *C++*)

```
theStation.SetParameter(eNameOfParameter,value);
```

to set a parameter and

```
double par1 = theStation.GetParameter(eNameOfParameter);
```

to retrieve a parameter, where `theStation` is the reference to a radio station. The only restriction is that all parameters in one parameter storage class must have the same data type (doubles in our case).

ADST

At the end of the reconstruction, all quantities important for a final analysis are saved in a *ROOT* [77] based file format called Advanced Data Summary Tree (ADST) developed by the Pierre Auger collaboration [78]. Here as well, one benefits from the parameter storage class. Thus, all quantities stored in the parameter storage class are transfered automatically to the ADST file. This automating saves a lot of work compared to the way it is done for the other detector components, where for each quantity the data structure has to be created manually.

With the ADST package comes a powerful event browser to visualise the detector data. One mayor advantage is that the data from all detector components can be observed in one single browser. Thus, the individual reconstructions can be compared easily to one another. Figure 4.3 shows the radio part of the event browser for a cosmic ray measured with the AERA detector.

4.1.2 Modules

The reconstruction process can be factorised into self-contained data processing steps which are implemented in so-called modules. All modules inherit a common interface which makes it easy to contribute new modules without knowing all details about the whole software. A sequence of modules then forms an application.

The module sequence is defined in a simple XML based language. This language allows to define arbitrarily deep nested loops: Each module can return instructions to the "run controller" such as `break` or `continue` to end a loop or to skip to the beginning of the loop. Thus, quite complex program sequences can be defined.
Listing 4.1 shows an exemplary module sequence for the reconstruction of a self-triggered radio event. The simple XML syntax enables especially new users to directly create their own applications.

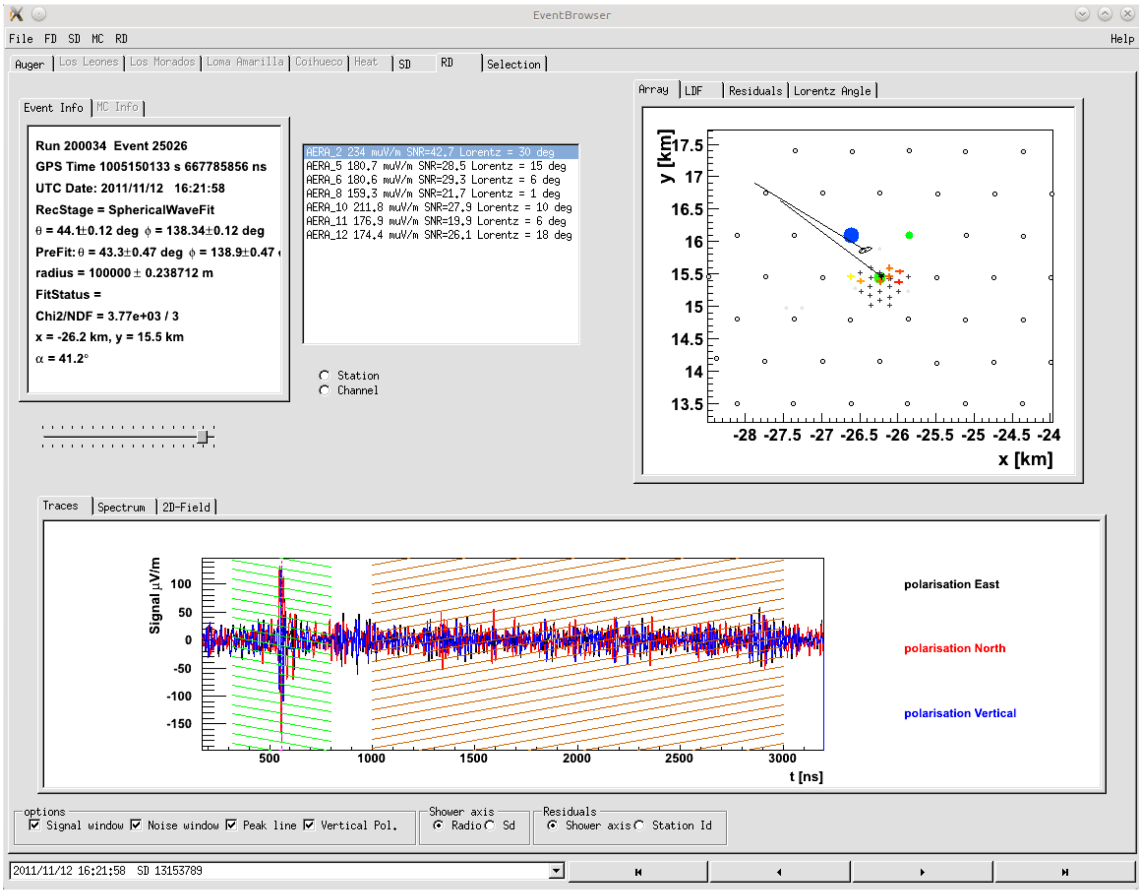

Figure 4.3: Radio part of the Offline event browser.

```
<sequenceFile>
  <moduleControl>
    <loop numTimes="unbounded">
      <module> EventFileReaderOG                     </module>
      ...
      <module> RdChannelADCToVoltageConverter        </module>
      ...
      <module> RdChannelUpsampler                    </module>
      <module> RdChannelBandstopFilter               </module>
      <module> RdPreWaveFitter                       </module>

      <loop numTimes="unbounded">
        <module> RdDirectionConvergenceChecker       </module>
        <module> RdAntennaChannelToStationConverter </module>
        <module> RdStationSignalReconstructor        </module>
        <module> RdWaveFit                          </module>
      </loop>

      <module> RecDataWriterNG                         </module>
    </loop>
  </moduleControl>
</sequenceFile>
```

Listing 4.1: Sample module sequence for the reconstruction of a self-triggered radio event. A detailed description of the modules can be found in [76].

The parameters and configuration instructions for the modules are also defined in XML files. This overall configuration through XML files enables the modification of applications without recompilation. Thus, the speed of a compiled C++ program is combined with the flexibility of a scripting language.

The modular structure has several advantages: For instance, it is easy to exchange and test code with other collaborators and a wide variety of applications can be build up by combining modules in various sequences.

Some of the important modules for the analysis of this thesis are described in the next section. For a complete description of all available modules please refer to [76] or the constantly updated documentation that comes with a current $\overline{\text{Off}}\underline{\text{line}}$ release.

4.2 Signal Processing

In this section the signal processing steps usually applied to radio data are described. It is beyond the scope of this thesis to describe all the steps in detail, therefore, the focus is laid on processing steps important for further analysis but references are given for the interested reader.

The start point of the offline signal processing is the recorded ADC counts (cf. section 3.5). Thus, the first important task is to translate the ADC counts from the digitiser into voltage and unfold the electronic characteristics (refer to [5] for details). Note that the LNA is not considered in this step because it is treated as part of the antenna and, thus, considered in the electric field reconstruction.

Upsampling

The sampling frequency of the AERA digitiser is 200 MHz[1] and the maximum frequency recorded at the AERA radio stations is below the Nyquist frequency of 100 MHz. Thus, according to the Nquist-Shannon sampling theorem [79], the recorded series of sample points contain all information about the signal progression. This means that an arbitrary number of additional sample points that exactly describe the signal progression can be calculated. This method is called upsampling [80]. Upsampling by a factor of $N = 5$ means that the sample distance of $\Delta t = 5$ ns is reduced to $\Delta t = 1$ ns.

By upsampling, the statistical error on the signal time - which is the position of the maximum signal amplitude - can always be reduced to a negligible value. For example AERA has a sampling distance of 5 ns. The envisaged time resolution is 1 ns. With upsampling by a factor of five the statistical uncertainty is reduced to $\Delta t/\sqrt{12} \approx 0.29$ ns.
This processing step is implemented in the $\overline{\text{Off}}\underline{\text{line}}$ module `RdChannelUpsampler`.

[1]A newer electronic version developed at Karlsruhe Institute of Technology and Bergische Universität Wuppertal has a sampling frequency of 180MHz. Because the maximum recorded frequency is below 80MHz the sampling theorem is fulfilled as well. However, all data used in this thesis was recorded with a 200MHz digitizer.

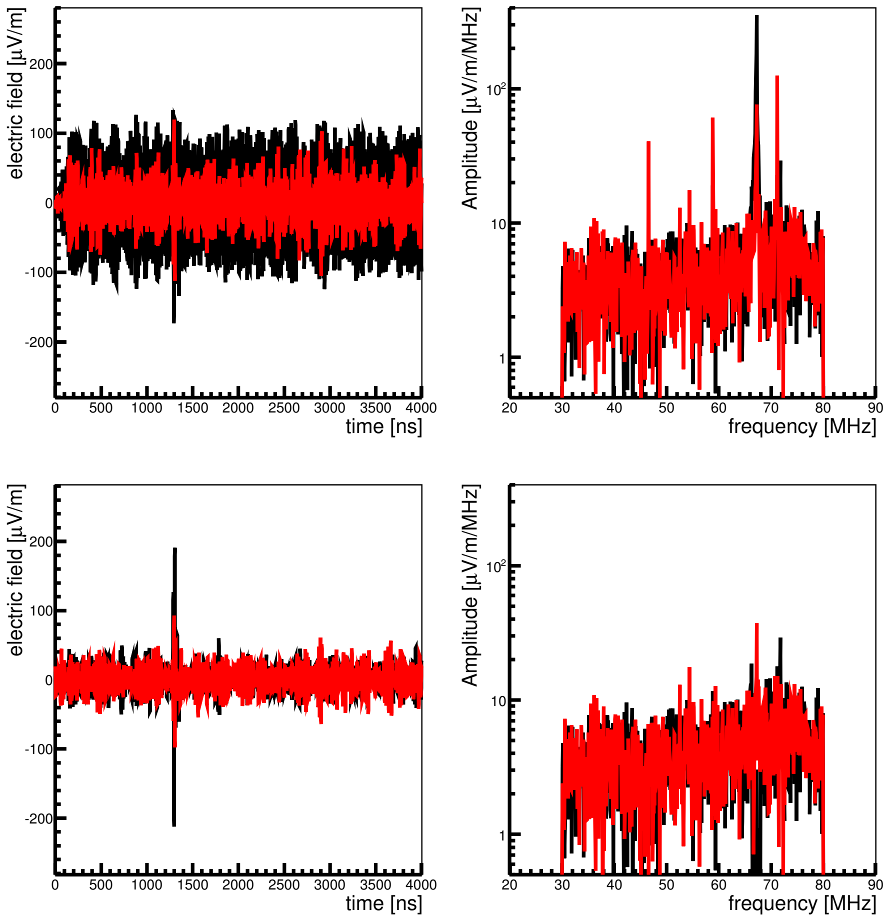

Figure 4.4: The left plots show the east-west (black) and north-south (red) component of the electric field of a cosmic ray radio signal. The right plots show the corresponding frequency spectrum. The upper plots show the situation before filtering narrowband transmitters. After applying a bandstop filter the signal quality is strongly enhanced (lower plots).

Removal of Narrowband Transmitters

A important contribution to the noise background are narrowband transmitters in the frequency range of the AERA antennas. To enhance the signal quality, the frequency bands of known transmitters are removed by means of a band stop filter. Due to the limited resolution of the frequency spectrum and the specific bandwidth of the transmitter, the signal leaks into nearby frequency bins. The leakage can be reduced by applying a window (a Hann window in our case[2]) to the time series prior to the Fourier transformation. Furthermore, the frequency resolution can be enhanced by upsamping.
Figure 4.4 shows meaningfully the improvement of signal quality due to the removal of narrowband transmitters.
This processing step is implemented in the Offline module `RdChannelBandstopFilter`.

[2]A Hann window modulates the beginning and the end of the time trace with a cosine to zero.

Reconstruction of the Electric Field

The three dimensional electric field that has induced the voltage in the antenna is the mayor quantity of interest. Unlike the voltage traces measured by the antennas, the reconstructed electric field is independent of the experimental setup. A comprehensive description and deviation of the formulas that will be used in this paragraph can be found in [5].

The antenna characteristics can be described via the vector effective length (VEL). The measured voltage depends only on the VEL $\vec{H}$ and the adjacent electric field $\vec{E}$:

$$U = \vec{H} \cdot \vec{E} \tag{4.1}$$

This system of equations has three free parameters, the three components of the electric field, but the voltage induced by the electric field $\vec{E}$ is measured at only two different antennas. One antenna is north-south and the other east-west polarized. To be, nevertheless, able to reconstruct all three components of $\vec{E}$, we use the fact that the radial component of the electric field is always zero as the electromagnetic wave propagates towards the antenna. Thus, equation 4.1 has to be solved in a spherical coordinate system where $\vec{e}_r$ points into the incoming direction of the electric field. This direction is the incoming direction of the air shower which accordingly has to be known. See section 4.3 for a description of the reconstruction of the arrival direction with radio technique.

After the coordinate transformation, equation 4.1 forms a linear system of equations with only two unknowns that can be solved most easily in Fourier space:

$$\begin{aligned}
\mathcal{V}_1(\omega) &= \vec{\mathcal{H}}_1(\omega, \theta, \phi) \cdot \vec{\mathcal{E}}(\omega) && (4.2)\\
&= \mathcal{H}_{1,\theta}(\omega, \theta, \phi)\mathcal{E}_\theta(\omega) + \mathcal{H}_{1,\phi}(\omega, \theta, \phi)\mathcal{E}_\phi(\omega) && (4.3)\\
\mathcal{V}_2(\omega) &= \vec{\mathcal{H}}_2(\omega, \theta, \phi) \cdot \vec{\mathcal{E}}(\omega) && (4.4)\\
&= \mathcal{H}_{2,\theta}(\omega, \theta, \phi)\mathcal{E}_\theta(\omega) + \mathcal{H}_{2,\phi}(\omega, \theta, \phi)\mathcal{E}_\phi(\omega), && (4.5)
\end{aligned}$$

where $\mathcal{V}_{1,2}$ is the Fourier transformation of the voltage trace measured in the two antennas and $\vec{\mathcal{H}}_{1,2}$ the corresponding VEL. $\mathcal{E}_\theta$ and $\mathcal{E}_\phi$ are the θ and ϕ components of the electric field in Fourier space.

Solving this equation leads to

$$\begin{aligned}
\mathcal{E}_\theta(\omega) &= \frac{\mathcal{V}_1(\omega)\mathcal{H}_{2,\phi}(\omega) - \mathcal{V}_2(\omega)\mathcal{H}_{1,\phi}(\omega)}{\mathcal{H}_{1,\theta}(\omega)\mathcal{H}_{2,\phi}(\omega) - \mathcal{H}_{1,\phi}(\omega)\mathcal{H}_{2,\theta}(\omega)} && (4.6)\\
\mathcal{E}_\phi(\omega) &= \frac{\mathcal{V}_2(\omega) - \mathcal{H}_{2,\theta}(\omega)\mathcal{E}_\theta(\omega)}{\mathcal{H}_{2,\phi}(\omega)} \quad , && (4.7)
\end{aligned}$$

where the VEL has to be evaluated for the incoming direction (θ, ϕ) of the signal. This processing step is implemented in the $\overline{\text{Off}}\underline{\text{line}}$ module `RdAntennaChannelToStationConverter`.

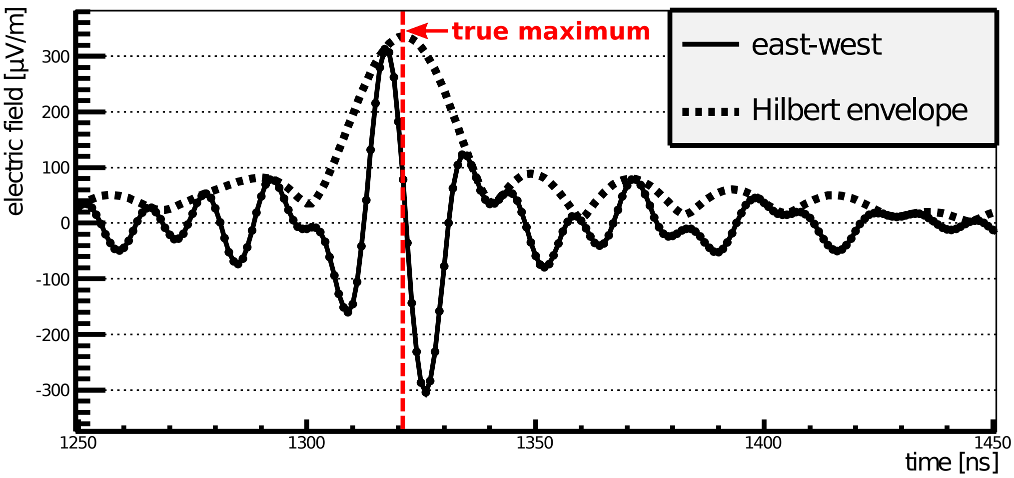

Figure 4.5: East-west component of the reconstructed electric field trace of one of the radio events measured in coincidence with the surface detector. An upsampling by a factor of five was applied.

Hilbert Envelope

As a final step of signal processing, the Hilbert envelope is calculated. As can be seen in figure 4.5, the radio signal can be decomposed into an oscillating part and a part enclosing the oscillation. Studies at the LOPES experiment [81] show that the Hilbert envelope - which is the instantaneous amplitude [82] - is an adequate choice for cosmic ray radio signals. A detailed description on how the Hilbert envelope is calculated on a discrete time series is given in [40].

The Hilbert envelope is very useful for the determination of the maximum signal amplitude. Due to the limited number of discrete sampling points, the maximum value of the measured time series does not necessarily resemble the true maximum. An analysis in [5] shows that for a sampling distance of 5 ns - which corresponds to the sampling frequency of AERA - the value of the maximum is on average only 93% of the height of the true maximum. In contrast, the maximum of the Hilbert envelope estimates the true maximum much better. Here, the maximum is on average more than 99.5% of the true maximum.

This bias could be overcome by reducing the time distance between two sample point via upsampling. However, even with arbitrarily high upsampling the maximum of the signal trace does not always resembles the true signal height because of possible zero crossings of the electric component of the electro-magnetic wave at the position of the true maximum as visible in figure 4.5.

4.3 Directional Reconstruction

This section describes the reconstruction of the incoming direction of the air shower by using the measured signal arrival times at the radio stations. A more detailed description and test of this method can be found in [83] and [5].

Figure 4.6 sketches the basic idea of the fit procedure. The signal passes the antennas from left to right. $\tau_{1,\ldots,5}$ denote the measured signal times at the antennas and τ_0 is the mean signal time. For each station the difference $\Delta\tau_i$ between the measured signal time τ_i and the mean τ_0 is calculated (the grey arrows in panel (b)). With an assumption on the shape of the signal front and the speed of propagation, we can calculate an expectation for the signal time for each hypothetical incoming direction. This is illustrated as red arrows in panel (c). The time differences of the measured signals $\Delta\tau_i$ are compared with the expected time differences Δt_i for a hypothetical incoming direction. A corresponding χ^2-function is defined and minimized to find the direction that describes best the measured data.

A reasonable assumption of the propagation speed of the signal front is the speed of light c. The simplest assumption for the shape of the wave front is a planar wave. Experimental results [84] show that the radio wave front is more complex and can be better described by a spherical or conical wave front.
Note that a fit of a more complex wavefront needs more data points, i.e. more radio stations must have measured the air shower and provide information about the signal time. One needs the timing information of at least three radio stations to fit a plane wave front and the timing information of at least four stations to fit a spherical wave front to the data.
In the following, the implementation of three wavefront models are described more closely. These are a plane wave front, a spherical wave front and a spherical wave front with variable speed of light.

The goodness of the fit depends strongly on the time resolution of the radio stations as the fit uses only the measured signal times. For horizontal showers ($\theta \approx 90°$) an uncertainty in the measured signal times can result in unphysical time differences why the definition of a wave front model with variable speed of light was necessary: When the radio signal is coming from directions close to the horizon, the time difference between two antennas can reach its maximum value which is the geometrical distance in direction of the incoming signal divided by the speed of light:

$$\Delta\tau_{ij,max} = \Delta d_{ij}/c \tag{4.8}$$

If the measured time differences exceed this maximum value the signal seems to propagate too slowly. Thus, the best fit in this case is a wave propagating in the plane of the detector.
The time residua will have a systematic offset: Stations towards the signal direction will measure the signal too early and stations contrary to the signal direction will measure the signal too late. This effect is accounted by allowing small variations of the speed of light.

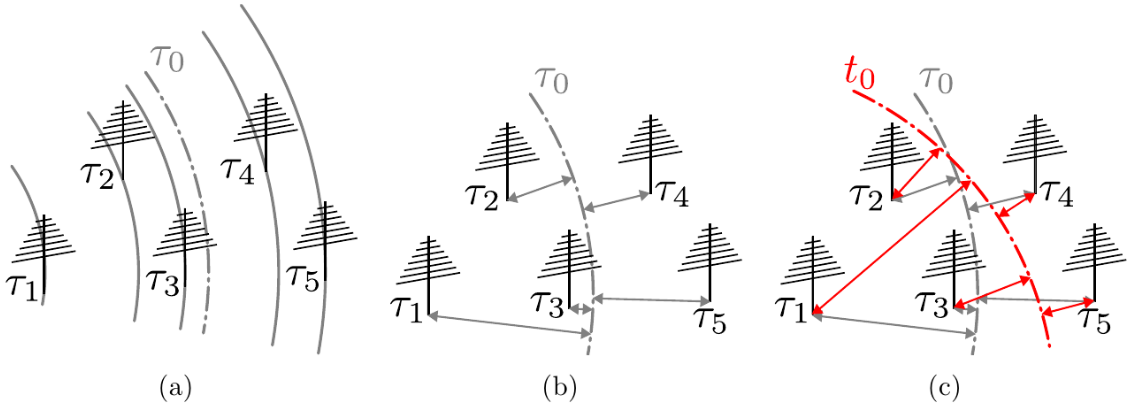

Figure 4.6: Illustration of the directional fit algorithm. From Ref. [83].

The expected signal times can be calculated as follows:

$$t_i^{planar}(\theta,\phi) = -(\vec{n}(\theta,\phi)\cdot\vec{d}_i)/c \tag{4.9}$$

$$t_i^{spherical}(R,\theta,\phi) = |\vec{R}(R,\theta,\phi)-\vec{d}_i|/c, \tag{4.10}$$

where $\vec{n}$ is the incoming direction of the radio signal and $\vec{R}(R,\theta,\phi)$ is the source point of the spherical wave. The variation of the speed of light is introduced by replacing c with $c' = \gamma\cdot c$ resulting in an additional fit parameter γ.

The χ^2 function is defined as

$$\chi^2 = \sum_{i=1}^{N}\left[\frac{((\tau_i-\tau_0)-(t_i-t_0))^2}{\sigma_i^2}\right] \quad , \tag{4.11}$$

where t_0 is the mean of the expected times t_i and σ is the uncertainty of the time resolution of the detector.
If the spherical wave front model with variable speed of light is used, a "penalty term" of the form $(1-\gamma)^2/\sigma_\gamma^2$ is added to the χ^2. This term leads to a higher χ^2 the more the speed of light is changed and, thus, allows only small variations of c. The value of σ_γ depends on the actual time resolution of the detector.

The minimization Algorithm

Finding the minimum of the χ^2 function, i.e. the arrival direction of the air shower, is not trivial, especially if a spherical wave front with its three (or four) free parameters is considered.

The success of the minimization depends strongly on a good choice of initial parameters. Therfore, the first minimization step is always a fit of a plane wave front with different initial values for the zenith and azimuth angle (θ, ϕ). The parameters with the overall best χ^2 is the best result.
The fit procedure for a spherical wave front uses the result of the plane wave fit as initial parameters for θ and ϕ. Again, different initial values for the distance to the source point R are tested and the result with the minimal χ^2 is best.
Similarly, the result of the spherical wave fit is used as initial value of the source point if the propagation speed is used as additional fit parameter.

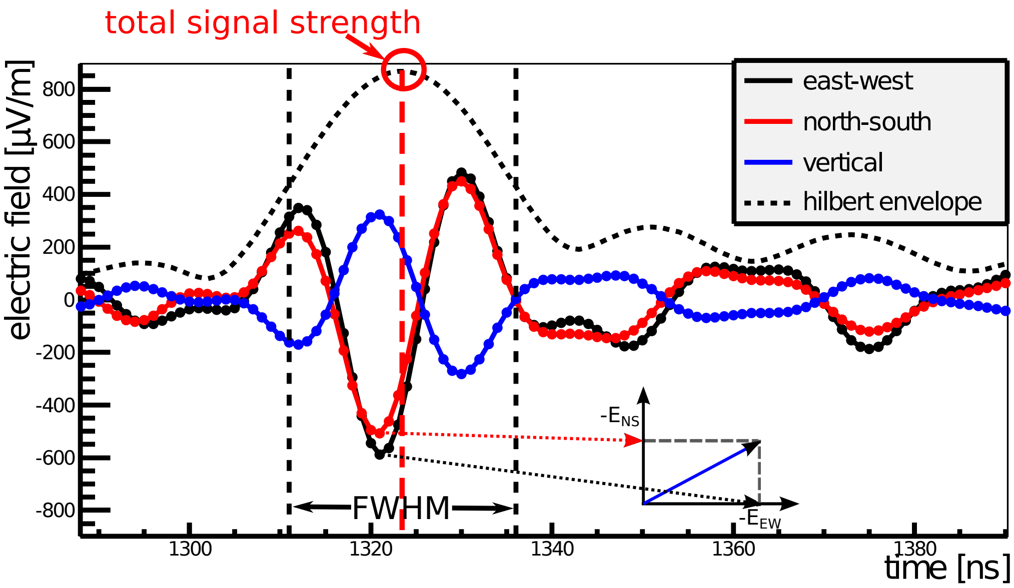

Figure 4.7: Reconstructed electric field trace of one of the radio events measured in coincidence with the surface detector. An upsampling by a factor of five was applied. The Hilbert envelope (dashed line) is the square root of the quadratic sum of the Hilbert envelopes of the three polarisations. The small sketch illustrates exemplarily for the EW-NS plane the direction of the electric field vector at a single time sample.

Peculiarity of the Directional Reconstruction

If the signal quality of the radio pulse is low, it happens that the correct pulse position can not be determined. Normally, this leads to larger timing differences between the radio stations than the allowed ones for the geometry of the AERA array. The largest timing difference can be achieved for horizontal directions because that maximizes the distance that a signal needs to propagate from one antenna to the other and, accordingly, a horizontal direction minimizes the above defined χ^2 for unphysical timing differences. Hence, a wrongly identified pulse position will mostly result in a reconstructed zenith angle of 90°.

Implementation in Offline

This fit procedure is implemented in the $\overline{\text{Off}}\underline{\text{line}}$ module `RdWaveFit` in a very flexible way. The core of this module is the definition of the χ^2 functions for the different wave front models. Within the function the expected times are calculated and compared with the measured ones by calculating the χ^2. Hence, adding a new wave front model is simple. One mainly needs to define a new χ^2 function according to the new wave front model.

4.4 Electric Field Vector

Figure 4.7 shows an example of a reconstructed electric field trace. To determine the total signal strength, the Hilbert envelope - which is the instantaneous amplitude

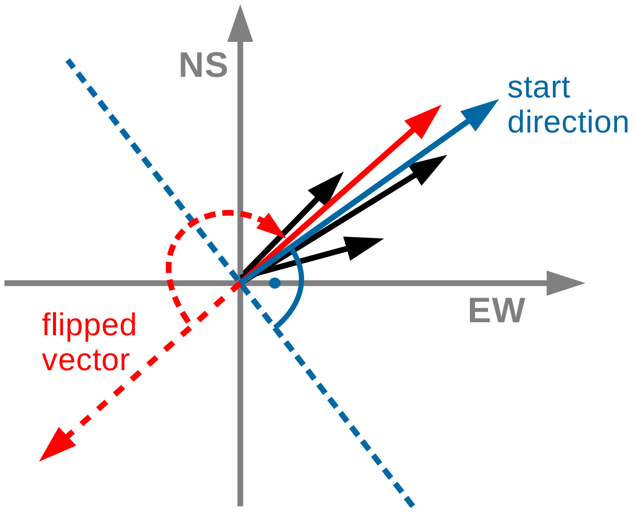

Figure 4.8: Illustration of the averaging process. Each arrow is an electric field vector corresponding to a specific time sample projected on the east-west north-south plane. Each arrow that has an angular distance greater than 90° to the start direction (blue vector) is flipped by 180° (red arrow).

- is calculated. The Hilbert envelope shown in this plot is the square root of the quadratic sum of the Hilbert envelopes of the three polarisations. The total signal strength is defined as the maximum of this Hilbert envelope.
We are not only interested in the total signal strength but also in the direction of the electric field. For each sampling point, the three components of the electric field form a three dimensional vector in a Cartesian coordinate system (cf. fig. 4.7). We observe that all vectors around the maximum of the radio pulse are aligned approximately in the same way. To determine the mean electric field vector around the pulse position most accurately, we average over all vectors in the FWHM interval of the Hilbert envelope.

When averaging, an issue occurs at zero crossings of the electric field. There the direction of the electric field vector changes by 180°, i.e. the vector points into the opposite direction. This is solved in the following way (see fig. 4.8 for an illustration): First, a start direction of the electric field vector is defined as the direction at the first maximum of the trace to the left of the maximum of the Hilbert envelope. Then, each vector that has an angular distance greater than 90° from the start vector is flipped by 180° (multiplied with -1). These partially corrected vectors are added up to determine the mean electric field vector:

$$\vec{E} = \sum \vec{E}_{i,corrected} \tag{4.12}$$

By averaging in such a way, vectors with high amplitudes have a higher weight. This is advantageous because the higher the amplitude the lower the influence of noise. From now on we will refer to this averaged vector as the “electric field vector”. After averaging, the length of the electric field vector is set to the maximum of the Hilbert envelope.
This calculation is performed by the $\overline{\text{Off}}\underline{\text{line}}$ module `RdEFieldVectorCalculator`.

5. Data Set and Cuts

In this thesis, self triggered radio data recorded between April and September 2011 is used. During this period of data taking, all 21 radio stations were operating and equipped with the *Dutch* version of the station electronics. The data volume accumulates to $\sim$3.3 TByte and contains more than 25 million reconstructable events from which most events originate from noise sources and not from cosmic ray induced air showers. This data set is referred to as AERA21.
This huge amount of data requires special computing power. Thus, the high performance cluster (HPC) of the RWTH university - which is one of the hundred world's fastest super computers [85] - is used to reconstruct and process the data.

Figure 5.1 shows the reconstructed arrival directions of all 25 million self-triggered events. Most events accumulate at the 90° zenith bin. Besides the fact that most events originate from noise sources at the horizon, this is an additional artefact of the reconstruction. First, the directional reconstruction is limited to a zenith angle of 90°. Second, a wrongly identified pulse position leads normally to a reconstructed zenith angle of 90° (cf. chapter 4.3).
Beside this feature, one observes that most events come from a few hotspots from the horizon. Detailed surveys of the noise sources at the AERA site have identified most of these hotspots [83] [70]. Thus, e.g. power line poles, a transformer or a nearby village were identified as the origin of these radio pulses.
Furthermore, the positions of the hotspots are washed out (note the logarithmic scale of the skymap). Hence, a signal originating from a hotspot at the horizon can be reconstructed towards lower zenith angles. In addition, bow-like structures over the whole sky are observed which is due to particular geometrical configurations of the triggered radio stations (cf. chapter 8.5.1).

5.1 Cosmic Ray Radio Events

Radio events originating from cosmic ray induced air showers can be identified by comparing the event time and arrival direction with the cosmic rays measured by the surface detector (SD). These coincident events are especially useful because the SD information can be used to calibrate the AERA detector. However, not all cosmic ray radio events can be found with this method, because the energy threshold of SD is higher than the one of AERA. Therefore, the self-triggered data set should contain more cosmic ray events than the events measured in coincidence with SD.

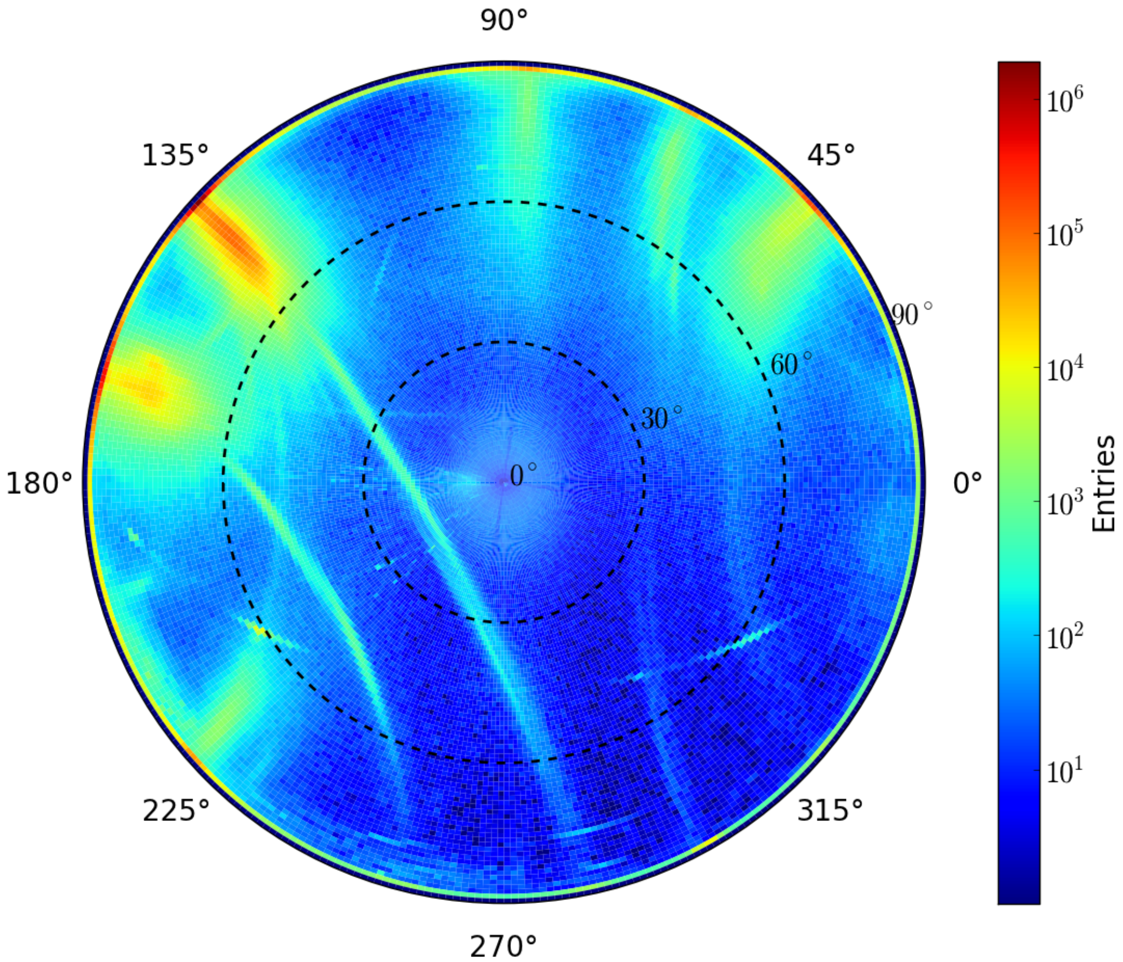

Figure 5.1: Skymap of arrival directions of all self-triggered events. The event rate per bin is colour coded.

In this thesis, coincident events from the AERA21 and AERA12 data set are used. The latter data set was recorded from 11/11/2011 to 2/29/2012 with only 12 radio stations equipped with the *Dutch* version of the station electronics[1].

To use these events in further analyses some quality cuts have to be applied:
We require a zenith angle smaller than 55° to have a reliable SD reconstruction. The reconstruction of the electric field needs the arrival direction of the air shower as input parameter (cf. chapter 4.2) for what the more precise information of SD is used. The surface detector reconstruction is performed with the observer pipeline[2] from the actual Offline trunk. The result of this reconstruction is compared with the official observer reconstruction with version no. v7r4[3]. We observe a difference in the reconstructed core position and cosmic ray energy for a small number of events. Therefore, we always use the result of the official observer reconstruction, except for

[1]The other radio stations were equipped with a enhanced station electronic version but data recorded with this electronic version was not yet available for this thesis.

[2]"Observer" is the name of the standard reconstruction of the surface detector.

[3]http://augerobserver.fzk.de/doku.php

the shower axis that is needed during the reconstruction, as input for the electric field reconstruction. Three events in our data set are not available in the official observer reconstruction and, thus, will be rejected.
One event has such a small SNR that at one station the wrong pulse is identified and, therefore, it is rejected[4].
Due to an initial list of “coincident events” of the AERA group, we excluded two events that actually pass the previously defined quality cuts[5]. In further analyses this events should be considered.

Rejection of Thunderstorm Events

Events recorded during periods with abnormal conditions of the electric field in the atmosphere (like thunderstorms) are rejected too. To determine these events, the data from the electric field mill mounted at the central radio station (CRS) is analysed. We use two different algorithms:

The first looks for abnormal electric fields in the atmosphere. All periods with an electric field higher than 50 V/m or smaller than -150 V/m or with a RMS greater than 30 V/m are rejected. With this algorithm, we find eight events in the data set.

The second algorithm is more sophisticated and sensitive to thunderstorms. This algorithm was used by LOPES and is described in detail in [86]. It finds two events in our data set which where also found by the first algorithm. An interesting fact is that these two events have a very clear signal but the polarisation is completely different, compared to the expectation for geomagnetic emission, and the estimated energy is way to large. This indicated that radio signals can be amplified strongly by thunderstorms. See analysis in chapter A.1 for details. This behaviour was also observed by LOPES [87].

For some events, no weather data was available. To not exclude these events from our analysis we investigated the weather data from the balloon launching station (BLS). Fortunately, at times where no weather data is available at the CRS the electric field mill at the BLS measures - during two hours around the event time - normal conditions of the atmospheric electric field. Thus, we conclude that at the CRS are also normal atmospheric conditions and these events can be used in later analyses.

The different cuts are summarized in the following table:

reason	number of rejected events
zenith > 55 deg	26
no official observer reco.	3
thunderstorm cut	3
wrong radio pulse identified	1
no “initial coincident event”	2

Figure 5.2 shows an overview of the remaining 33 events.

[4] Event no. 104309
[5] Event no. 19865 and 25026

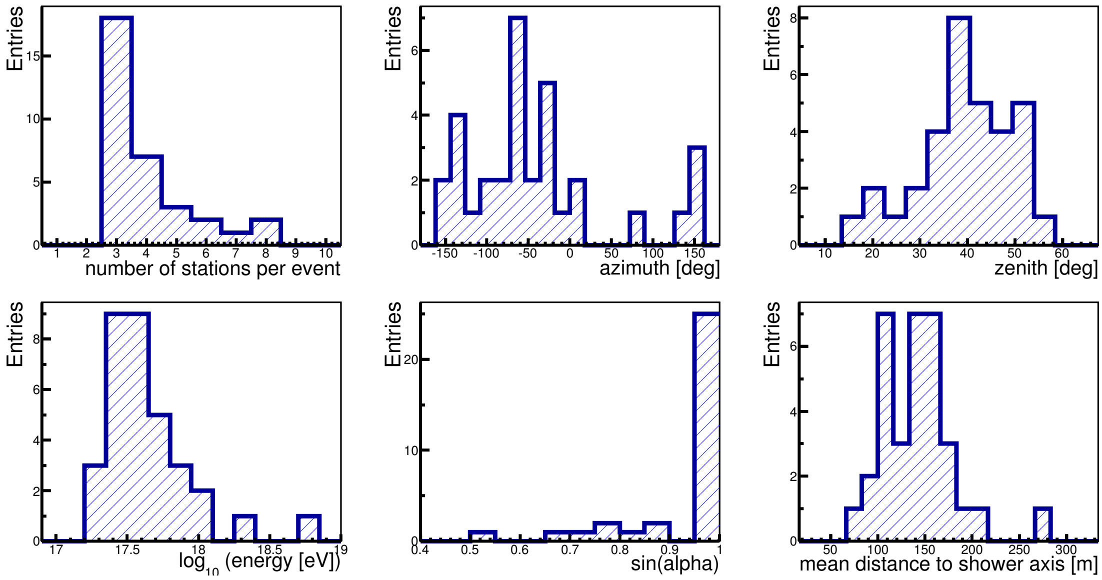

Figure 5.2: Overview of the coincident data set after all cuts.

6. Properties of Cosmic Ray Radio Pulses

In this chapter the properties of cosmic ray radio pulses are analysed. The first section deals with a correct description of the signal quality. Then, a method to simulate realistic electric field traces containing cosmic ray radio pulses is presented. In the third section, this simulation is used to determine the uncertainty of cosmic ray signals for a given signal quality. And finally, the polarisation of the measured cosmic ray radio pulses - which contain information about the emission process - is analysed.

6.1 Definition of a Signal to Noise Ratio

The quality of a radio signal can be described well with the signal to noise ratio (SNR). Unfortunately, different definitions of a SNR exist and are frequently used. This situation leads not only to misunderstandings but, furthermore, it is also unclear what e.g. a SNR of 20 means.

In this section all common SNR definitions are analysed and, fortunately, all of them show a strong correlation. Furthermore, the proportionality constants will be determined so that the user can convert them to his favoured definition.

The possible definitions for a SNR that are considered are the followings[1]:

- $SNR_1 = \frac{H_{max}^2}{H_{mean}^2}$
- $SNR_2 = \frac{H_{max}^2}{H_{RMS}^2}$ [2]
- $SNR_3 = \frac{T_{max}^2}{T_{RMS}^2}$
- $SNR_4 = \frac{H_{max}^2}{T_{RMS}^2}$

where T is the electric field trace and H is the Hilbert envelop of that trace. With "max" the maximum of the absolute value of the trace is meant, thus either the

[1] Note that we use always the quadratic definition. This analysis can be easily translated to a linear definition by just taking the square root of the derived proportionality constants.

[2] This is the default definition of $\overline{\text{Off}}\underline{\text{line}}$.

minimum or the maximum. RMS is the root mean squared and not the standard deviation.

To analyse the different SNR definitions, all events measured in coincidence with the surface detector are analysed. For each polarisation and the total component[3] of the electric field the different SNR definitions are calculated.

Figures 6.1, 6.2 and 6.3 show the relation between the different definitions of a SNR. All SNR definitions show a strong correlation to each other. Thus, it does not make a difference which definition is used.
Figure 6.3 shows, in addition, that the maximum of the Hilbert envelope is on average 6% to 7% higher than the maximum of the trace.

In the following table the result is summarized. To simplicity matters, the result for the EW, NS and vertical component of the electric field are combined.

SNR definition	total component	EW, NS, V component
$2 \to 1$	$\frac{H^2_{max}}{H^2_{RMS}} \approx 0.9 \cdot \frac{H^2_{max}}{H^2_{mean}}$	$\frac{H^2_{max}}{H^2_{RMS}} \approx 0.8 \cdot \frac{H^2_{max}}{H^2_{mean}}$
$3 \to 1$	$\frac{T^2_{max}}{T^2_{RMS}} \approx 1.6 \cdot \frac{H^2_{max}}{H^2_{mean}}$	$\frac{T^2_{max}}{T^2_{RMS}} \approx 1.4 \cdot \frac{H^2_{max}}{H^2_{mean}}$
$4 \to 3$	$\frac{H^2_{max}}{T^2_{RMS}} \approx 1.1 \cdot \frac{T^2_{max}}{T^2_{RMS}}$	$\frac{H^2_{max}}{T^2_{RMS}} \approx 1.1 \cdot \frac{T^2_{max}}{T^2_{RMS}}$
$3 \to 2$	$\frac{T^2_{max}}{T^2_{RMS}} \approx 1.8 \cdot \frac{H^2_{max}}{H^2_{RMS}}$	$\frac{T^2_{max}}{T^2_{RMS}} \approx 1.8 \cdot \frac{H^2_{max}}{H^2_{RMS}}$

The proportionality between SNR_2 and SNR_3 was calculated from the proportionality between SNR_1 and SNR_2 and the proportionality between SNR_1 and SNR_3. Thus, for the total component we obtain

$$\frac{T^2_{max}}{T^2_{RMS}} \approx 1.6 \cdot \frac{H^2_{max}}{H^2_{mean}} \approx 1.6 \cdot 0.9^{-1} \cdot \frac{H^2_{max}}{H^2_{RMS}} \approx 1.8 \cdot \frac{H^2_{max}}{H^2_{RMS}} \tag{6.1}$$

and for the other polarisations

$$\frac{T^2_{max}}{T^2_{RMS}} \approx 1.4 \cdot \frac{H^2_{max}}{H^2_{mean}} \approx 1.4 \cdot 0.8^{-1} \cdot \frac{H^2_{max}}{H^2_{RMS}} \approx 1.8 \cdot \frac{H^2_{max}}{H^2_{RMS}}. \tag{6.2}$$

The error on the proportionality constants is estimated to a few percent by examining the change of the proportionality constants for different data sets.

SNR_2 is the default definition of $\overline{\text{Off}}\underline{\text{line}}$ and will be used in all further analysis.

[3]The total component is defined as $E_{total} = \sqrt{E^2_{EW} + E^2_{NS} + E^2_V}$, the total component of the Hilbert envelope is $H_{total} = \sqrt{H^2_{EW} + H^2_{NS} + H^2_V}$ the vectorial sum of the Hilbert envelopes for each polarisation.

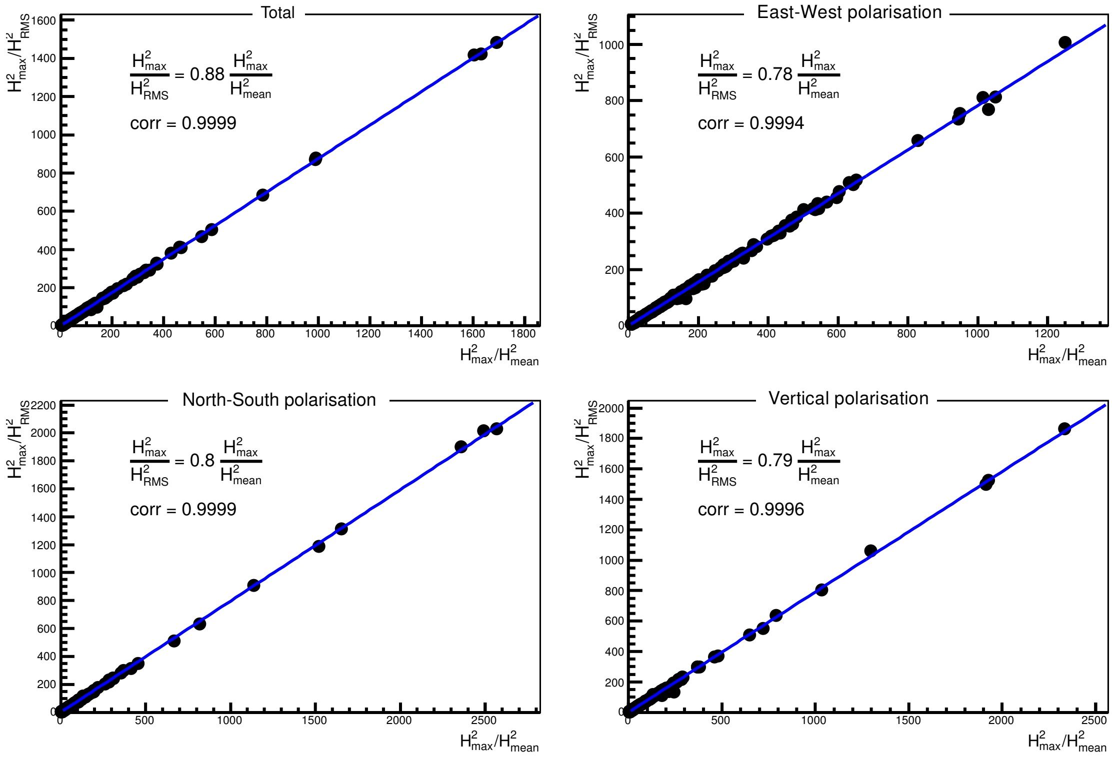

Figure 6.1: Correlation between SNR_1 and SNR_2

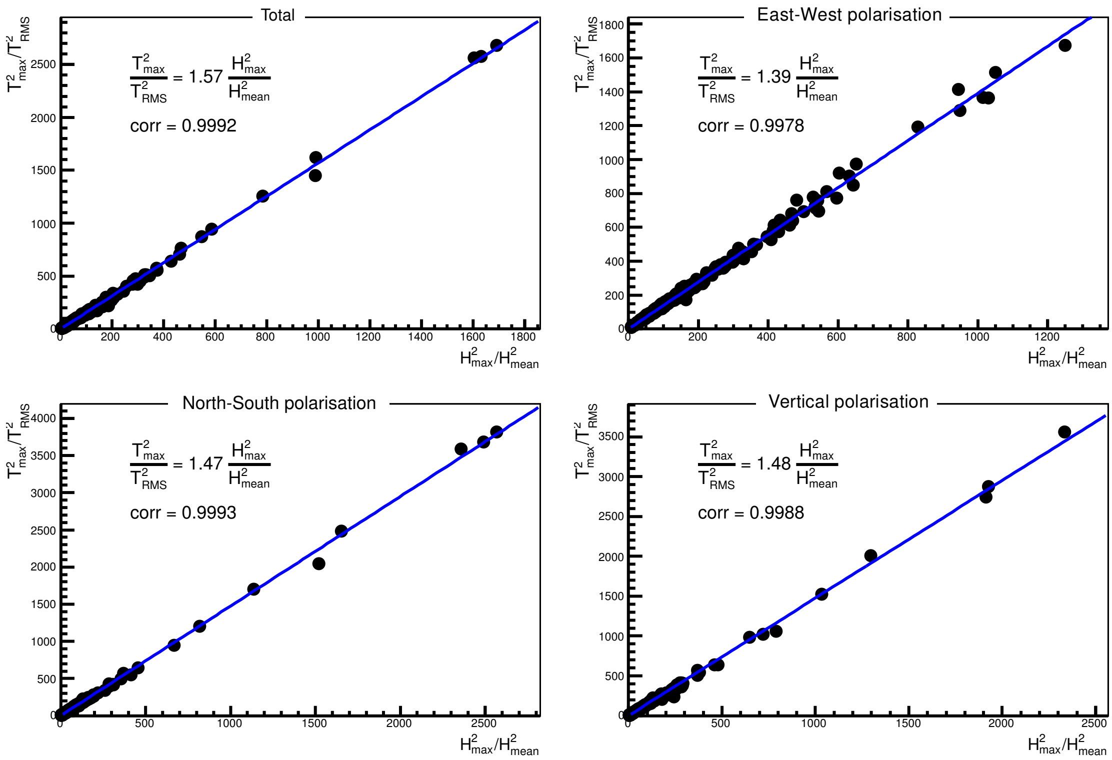

Figure 6.2: Correlation between SNR_1 and SNR_3

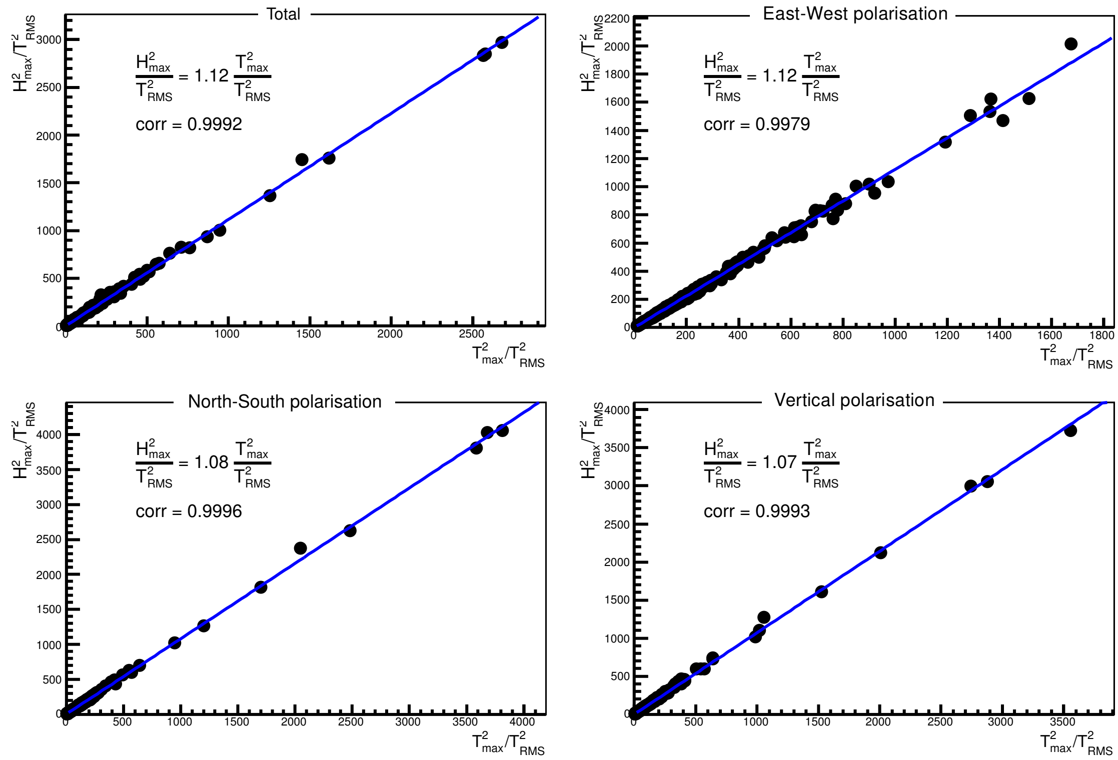

Figure 6.3: Correlation between SNR_3 and SNR_4

Consistency

As pointed out by [88], a consistent definition of a signal to noise ratio should result in a SNR of one if the trace does not contain signal. However, all four SNR definitions do not fulfil this consistency criterion.
Figure 6.4 shows the measured SNR for pure noise traces. The expectation value of the SNR_2 for the total component of a trace without signal is approximately five. The asymmetry towards higher values of the SNR is due to the quadratic definition of the SNR.
A pragmatic and feasible solution to solve this inconsistency, in contrast to a more complicated SNR definition as proposed in [88], is to normalize the SNR by its expectation value for noise. This will directly lead to a consistent definition.

6.2 Simulation of Electric Field Traces

Analysing simulations instead of real measurements has the huge advantage that the true air shower properties are known. Thus, the full reconstruction pipeline can be tested and the impact of disturbing environmental influences (such as noise) can be estimated. For this purpose, a program is created to generate electric field traces corresponding to specific air shower properties. Furthermore, the $\overline{\text{Off}}\underline{\text{line}}$ software framework is extended by a module to read in the simulated $\vec{E}$-field traces. Hence, all modules dedicated to the reconstruction of electric field properties can be tested easily.

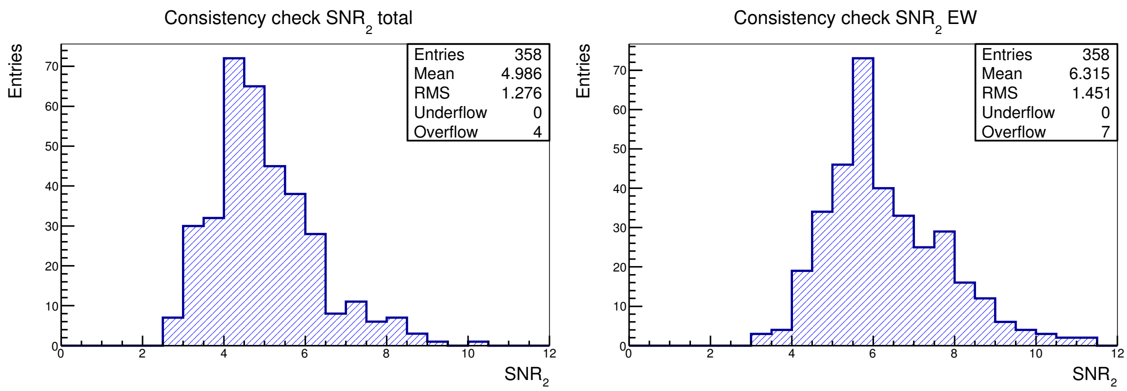

Figure 6.4: Signal to noise ratio of pure noise traces (i.e. a trace that does not contain a signal). The north-south and vertical component show approximately the same result as the east-west component. The asymmetry is due to the quadratic definition of the SNR.

We use a band-width limited delta pulse to describe the signal shape of the cosmic ray radio signal. The frequency spectrum of a delta peak[4] is a uniform distribution of all frequencies. When the frequency spectrum is band pass filtered from 30 MHz to 80 MHz[5] and transformed back to the time domain, the former delta pulse now oscillates as can be seen in figure 6.5 top.

We generate $\vec{E}$-field traces in the following way: First, the bandwidth limited Dirac pulse is generated for all three components of the electric field. The amplitudes of the three projections of the $\vec{E}$-field are adjusted following the geomagnetic emission model. This is

$$\vec{E} \propto \vec{n} \times \vec{B}, \tag{6.3}$$

where $\vec{B}$ is the magnetic field vector at the AERA site and $\vec{n}$ is the shower axis. The total signal height (as defined in chapter 4.4) is set to unity.
Second, noise is added to the perfect signal. The noise trace is obtained from the events that are measured in coincidence with the surface detector[6]. We get 152 noise traces for each component of the $\vec{E}$-field . For each simulated trace, we choose one of the 152 noise traces randomly. The noise trace is cut to the correct length and the start time of this interval is chosen randomly between 0ns and 500ns. The amplitude is set accordingly to the SNR of the measured event. Noise for the three projections of $\vec{E}$ are taken from the corresponding projections of the same noise trace. This is necessary because the different projections are correlated. An example of such a trace can be seen in figure 6.5 bottom.

Finally, the $\vec{E}$-field traces of different radio stations form an event. For the geometric positions of the radio stations, the positions of the 21 AERA radio stations are used. The timing of the signal pulses in the different stations is adjusted according

[4]With "delta peak" we mean that only one bin of the sampled electric field trace is unequal zero.
[5]This is approximately the bandwidth of the AERA detector.
[6]The noise trace is taken from an interval of the trace behind the cosmic ray radio pulse.

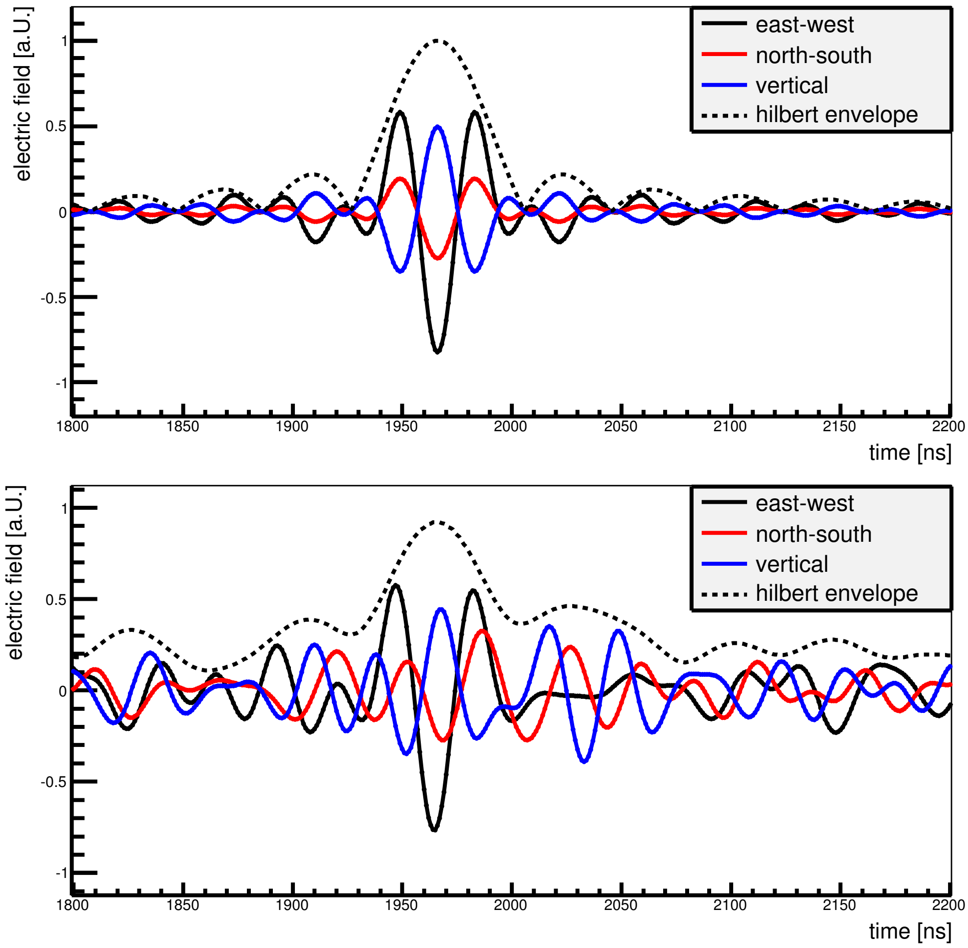

Figure 6.5: Example of a simulated electric field trace. (*top*) Bandwidth limited delta pulse for all three components of the $\vec{E}$-field. (*bottom*) Same as the upper plot but with noise.

to a selectable shape of the signal front. A plane and a spherical signal front is currently implemented. Thus, this simulation can be used to test the directional reconstruction and to determine the influence of noise or timing uncertainties onto the angular resolution. However, it is beyond the scope of this thesis to investigate these influences.

The simulated $\vec{E}$-field traces of all stations that form an event, including the information about the shower properties such as the incoming direction, are saved to ASCII. The text files can then be read in by the new $\overline{\text{Off}}\underline{\text{line}}$ module written for this purpose.

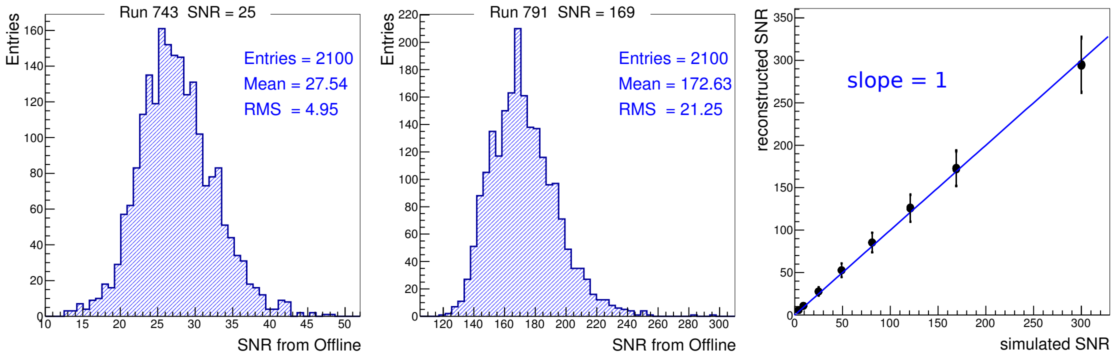

Figure 6.6: Consistency check of the correct simulation of the signal to noise ratio. The y-values in the graph are the mean and the error bars the RMS of the corresponding histogram.

6.3 Uncertainty of the Electric Field Vector

To study the influence of noise on the electric field vector (i.e. the signal height and the Lorentz angle), more than 250,000 $\vec{E}$-field traces are generated and analysed. For each combination of the following properties, 100 events with all 21 AERA stations are simulated (the timing is adjusted using a spherical signal front):

- SNR[7] = 4, 9, 25, 49, 81, 121, 169, 300
- zenith = 10°, 30°, 50°
- azimuth = 270°, 300°, 315°, 330°, 360°
- radius = 10,00 0m
- core position = bary center of participating antenna stations

All simulated events are analysed using $\overline{\text{Off}}\underline{\text{line}}$. The events are read in with the module `RdMySimShowerReader` and the $\vec{E}$-field properties are reconstructed using the modules `RdStationSignalReconstructor` and `RdEFieldVectorCalculator`.

As a first consistency check, the measured SNR is compared to the SNR adjusted in the simulation. Figure 6.6 shows that the measured SNR scatter around the adjusted one. This is because the signal can interfere both constructively and destructively with the noise and, thus, change the true value of the maximum which results in a different SNR. However, these small deviations from the design value do not have a disturbing influence on the following analysis.

Figure 6.7 shows the reconstructed signal height for different signal to noise ratios. Each histogram contains the values of the maximum signal height for one specific SNR and incoming direction of the air shower. For each of these combinations, 100

[7]According to the second (the standard $\overline{\text{Off}}\underline{\text{line}}$) SNR definition.

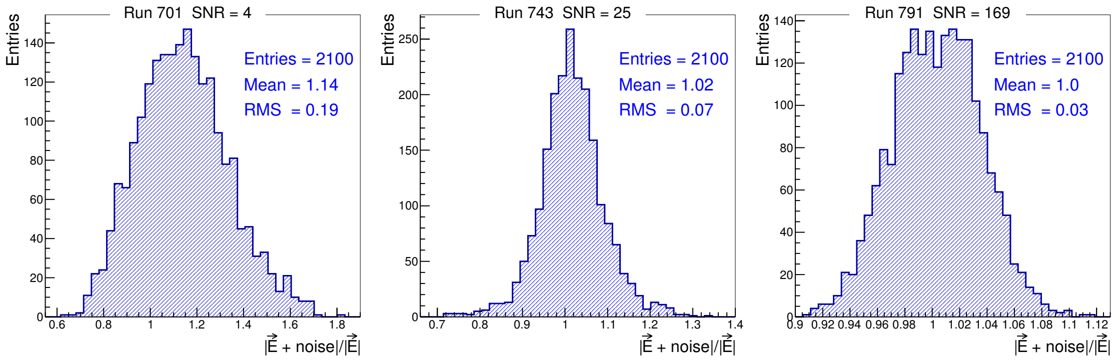

Figure 6.7: Variation of signal height due to noise. The three histograms show the variation of the signal height for simulations with different signal to noise rations. Note that the x-axis range does change.

events with 21 stations were simulated resulting in the 2,100 entries in the histogram. The standard deviation of the signal height distribution is used as measure of the uncertainty.

Figure 6.8 shows the result for all incoming directions and signal to noise ratios. In the left figure, the average signal height (the mean of the histogram) is plotted versus the measured SNR. Only at very small SNRs the noise background has a significant influence on the average signal height. The average change of the signal height can be nicely described with the following function:

$$\frac{<|\vec{E}|>}{|\vec{E}_{true}|} = 1 + \frac{0.95 \pm 0.09}{\sqrt{SNR^{2.30 \pm 0.05}}}. \tag{6.4}$$

The right plot in figure 6.8 shows the dependence of the uncertainty of the signal height on the SNR. The uncertainty on $|\vec{E}|$ is anti-proportional to the square root of the SNR. The best fit to the data is

$$\frac{\sigma_{|\vec{E}|}}{|\vec{E}_{true}|} = \frac{0.403 \pm 0.003}{\sqrt{SNR}}. \tag{6.5}$$

This proportionality corresponds to the reasonable assumption that the uncertainty of the signal height is proportional the the RMS of the noise trace as the following equation illustrates:

$$\frac{\sigma_{|\vec{E}|}}{|\vec{E}_{true}|} \propto \frac{1}{\sqrt{SNR}} \propto \frac{RMS}{|\vec{E}|}. \tag{6.6}$$

A closer inspection of figure 6.8 right suggests that the uncertainty on the signal height does depend on the specific arrival direction. With changing arrival direction, the signal pulse is distributed differently onto the three components of the electric field (cf. eq. 6.3). For instance an air shower coming from the south (azimuth = 270°) will mostly cause a signal in the east-west component of the

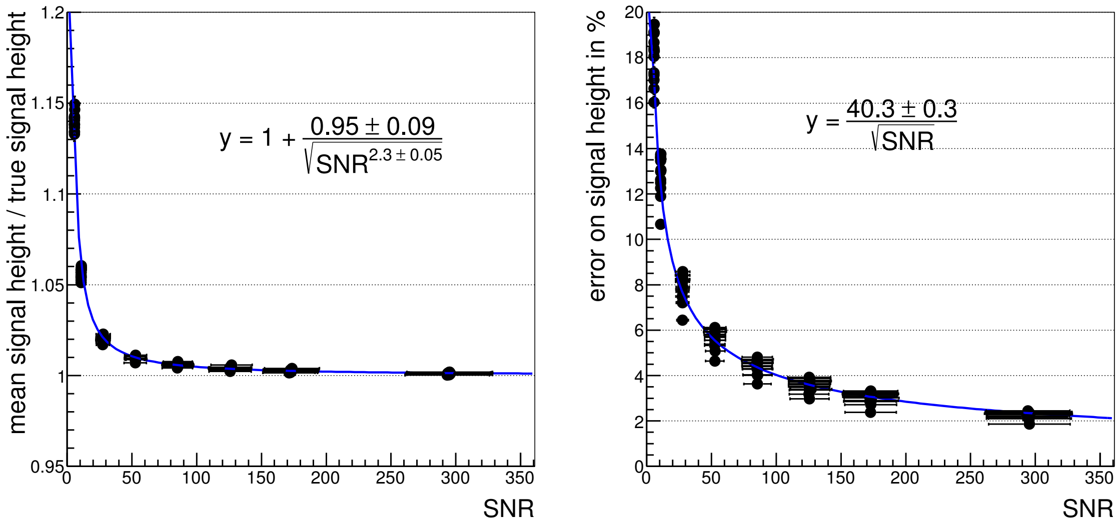

Figure 6.8: (*left*) Variation of the true signal height as a function of signal to noise ratio. Only at low SNR the signal height is on average significantly increased. (*right*) The uncertainty on the signal height as a function of signal to noise ratio. Note that the average overestimation of the signal height is compatible to the true signal height within its uncertainties. The x-error bars are the width of the measured SNR distributions (cf. 6.6). The multiple data points for one SNR are the results for the different simulated arrival directions.

$\vec{E}$-field . To quantify how much the signal is distributed onto the three components of electric field, the standard deviation of $|\vec{E}|$ is calculated:

$$\sigma = \sqrt{\frac{1}{3}\sum_{i=1}^{3}(|E_i| - <|\vec{E}|>)^2}, \quad \text{where} <|\vec{E}|> = \frac{1}{3}\sum_{i=1}^{3}|E_i|. \tag{6.7}$$

Figure 6.9 shows clearly that the uncertainty of the signal height increases with increasing σ. This means that the signal height can be reconstructed more precisely if the signal is distributed more uniformly onto the three components of $\vec{E}$.

Another quantity of interest is the so-called Lorentz angle, i.e. the angle between the Lorentz force acting on the charged particles in the shower and the electric field vector. As in this simulations the radio signal was generated to obey geomagnetic emission, the expectation value for the Lorentz angle is zero. Any deviation from zero is due to noise, though.
Figure 6.10 shows the distribution of the reconstructed Lorentz angles for different SNRs. The distribution gets narrower with higher SNRs and can be described with a Rayleigh function:

$$f(x) = \frac{x}{\sigma^2} \cdot exp\left(-\frac{x^2}{2\sigma^2}\right). \tag{6.8}$$

The position of the maximum of the Rayleigh function, which is the parameter σ of this function, is defined as the uncertainty on the Lorentz angle.

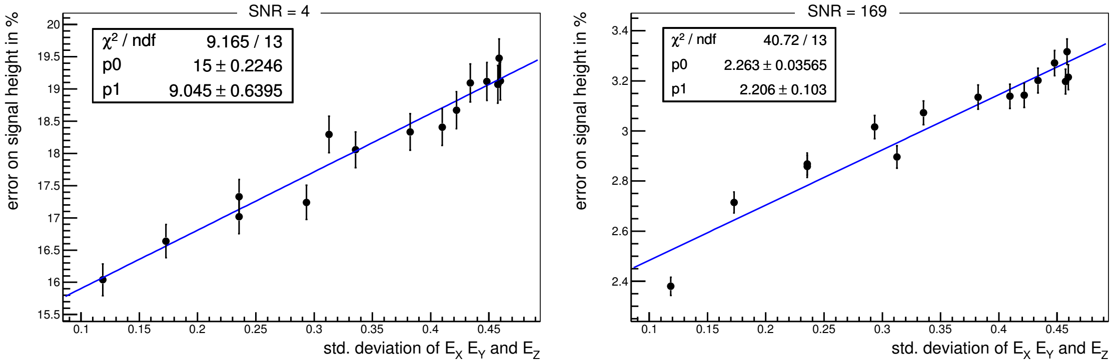

Figure 6.9: Dependence of the uncertainty of the signal height on the arrival direction (see text for details) exemplary for two different SNR. The dependency for other SNRs is qualitatively the same.

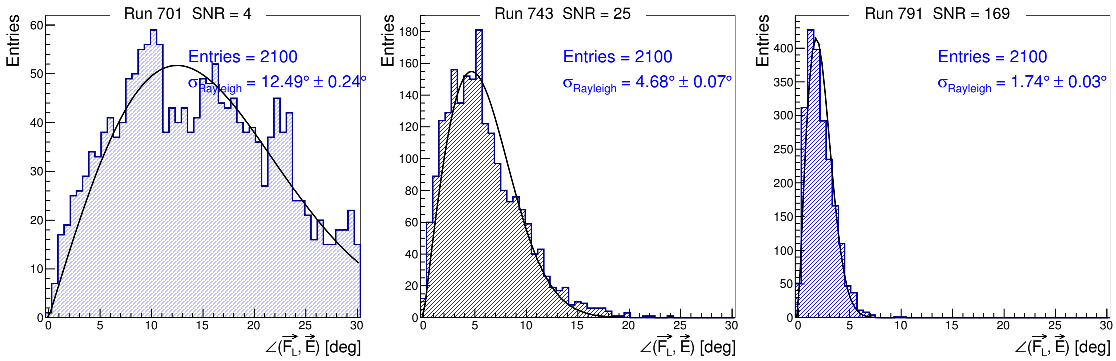

Figure 6.10: Variation of the angle between Lorentz force and electric field vector (Lorentz angle). The polarisation of the electric field vector was simulated accordingly to the geo-magnetic emission process. Thus, the expectation of the Lorentz angle is zero. The three histograms show the variation of the Lorentz angle for simulations with different signal to noise ratios.

Figure 6.11 shows that the uncertainty on the Lorentz angle is anti-proportional to the square-root of the SNR too and can be parameterized with

$$\sigma_{\text{Lorentz angle}} = \frac{24.2 \pm 0.2}{\sqrt{SNR}}. \tag{6.9}$$

6.3.1 Individual Uncertainty Calculation for Coincident Events

As the uncertainty on the signal height depends on how the signal is distributed onto the three components of the electric field, the error estimation can be improved by simulating each event individually. This is done for the all coincident events that survive the quality cuts defined in chapter 5:

For each event and station we generate 200 electric field traces with known signal, add noise and run the $\overline{\text{Off}}\underline{\text{line}}$ reconstruction chain to reconstruct the signal. With

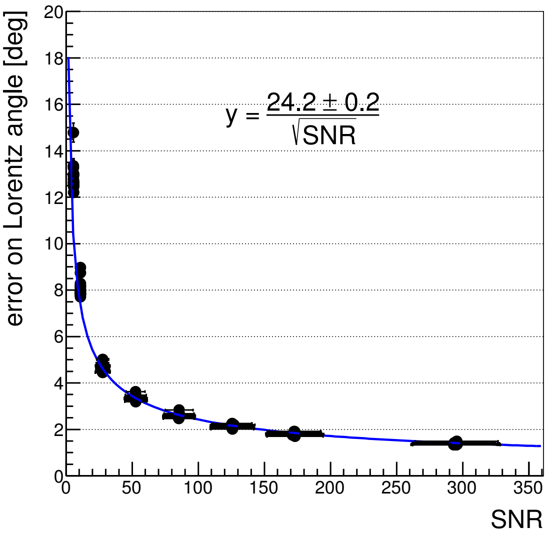

Figure 6.11: Uncertainty of the Lorentz angle as a function of the signal to noise ratio.

this method, not only the influence of noise is determined but the full reconstruction chain is tested.
The electric field traces are simulated with the same procedure as described in section 6.2. The only difference is that the noise level for each polarisation is adjusted individually following the SNR of the measured event for that polarisation. Thus, the correct signal distribution onto the three $\vec{E}$-field components is reproduced in the simulation.

The result, exemplary for one station of one event, is shown in figure 6.12. As uncertainty on the signal amplitude we define the standard deviation of the signal height distribution (fig. 6.12 left). Note that the change of the mean is small compared to the spread and, thus, will be neglected.
The expectation for the Lorentz-angle, the angle between Lorentz force and electric field, is zero as we have generated the $\vec{E}$-field traces to follow geomagnetic emission. As uncertainty on this quantity the maximum of a Rayleigh function, fitted to the distribution, is used (cf. fig. 6.12 right).

6.4 Polarisation of Electric Field

Different emission processes of radio signals from extensive air showers can be distinguished by the polarisation of the electric field measured at the radio stations. See chapter 2.3 for a detailed description of the different emission processes.

The dominating geo-magnetic emission process is due to the deflection of charged particles by the Lorentz force in the magnetic field of the earth. Thus, a polarisation in the direction of the Lorentz force is expected. For the Lorentz force holds

$$\vec{F} \propto \vec{n} \times \vec{B}, \tag{6.10}$$

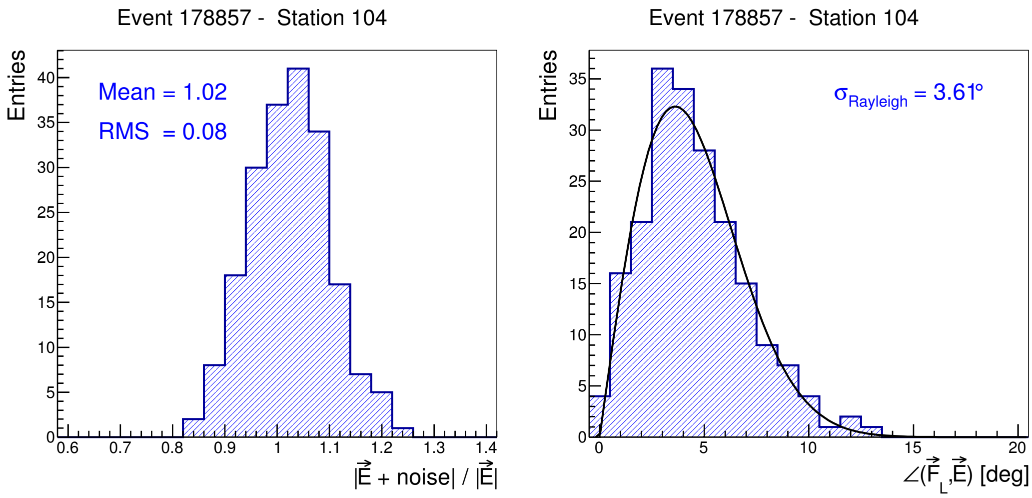

Figure 6.12: (*left*) Influence of noise on the signal amplitude. (*right*) Influence of noise on the direction of the $\vec{E}$-field vector. In this simulated $\vec{E}$-field traces the direction of the $\vec{E}$-field vector was defined to point into the direction of the Lorentz force. Hence, the expectation for $\angle(\vec{F}_L, \vec{E})$ is zero. A Rayleigh function is fitted to the distribution. The maximum of this function is taken as uncertainty on the direction of the $\vec{E}$-field vector.

where $\vec{B}$ is the magnetic field vector at AERA site and $\vec{n}$ is the shower axis. The electric field points into the same direction as the Lorentz force. Thus, the expected polarisation of the electric field depends only on the arrival direction of the air shower and can be calculated.

Figure 6.13 visualises the expected polarisation due to geomagnetic emission. In this polar skyplot each arrow represents the polarisation for a specific arrival direction. The arrows are the x,y projection of the electric field in an underlying Cartesian coordinate system. The z component is colour coded. The emission strength depends on the angle α between shower axis and magnetic field[8] which is visualised by the length of the vector.

The electric field vector measured in each radio station (cf. chapter 4.4) can now be compared to the expected polarisation. In the skyplot in figure 6.14 left, the measured polarisation of the cosmic ray events in our data set is shown. The black arrows are the projections of the measured $\vec{E}$-field vectors on the x-y plane. At each incoming direction, at least three arrows are plotted above each other (each event consists of at least three radio stations). We observe that the electric field exhibits a strong polarisation and is in good agreement to the expectation due to geomagnetic emission (red arrows).

To quantify this effect, the three dimensional angular distance between the theoretical and measured $\vec{E}$-field vector is calculated. The resulting values for the angle to the Lorentz force can be seen in the histogram of figure 6.14 right. Most events have

[8] cf. eq. 6.10 and note that $|\vec{a} \times \vec{b}| = |\vec{a}|\ |\vec{b}|\ \sin(\alpha)$

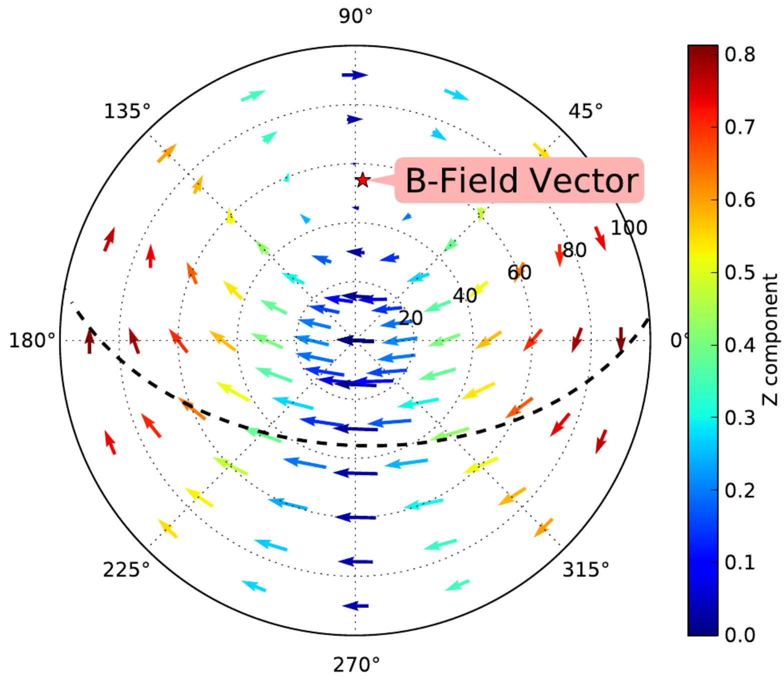

Figure 6.13: Skymap of the polarisation of radio pulses due to geomagnetic emission ($\vec{n} \times \vec{B}$). From Ref. [89].

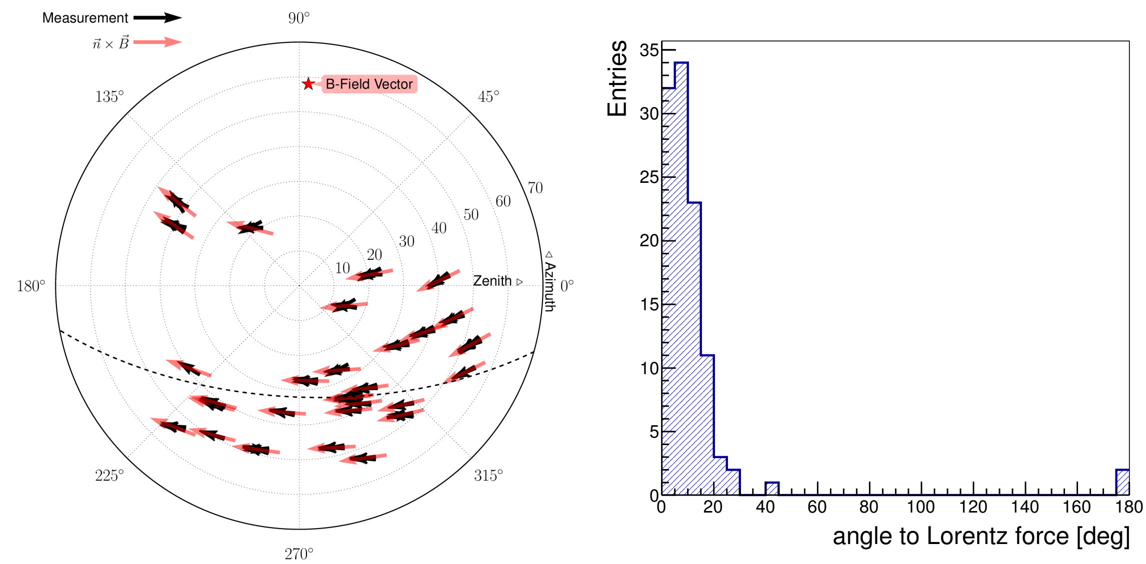

Figure 6.14: (*left*) Skymap of the polarisation of measured radio events compared to the expected polarisation due to geomagnetic emission ($\vec{n} \times \vec{B}$). From Ref. [90] (*right*) Angle between electric field vector and Lorentz force.

very small angles which show that geomagnetic emission is indeed the dominating process.

An interesting feature is that most events have an angle to the Lorentz force close to 0° but only two events have a Lorentz angle of 180°. This means that these two $\vec{E}$-field vectors are flipped by 180° compared to the other vectors (cf. chapter 4.4 and fig. 4.7). Thus, the direction of the first oscillation of the electric field is the same for almost all events.

The small deviation from the geomagnetic expectation can have various reasons. First, the direction of the electric field vector can only be measured up to some precision because the true signal is influenced by noise. Figure 6.15 left shows that the uncertainty of the angle to the Lorentz force varies between 1° and 5° for most events of our data set.

Relating the uncertainty of the direction of the electric field vector due to noise to the angular distance to the Lorentz force shows that the observed polarisation can not be explained solely with the geo-magnetic effect (cf. fig. 6.15 right).
This indicates that other second order emission processes exist that have a different polarisation signature. As the emission strength of geomagnetic emission decreases for incoming directions with smaller angles to the magnetic field, the fraction of other emission processes becomes larger. One possible explanation is the charge excess emission process that show a radial polarisation with respect to the shower axis. A different analysis has determined the charge excess fraction to $\sim$12% for incoming direction perpendicular to the magnetic field of the earth [40].

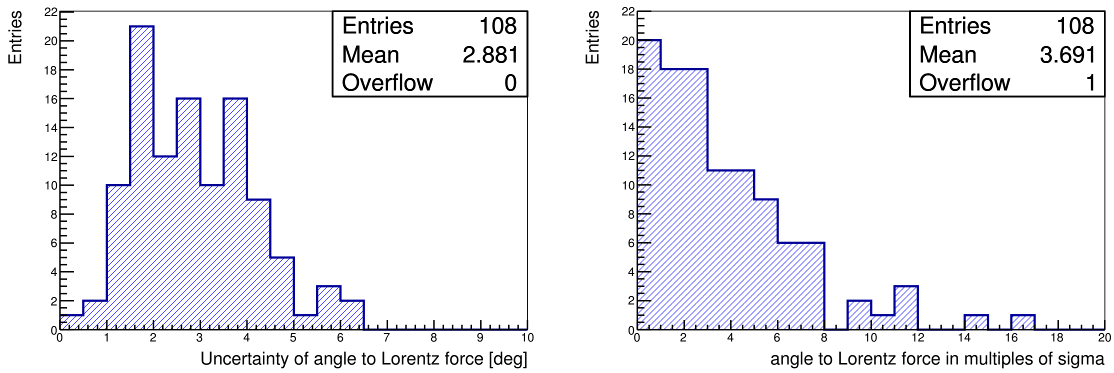

Figure 6.15: (*left*) Uncertainty of the angular distance between electric field vector and Lorentz force for all events used in this analysis. (*right*) Deviation of the Lorentz angle from the geo-magnetic expectation expressed in multiples of the individual uncertainty of the Lorentz angle.

7. Energy Measurement

In this chapter, the measured radio signal is correlated with the cosmic ray energy. Therefore, a radio energy estimator is developed and its uncertainty is determined thoroughly. Finally, the radio energy estimator is calibrated with the cosmic ray energy information from the surface detector.

For this analysis all cosmic ray radio events that have been measured in coincidence with the surface detector and satisfy the quality cuts mentioned in chapter 5 are used.

7.1 Method

The basis of this analysis is the reconstructed electric field vector (cf. chapter 4.4) which is reconstructed using the software framework $\overline{\text{Off}}\underline{\text{line}}$:

First, the air shower is reconstructed with the standard observer pipeline[1] using the surface detector informations. Second the reconstruction using the radio detector is performed. Upsampling by a factor of five is applied and narrowband noise sources are filtered out using the standard configuration of the RdChannelBandstopFilter module. For the reconstruction of the electric field, the needed arrival direction of the air shower is taken from the surface detector reconstruction[2]. Thus, the RdAntennaChannelToStationConverter[3] is configured to read the shower axis from the SD reconstruction.

7.1.1 Correction for Incoming Direction

The dominating emission process of radio emission from extensive air showers in the bandwidth of AERA[4] is the geo-magnetic effect (cf. [40] or chapter 6.4). This emission process implicates that the emission strength depends on the angle α between shower axis and the earth's magnetic field. This is taken into account by dividing the electric field amplitude by $\sin\alpha$ (cf. eq. 2.9).

[1] "Observer" is the name of the standard reconstruction of the surface detector.

[2] This is advantageous because a time calibration the AERA stations is not yet realized. Therefore the time resolution is currently in the order of tens of nanoseconds which lead to a worse angular resolution compared to the SD reconstruction.

[3] This $\overline{\text{Off}}\underline{\text{line}}$ module reconstructs the electric field.

[4] 30 MHz to 80 MHz

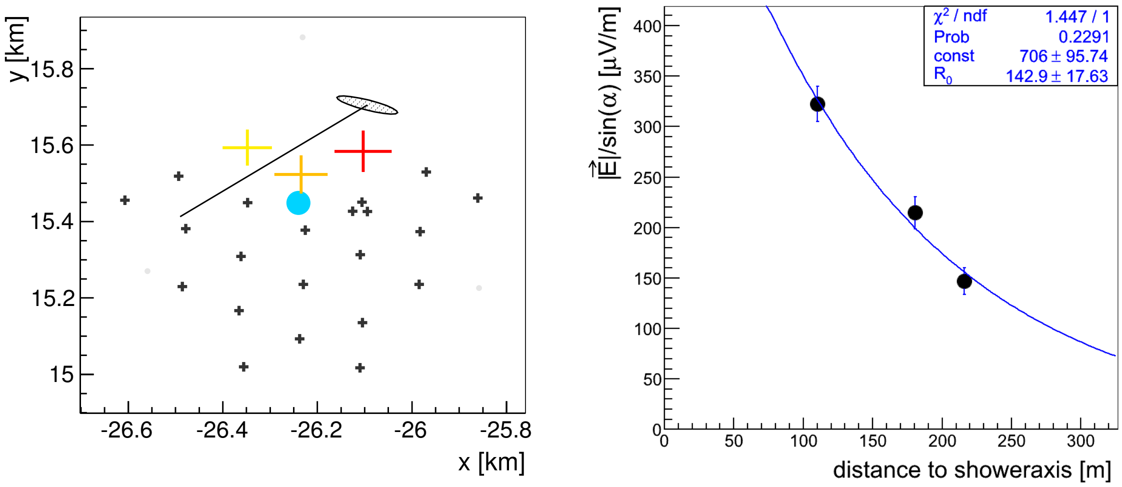

Figure 7.1: (*left*) Map of one of the coincident events. The AERA stations are marked as black crosses, the big coloured crosses are the three triggered stations (colour coded is the signal time). The blue dot is a SD tank. The dashed ellipse is the shower core with uncertainties and the black line the shower axis from the SD reconstruction. (*right*) Lateral signal falloff of one of the coincident events used in this analysis. An exponential function with two free parameters is used to interpolate between the data points. The determination of the error bars are explained in section 6.3.1.

7.1.2 Definition of Energy Estimator

As proper energy estimator we have to relate the corrected signal strength to some specific distance D_0 from the shower axis. The radio signal is measured only at discrete positions (the positions of the radio stations) as can be seen in the map of the AERA array in figure 7.1 left. Hence, for each event the radio stations have different distances to the shower axis.

Thus, it is indispensable, to interpolate between the data points. To describe the lateral signal falloff, we use an exponential function with two free parameters (ε_{D_0} and R_0):

$$\frac{|\vec{E}|}{\sin(\alpha)} = \varepsilon_{D_0} \cdot exp\left(-\frac{(D - D_0)}{R_0}\right) \tag{7.1}$$

The variable D_0 is the distance where the function should be evaluated. Then, ε_{D_0} is the value of the function (eq. 7.1) at position D_0 and the uncertainty on this quantity can be obtained directly from the fit.

The exponential function is a good choice in our case: Above a certain distance to the shower axis one would expect an an exponential falloff[5]. Furthermore, most events have only three to four stations why it is impossible to fit functions with more free parameters.

[5]Recent results from the LOFAR experiment indicate that above a distance to the shower axis of ∼100 m the signal drops exponentially [91].

Figure 7.1 right shows an example of such an interpolation. In this plot, the signal strength corrected for the incoming direction is plotted versus the perpendicular distance to the shower axis. Finally, we define the energy estimator as the corrected signal strength at distance D_0 (which is the fit parameter ε_{D_0}). This estimator will then be calibrated with the surface detector.

7.2 Uncertainties

Besides the uncertainty on the signal height which is obtained via simulations as described in chapter 6.3.1, other uncertainties enter into this analysis and are described in this section.

7.2.1 Energy Estimator

The energy estimator ε is defined as the corrected signal strength at a specific distance D_0 from the shower axis and, hence, is the parameter ε_{D_0} of the exponential function fitted to the lateral signal distribution.

The dominating uncertainty on the energy estimator is not the fit uncertainty on this parameter but the uncertainty of the shower core. As visible in figure 7.1 left as dashed error ellipse, the uncertainty can be relatively large compared to the distance of the radio stations to the shower core. This uncertainty is not a statistical error on the distance to the shower axis in the LDF fit (cf. fig. 7.1 right) but has a systematic effect depending on the geometry of the event.

To account for this uncertainty, the shower core and the incoming direction is varied 500 times within its uncertainties. For each realisation of the shower core and incoming direction, the exponential interpolation of the lateral signal falloff is redone and the energy estimator is determined. Figure 7.2 shows three examples of the change in the lateral signal falloff only due to the variation of the shower core.
The resulting distribution of the energy estimator ε_{110m} at distance $D_0 = 110$ m for this example event is shown in figure 7.3 left. The red line is the value obtained for no variation of the shower core. The standard deviation of this distribution is used as uncertainty of the energy estimator.

This error estimation is justified because the individual errors on ε_{110m} from the exponential fit are always smaller than the uncertainty due to the variation of the shower core as visible in figure 7.3 right for this example event.

The variation of the shower core can have the effect that a LDF plot that first does not show a monotone falloff changes in such a way that it can be described well by an exponential function. However, this is not true for all events. For a few events, the LDF plot looks still peculiar. The observed pattern is that the signal strength does not decrease with greater distance to the shower axis but jumps from a low signal to a high signal and back to a low signal. The jump size can be up to a factor of three of signal strength.

To quantify if the lateral signal falloff could be described by an exponential function including the impact of the imprecise shower core, we calculate the χ^2 probability

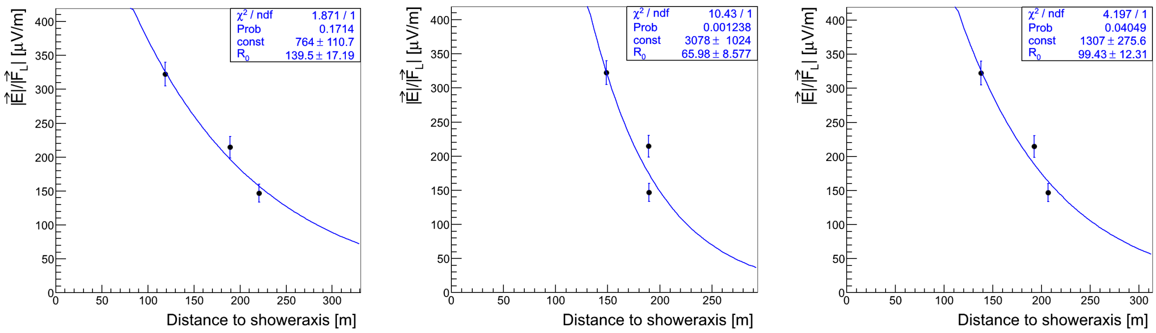

Figure 7.2: Different LDFs due to variation of the shower core.

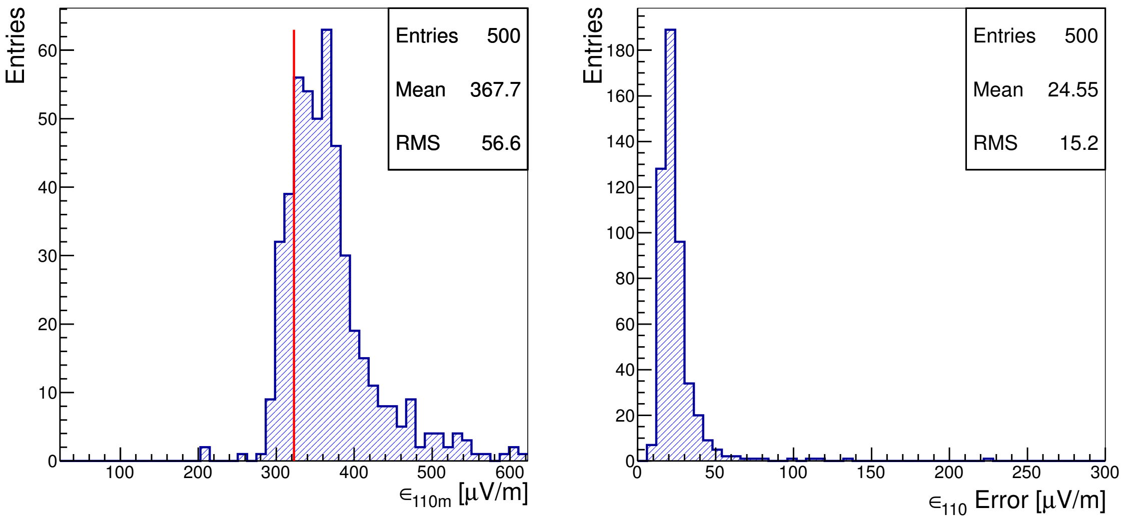

Figure 7.3: (*left*) Variation of the energy estimator due to the shower core uncertainty for event 178857. The shower core (and shower axis) is varied 500 times within its uncertainties. For each realisation the energy estimator is determined and shown in this histogram. The RMS is taken as uncertainty on ε. The red line is the value of the energy estimator if the shower core is not modified. (*right*) The individual error on the energy estimator obtained from the exponential fit. The individual errors are small compared to the variation due to the shower core uncertainty.

of the exponential fit. The uncertainty on the shower core is translated to an error on the distance to the shower axis using Monte Carlo technique. This error is then used as statistical error on the x-coordinate in the χ^2 probability calculation. Note that in the fit x-errors are not considered but only in the χ^2 probability calculation. All events with a χ^2 probability smaller than 10^{-6} are rejected. Four events do not pass this additional quality cut[6].

[6]The LDFs of these events can be found at http://www.c-glaser.de/physik/EnergyEstimation/LDFs.php?q=/rejected (This page is restricted to members of the Pierre Auger collarboration).

7.2.2 Other uncertainties

The uncertainty of the incoming direction of the air shower (the shower axis) has various influences. First, a change in the shower axis will end up in a change in the electric field as the antenna pattern is evaluated at a different position. Second, this uncertainty has an impact on the angle between shower axis and magnetic field. Thus, the correction of the signal amplitude for the incoming direction changes (cf. chapter 7.1.1). The third effect, which is already considered in the Monte Carlo error estimation of the energy estimator, is the change of the distance between shower axis and radio station.

The shower axis is obtained from the surface detector reconstruction that has an angular resolution of better than 1.5° [92]. This small uncertainty, compared with the uncertainty due to noise on the signal height and the uncertainty on the core position, makes this effect negligible.
The fact that we use the directional reconstruction of the surface detector instead of the radio detector has the advantage that the time uncertainty of the AERA stations does not have an influence on our analysis.

Another uncertainty that is neglected in this analysis is the one on the simulated antenna pattern. Measurements have shown that the simulated pattern describes our antenna well and only for some frequencies a shift in the gain of less than 20% is observed [5].

7.3 Energy Calibration

The energy estimator is defined as the corrected signal strength at distance D_0 from the shower axis. To retrieve the signal at distance D_0, the lateral signal falloff is interpolated with an exponential function. Figure 7.1 right and A.5 show examples of this interpolation[7] and figure A.6 the resulting slope parameters of the exponential function.

Until now, we do not have specified at which distance D_0 the energy estimator should be evaluated. A priori, it is unclear which distance will be best. Therefore, different distances are tested. For each definition of the energy estimator, a calibration with the energy measured by the surface detector is performed. To parametrise this correlation, a power law[8]

$$E_{Rd} = const. \cdot (\varepsilon_{D_0})^m \tag{7.2}$$

is fit to the data. Thus, for each event the energy can be calculated from the radio part. As a measure of quality we define the relative energy resolution as

$$\frac{E_{SD} - E_{Rd}}{E_{SD}}. \tag{7.3}$$

[7]The LDF plots for all events can be found at http://www.c-glaser.de/physik/EnergyEstimation/LDFs.php (This page is restricted to members of the Pierre Auger collarboration).

[8]which is a straight line on a double-logarithmic scale

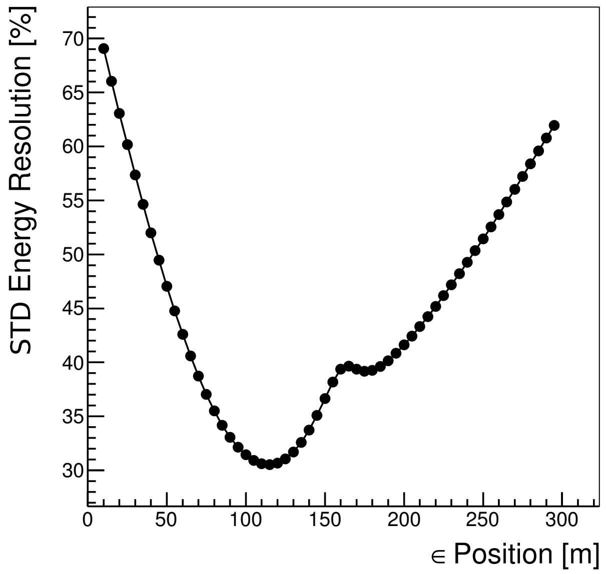

Figure 7.4: Scan for the best distance D_0 for the energy estimator. The corrected signal strength at 110 m leads to the best energy resolution.

For each distance D_0 the standard deviation of the obtained distribution of the energy resolution is calculated (individual event uncertainties are not taken into account). Figure 7.4 shows the result of the scan for the best value for D_0. We find that a distance $D_0 = 110$ m leads to the best energy resolution.

On a closer inspection of figure 7.4, a second minimum at about 180m is observed. This might be a hint that a distance of 110 m is not the best choice for all events in our data set. Simulations suggest [93] that the optimal distance depends on the zenith angle. Showers with a small zenith angle prefer smaller distances.
To study this effect, the data set has to be splitted into subsamples with different zenith angles. A first look at our data actually indicates this effect but the statistic is too low to make a reliable statement. However, we anticipate to be able to study this effect in detail with increasing statistics soon.

With the knowledge of the optimal distance for the energy estimator, we perform the final calibration with the cosmic ray energy measured by the surface detector. In figure 7.5 left, the energy measured by SD is plotted versus the energy estimator at a distance $D_0 = 110$ m and a power law (eq. 7.2) is fitted to the data. The result of the calibration fit is:

$$\log_{10}(E_{SD}/eV) = (1.02 \pm 0.05) \cdot \log_{10}\left(\frac{\varepsilon_{110m}}{\mu V/m}\right) + (15.01 \pm 0.14) \tag{7.4}$$

$$\Rightarrow E = (1.10 \pm 0.35) \cdot 10^{15} \cdot \left(\frac{\varepsilon_{110m}}{\mu V/m}\right)^{1.02 \pm 0.05} eV \tag{7.5}$$

This means that the radio signal amplitude scales linear with the cosmic ray energy which is consistent with the results of other radio experiments [35, 37, 38, 94].

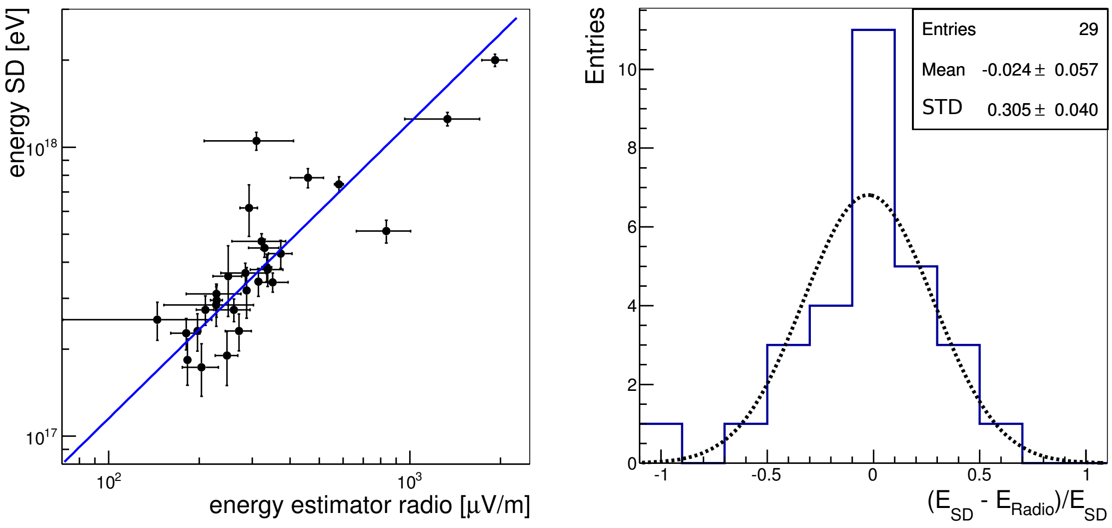

Figure 7.5: (*left*) Energy Calibration: The energy estimator is calibrated with the cosmic ray energy measured by the surface detector. A power law is fit to the data. The χ^2/ndf is 2.0. (*right*) Relative Energy Resolution. The dashed curve is a Gauss function corresponding to the mean and standard deviation of the distribution.

The obtained energy resolution can be seen in figure 7.5 right. We use the standard deviation of this distribution of 0.305 ± 0.04 as an estimate of the obtained energy resolution. The normal distribution shown in this plot (dashed line) uses these parameters. A binned fit of a Gaussian function leads to a smaller width of $\sigma \cong 0.25$ as reported in [95]. Because of the low statistics, the result of the fit depends on the binning of the histogram and is hence not a stable estimator.

We conclude that we have obtained an energy resolution of $\sim$31% including the surface detector uncertainty. This is, of course, an upper limit on the possible achievable energy resolution. We expect to improve the energy reconstruction by refining the analysis with increasing statistics soon.

8. Trigger Strategy using Wavelet Technique

In this chapter a new trigger strategy using wavelet technique is described. The general idea is to expand the measured radio signal into its wavelet coefficients and compare these coefficients to the expectation for cosmic ray radio signals.
In the first section the theory of the continuous wavelet transformation is introduced shortly. Then, the method and the implementation into $\overline{\text{Off}}\underline{\text{line}}$ is described. Finally, we determine the background reduction rate that can be achieved by this method and apply this method to search for cosmic rays signals in our data set.

8.1 Continuous Wavelet Transformation

A wavelet transformation is the decomposition of a time-signal into wavelet functions of a certain family. As wavelet comes from the French word *ondelette* meaning "small wave", a wavelet function is a time limited oscillation. Wavelet functions have special properties. One of the most important ones is that a wavelet function is limited in time and frequency (see fig. 8.1 for an example). Thus, by expanding the time signal into its wavelet coefficients the time dependent frequency content can be observed. This is in contrast to a Fourier transformation which decomposes the signal into time-unlimited sine functions.

Many different wavelet function families are available that satisfy these requirements. The wavelet families differ mainly in their localisation in the time and frequency spaces. Due to the Heisenberg uncertainty principle, a function can not be arbitrarily well localised in both domains. A narrow localisation in the time domain leads to a broad frequency content and, contrarily, a narrow frequency content leads to a broad localisation in the time domain.
Hence, depending on the specific wavelet function that is used for the transformation one obtains a good time resolution of the wavelet coefficients at the expense of frequency resolution, vice versa or a compromise between those extremes.

The wavelet transformation of a function $x(t)$ with the complex wavelet function Ψ can be expressed as follows:

$$X_{a,b} = \frac{1}{\sqrt{a}} \int_{-\infty}^{+\infty} x(t) \cdot \Psi^* \left(\frac{t-b}{a} \right) dt \quad . \tag{8.1}$$

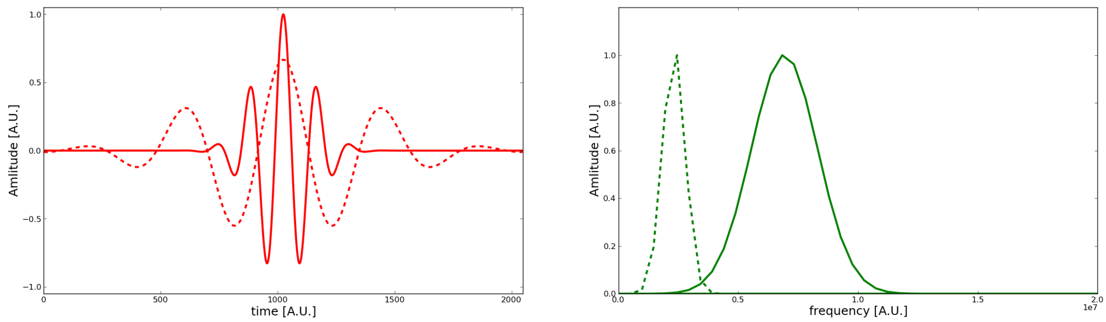

Figure 8.1: Plot of the Morlet wavelet in time (left) and frequency (right) domain. In the time domain only the real part of the function is shown. The solid line is the "Mother" wavelet with the scaling parameter $a = a_0 = 1$. The dashed line is a "child" wavelet with a different scaling parameter $a > a_0$. One observes that the frequency content of a wavelet function with scale a is centered around a certain mid-frequency which can be calculated from a. The width of the frequency resolution gets smaller for higher values of the scale a (i.e. a smaller mid-frequency) while the relative frequency resolution $\frac{\Delta f}{f}$ remains constant.

The parameter $b \in \Re$ is the translation in time of the wavelet function Ψ and $a \in \Re, a > 0$ is the scaling parameter which is anti proportional to the frequency content of the wavelet function.

In this analysis the complex Morlet wavelet family will be used, which offers a good compromise between time and frequency resolution. Mathematically, the Morlet wavelet is a plane wave localised with a Gaussian window [96]:

$$\Psi(t) = e^{i\omega_\Psi t} \cdot e^{-t^2/2}, \tag{8.2}$$

where $\omega_\Psi \in [5, 6]$ is a constant.

From the so called *mother* wavelet different *child* wavelets can be obtained by shifting the hole function in time or rescaling the function by varying the scaling parameter a:

$$\Psi_{a,b} = \frac{1}{\sqrt{a}} \cdot \Psi\left(\frac{t-b}{a}\right) \quad . \tag{8.3}$$

In fig. 8.1 the time and frequency domain of the Morlet wavelet is shown. A change in the scale parameter a leads to a different frequency content (dashed line). Each scale parameter a can be related to a different mid-frequency f_0. The relative frequency resolution $\frac{\Delta f}{f}$ remains constant but the whole frequency content changes to smaller frequencies when the scale parameter a increases.

Note that the scaled and shifted *child* Morlet wavelets do not form a orthogonal system. In principle, it is possible to construct orthogonal wavelet functions but this approach is not suitable for this work.

Figure 8.2 shows a simple example of a wavelet transformation using the Morlet wavelet.

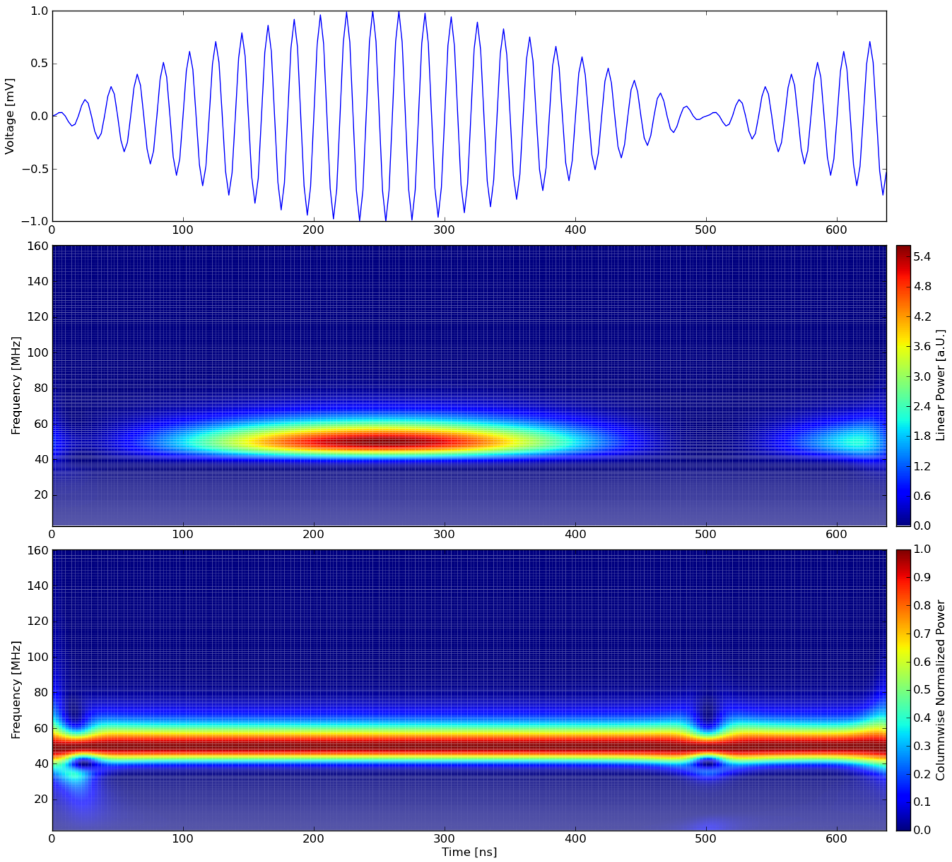

Figure 8.2: A simple example of a continuous wavelet transformation using the Morlet wavelet function: In the upper plot a sine function modulated with another sine function is shown. In the middle plot the power of the complex wavelet coefficients (color coded) for different times and frequencies (scales) are shown. The different scales are here converted to the mid-frequency to have a physically meaningful quantitiy. The frequency of the sine function of 50 MHz is recovered within the frequency resolution. At times where the amplitude of the sine function is small the power of the wavelet coefficients is, of course, also small. In the lower plot each column is normalized to one to see the frequency content even at times where the amplitude of the sine is small.

8.2 Method

In the upper plot of fig. 8.3 the electric field trace of one of the cosmic ray events recorded with AERA is shown. The $\vec{E}$-field trace was upsampled by a factor of four and has a very good signal to noise ratio. Hence, the signal originating from a cosmic ray is clearly visible.

The length of the $\vec{E}$-field trace on which the wavelet transformation is performed is 650 ns. The sampling rate of the detector is 200 MHz. With the upsampling factor of four this leads to $128 \cdot 4 = 512$ time bins.

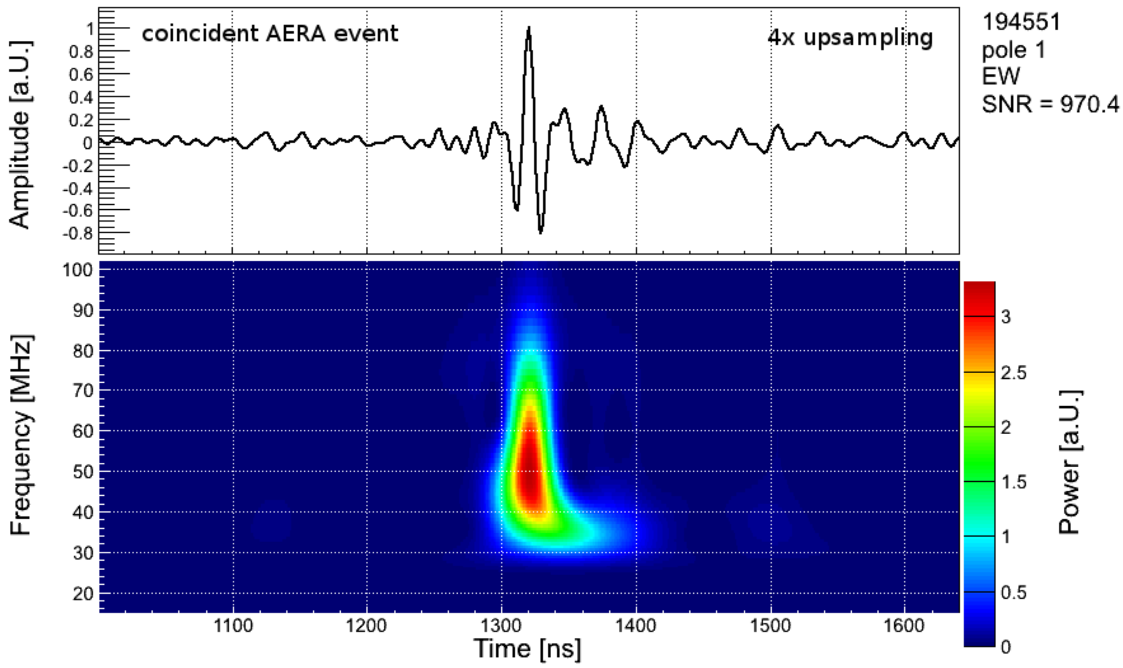

Figure 8.3: (*top*) $\vec{E}$-field trace of a cosmic ray radio event. (*bottom*) Wavelet coefficient of the above $\vec{E}$-field trace. The power of the complex wavelet coefficient is displayed colour coded.

The wavelet coefficients are calculated via eq. 8.1 for different values of the translation in time b and scale a[1]. The scale a corresponds to a specific frequency content of the wavelet function (cf. fig. 8.1). High wavelet coefficients for scale a_i mean that the corresponding frequencies are contained in the signal. To have a physically meaningful quantity the scale is translated to its mid-frequency.

The lower plot of fig. 8.3 shows the power[2] of the complex wavelet coefficients colour coded for the different times and frequencies (scales). One observes high amplitudes in the wavelet coefficients at the time where the pulse occurs and a frequency content of approx. 30 MHz to 80 MHz which is the bandwidth of the AERA detector.

The time and frequency dependency of the wavelet coefficients exhibit a special shape (fig. 8.3 bottom) which will be used as discriminator between cosmic ray signals and noise pulses. The general idea of this method is to compare the wavelet expansion of a measured signal pulse with the expectation for a cosmic ray signal. The better the similarity, the more likely is that the measured signal originates from a cosmic ray induced air shower.

Expectation of a CR radio pulse

The expected signal shape for a cosmic ray radio signal is determined by averaging over the reconstructed electric field traces of all high quality events (SNR $>$ 200)

[1]Actually the wavelet coefficients are calculated in fourier space where the convolution transforms in a simple multiplication.

[2]Power means the norm squared.

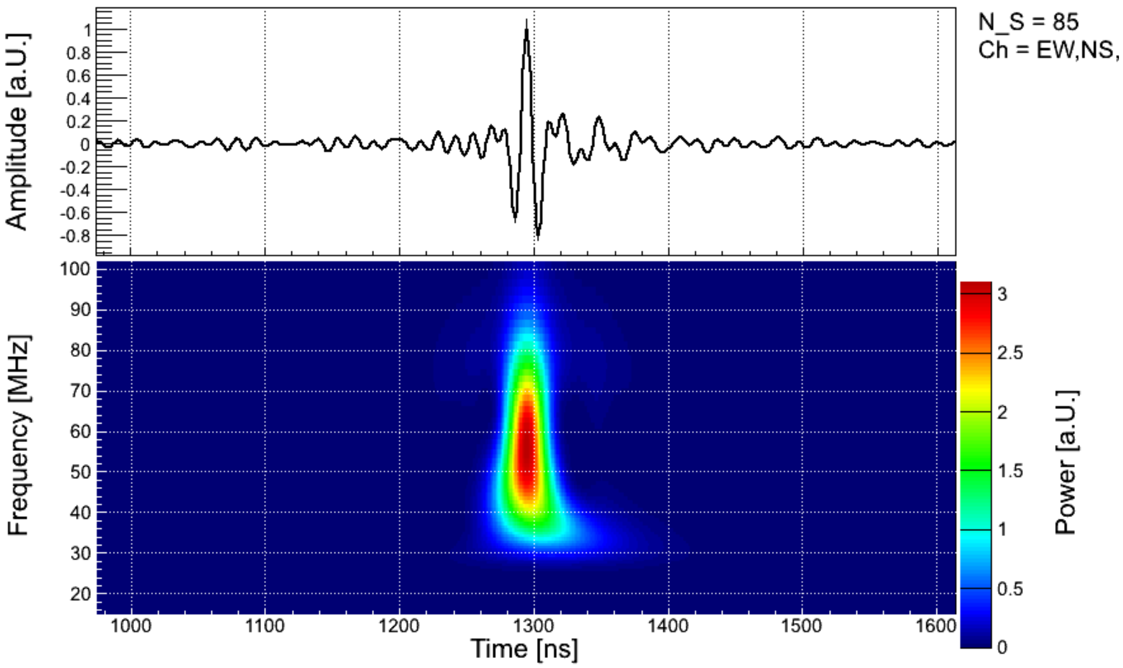

Figure 8.4: (*top*) Mean cosmic ray electric field trace. (*bottom*) Wavelet expansion of the mean cosmic ray $\vec{E}$-field trace using the Morlet wavelet.

that have been measured in coincidence with the surface detector. This approach has the advantage that it is independent on theoretical assumptions about the pulse form. On the other hand, a potentially downside is that the station trigger may have been sensitive to specific pulse forms. Consequently, this method is also sensitive only to a specific class of cosmic ray radio signals.
Figure 8.4 shows the mean cosmic ray $\vec{E}$-field trace and its wavelet expansion.

Calculation of Wavelet Similarity

To determine the similarity between a measured radio pulse and the mean cosmic ray radio pulse, both signals are expanded into its wavelet coefficients. Then, we simply subtract the power of the wavelet coefficients from each other and add up the square of each difference:

$$\text{wavelet similarity} = \sum_{iScale=minScale}^{maxScale} \sum_{iTime=0}^{maxTimeBin} (M_{iScale,iTime} - CR_{iScale,iTime})^2, \quad (8.4)$$

where M is the power of the wavelet coefficients of the measured $\vec{E}$-field trace and CR is the power of the wavelet coefficients of the mean cosmic ray $\vec{E}$-field trace.
One can visualize this process in the following: The wavelet expansion of a time signal can be thought of a 2-dim. matrix (see fig. 8.4 bottom). Then, the matrix of the measured pulse is subtracted from the matrix of the mean cosmic ray pulse. All components of the resulting matrix are summed up quadratically which gives the wavelet similarity.

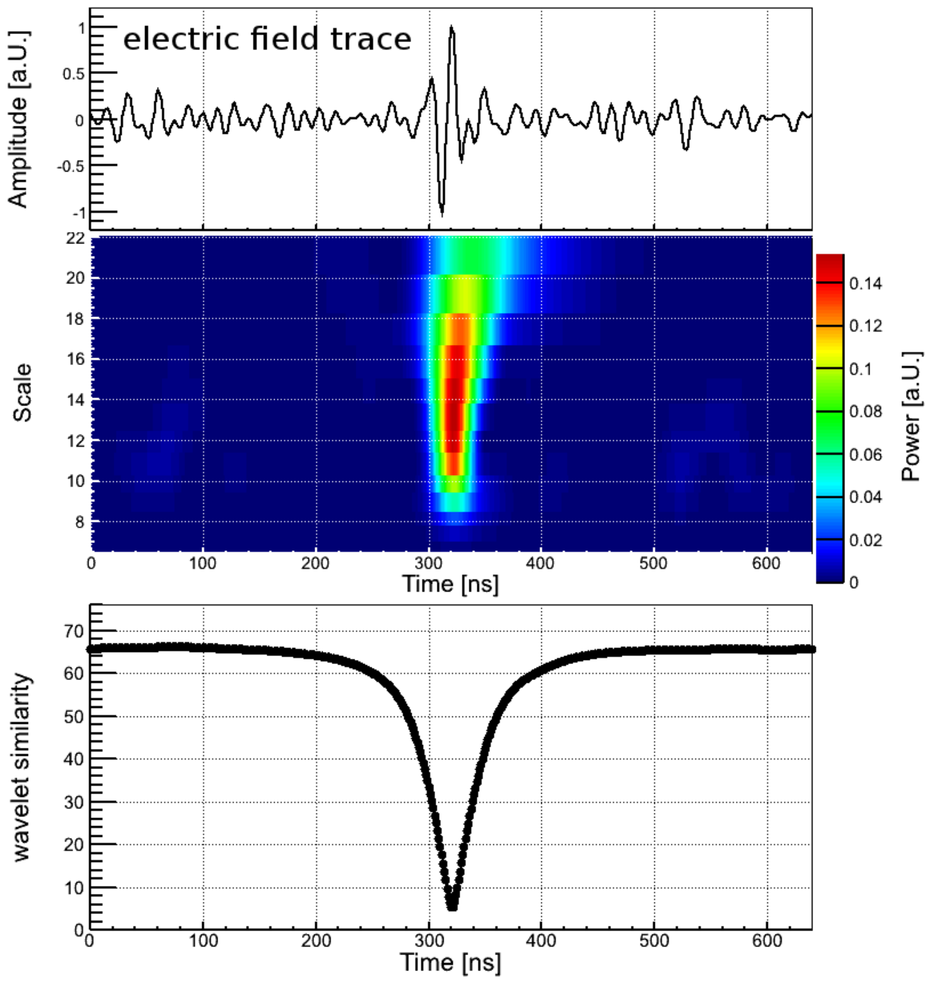

Figure 8.5: (*top*) $\vec{E}$-field trace of a cosmic ray radio event. (*middle*) Wavelet transformation of the above displayed $\vec{E}$-field trace using the Morlet wavelet as implemented in Offline. The scales are not converted into the corresponding mid-frequencies. Colour coded is the power of the complex wavelet coefficients. (*bottom*) Scan for the best wavelet similarity.

This approach will only lead to the lowest possible similarity value if the maxima of the radio pulses are exactly at the same position which is not always the case. To overcome this problem one matrix is shifted along the time axis and for each shift the similarity is calculated. Figure 8.5 shows the result of such a scan. The minimum value is used as the similarity for this event.

A priori, the value of the wavelet similarity has no significant meaning because the value depends on the normalization of the $\vec{E}$-field trace and the frequency and time binning of the wavelet coefficients. A measure of what is a "good" similarity can be obtained when analysing the radio events that have been measured in coincidence with SD. From these events we know that the radio pulse originates from a cosmic ray. Thus, the wavelet similarities of those events determine what a "good" similarity means.

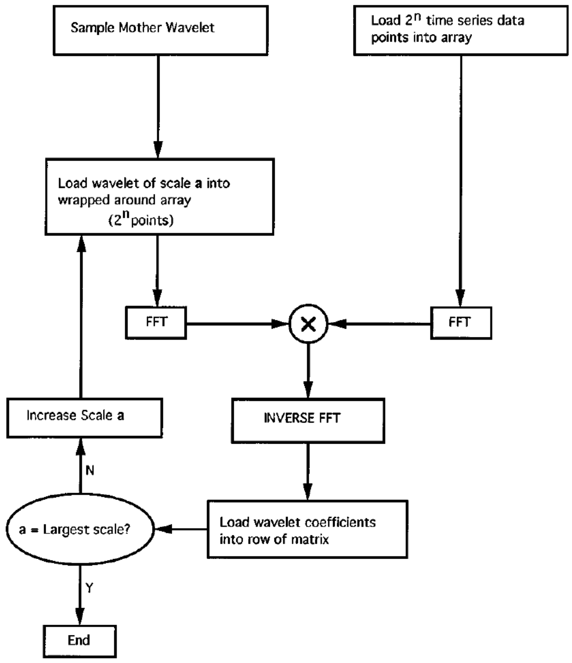

Figure 8.6: Block diagram of the implementation of the continuous wavelet transformation. Image from [96].

8.3 Implementation to Offline

We implemented the continuous wavelet transformation and the calculation of the wavelet similarity into $\overline{\text{Off}}\underline{\text{line}}$. Thereby, we orientate on a suggestion given in [96]. The implementation is performed such that all parameters are configurable through a xml-file. The concrete numbers that are given are the ones used in the later analysis.

The calculation of the wavelet coefficients is most efficiently performed in Fourier space, because there equation 8.1 becomes a simple multiplication. For that reason, the size of the signal trace should be a power of two. We use a signal window of 640 ns centred around the pulse position. With a sampling rate of 5 ns and an upsampling by a factor of four this leads to $\mathrm{N}_{\mathrm{time}} = 128 \cdot 4 = 512 = 2^9$ time bins. The maximum pulse height is normalized to unity.

The algorithm is illustrated in the block diagram in figure 8.6. For each scale a the Fourier transform of the (Morlet[3]) wavelet function is multiplied with the Fourier transform of the signal trace:

$$\tilde{X}_{a,i} = \tilde{T}_i \cdot \tilde{W}_{a,i}\,, \tag{8.5}$$

where $\tilde{X}_{a,i}$ is the complex wavelet coefficient in Fourier space of scale a and frequency bin i. $\tilde{T}$ is the signal trace in Fourier space and $\tilde{W}_{a,i}$ is the complex wavelet function. The wavelet coefficients for scale a in the time domain are obtained by the application of an inverse Fourier transformation:

$$\mathbf{X}_a = \text{inverse}\, FFT(\tilde{\mathbf{X}}_a)\,, \tag{8.6}$$

[3]The Fourier transform of the Morlet wavelet can be calculated analytically.

where $\mathbf{X}_a$ and $\tilde{\mathbf{X}}_a$ are lists of $\mathrm{N}_{\mathrm{time}}$ bins.

This is repeated for all scales a, resulting in $\mathrm{N} = \mathrm{N}_{\mathrm{time}} \cdot \mathrm{N}_{\mathrm{scales}}$ wavelet coefficients. The wavelet coefficients are in general complex numbers. We calculate the power, i.e. the norm squared, to obtain real valued coefficients. This is the matrix that is shown e.g. in figure 8.5 middle.

The number of scales is directly proportional to the computing time and data volume which requires particular notice of the scale sampling. The highest and lowest scale is chosen to correspond to the lowest and highest frequency of the bandwidth of AERA. However, a constant spacing of the scales within this interval is not reasonable because the relative frequency resolution of a wavelet function $\frac{\Delta f}{f}$ is constant (cf. fig 8.1). Thus, the spacing should increase with increasing frequency (i.e. decreasing scale). Calculating the scales via

$$a_i = K^{(i-1)}\,, \tag{8.7}$$

where K is a real number greater than one and $i \in \aleph^{\geq 0}$ consecutively numbers the scales a, ensures a sampling where the distance between two scales corresponds to the same frequency resolution.

Finally, the wavelet similarity (eq. 8.4) is calculated for different positions of the measured pulse position relative to the pulse position of the mean cosmic ray trace. This is the scan in figure 8.5 bottom. The lowest value is saved for later analysis.

8.4 Determination of Background Reduction Rate

The histogram in figure 8.7 left shows the wavelet similarity for all 62 fully reconstructable events measured in coincidence with SD (the coincident events). Each event consists of several stations. For the best $\vec{E}$-field trace (the polarisation with the highest SNR) of each station the wavelet similarity is calculated which leads to the 302 entries in the histogram. The two dashed lines indicate the 50% and 80% quantile at a wavelet similarity of 18.6 and 33.9 respectively, i.e. 50% of all measured cosmic ray $\vec{E}$-field traces have wavelet similarity of less than 18.6.

A few of the cosmic ray $\vec{E}$-field traces have a large value of wavelet similarity. Some outliers are due to a bad signal quality, i.e. the SNR of this trace is very low and the radio pulse is strongly influenced by noise. A SNR cut is not applied in this analysis to not bias the result to high quality events.
However, this situation can be improved by considering only the station with the best wavelet similarity. Naturally, some stations have a better signal quality than others, e.g. a station with a small distance to the shower axis has normally a stronger radio signal and is therefore less influenced by noise.
This approach is shown in the right histogram of fig. 8.7. The distribution has less outliers and of course in general smaller values for the wavelet similarity. The 50% and 80% quantile is now located at a wavelet similarity of 12.3 and 18.2 respectively.

The background reduction rate that can be achieved by applying a wavelet similarity cut can be determined by inspecting the wavelet similarity distribution for all background events. Therefore, we assume that all self-triggered events are background.

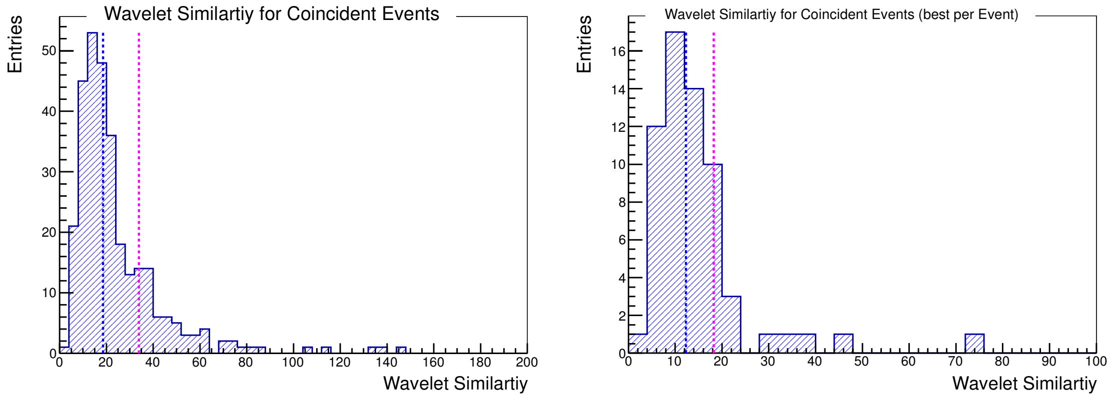

Figure 8.7: Wavelet similarity for coincident events. The dashed lines indicate the 50% and 80% quantile. (*left*) Wavelet similarity of each station trace. Histogram contains 302 entries. (*right*) Best wavelet similarity of each coincident event. Histogram contains 62 entries. Note the different x-axis range. Histograms do not contain overflow bins.

This assumption is justified because only a few cosmic ray events per day are expected but the average trigger rate is a few hundred thousands a day (cf. fig A.7). Thus, the cosmic ray events make a negligible percentage in the whole data set. Figure 8.8 left shows the wavelet similarity distribution for all background events (red histogram) together with the distribution for the coincident events. The background reduction factor for a cut value WS_{max} can be calculated via

$$\text{background reduction factor} = \frac{N}{N(WS < WS_{max})} \quad , \tag{8.8}$$

where WS is the wavelet similarity, N is the number of background events and $N(WS < WS_{max})$ is the number of background events with a wavelet similarity smaller than WS_{max}. For a cosmic ray efficiency of 80% (WS = 33.9) a background reduction by a factor of 4 and for a cosmic ray efficiency of 50% (WS = 18.6) a background reduction by a factor of 44 is achieved.

The background reduction can be improved significantly when considering only the best wavelet similarity per event. Figure 8.8 right shows that for a cosmic ray efficiency of 80% a background reduction by a factor of 17 is achieved. For a cosmic ray efficiency of 50% a background reduction of even a factor of 79 is gained.

Time Dependence of Background Reduction Rate

Figure 8.9 shows the time dependence of the obtained background reduction (note the logarithmic scale). Therefore, the data set is split into different parts. The splits are time ordered and such that the raw data volume per split is approximately the same but after the aforementioned cuts the number of events in each split can be different. The different parts belong to different runs. Thus, the individual trigger settings can vary from split to split.

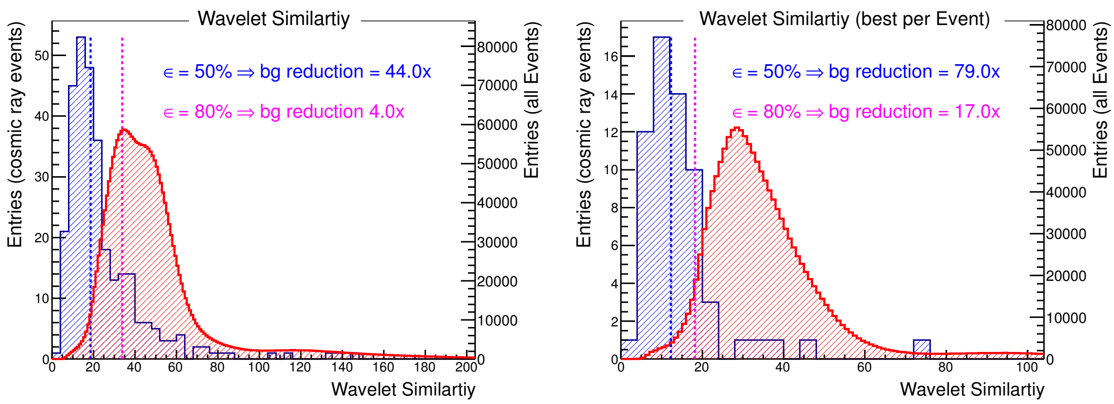

Figure 8.8: Wavelet similarity for coincident events (blue) and background events (red). The dashed lines indicate the 50% and 80% quantile. (*left*) Wavelet similarity of each station trace. (*right*) Best wavelet similarity of each event. Note the different x-axis range.

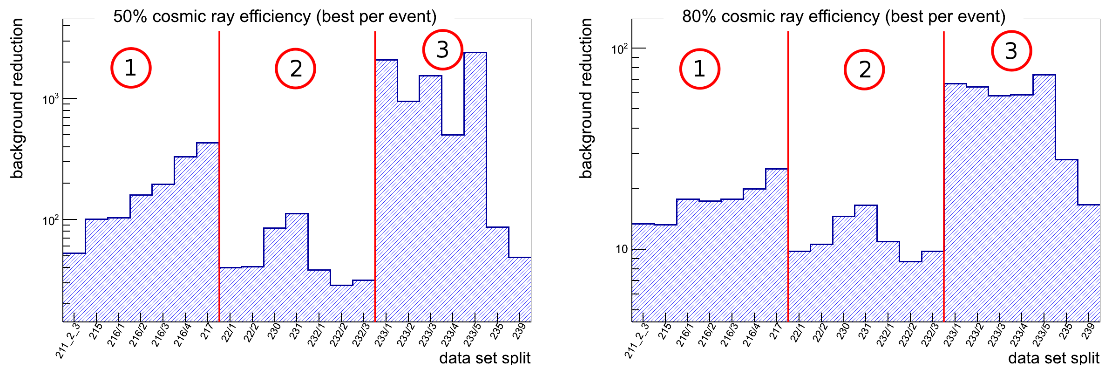

Figure 8.9: Time dependence of the background reduction rate. The data set is split up into 21 time ordered parts. The background reduction depends strongly on the specific time or run settings.

One observes that the data set can be roughly divided into three different regions as depicted in figure 8.9. For the first region, a relatively good background reduction rate of a factor of at least 100 can be achieved. Furthermore, the first region contains all 16 coincident events that are available in the whole data set considered in this chapter.
The second region shows a very low background reduction rate and the third region a very high background reduction rate.

Two possible explanations for this behaviour are the followings:
The noise sources that make the dominant contribution to the triggered events are not constant in time. The low background reduction rate in region two can thus be due to a new dominant noise source for which the wavelet trigger is not sensitive.
The second possible explanation is different trigger settings in the three regions. Thus, for instance in the second region the trigger settings could be such that mostly pulse forms with a good wavelet similarity are recorded.

8.5 Search for Cosmic Rays

In this section the developed wavelet trigger will be used to find cosmic ray radio signals in our data set. As the energy threshold of the AERA detector is lower than the threshold of the surface detector, a lot of low energy cosmic ray events[4] should be contained in the data set that have not been identified as such.

As the obtained background reduction rate depends strongly on the time were the data was taken, the search for cosmic rays is restricted to region one (cf. fig. 8.9). This has the additional advantage that all coincident (i.e. events from which we know that they are cosmic rays) are contained in this region. Hence, the efficiency and purity of the following procedure can be estimated.

A good wavelet similarity as only criterion will be insufficient which can be seen directly from the background reduction rate. Even with a background reduction by a factor of several hundreds the trigger rate will still be approximately thousand times higher than the expected cosmic ray rate (cf. fig. A.7).

8.5.1 Geometry Discriminator

Most of the background events originate from a few noise sources at the horizon. The skymap of all self triggered events (fig 5.1) show that these events are often reconstructed towards smaller zenith angles. This is mostly due to particular geometrical configurations of the triggered radio stations. Figure 8.10 shows an example for such a configuration. All triggered radio stations are aligned on one of the symmetry axes of the detector. All incoming directions that lie on a circle around the symmetry axis will lead to the same timing pattern. Hence, the reconstruction will choose an arbitrary direction on this circle which results in the bow-like structures in the skymap.

These configuration can be rejected using the following algorithm:
The first two triggered stations define a straight line through the detector array. Then, the smallest distance from all other triggered stations to this straight line is calculated and added up. This sum is our geometry discriminator. An analysis in [5, chapter 10.3.1] showed that the exclusion of all events with a geometry discriminator smaller than 100 m safely rejects all stretched configurations.

Figure 8.11 shows a skymap of the rejected events and figure 8.12 the events remaining after this cut. All bow like structures are rejected but the hotspots at the horizon are still clearly visible. This cut rejects $\sim$10% of the events.

8.5.2 Cone Cut Algorithm

An efficient way to remove most of the transient noise sources is the so called cone cut algorithm. For cosmic rays, we expect a uniform distribution the arrival directions and a rate of only a few events per day. For most noise sources, we measure events with a high rate always coming from the same direction.

[4] In this context of UHECRs “low energy” means energies between 10^{16} eV and a few 10^{17} eV.

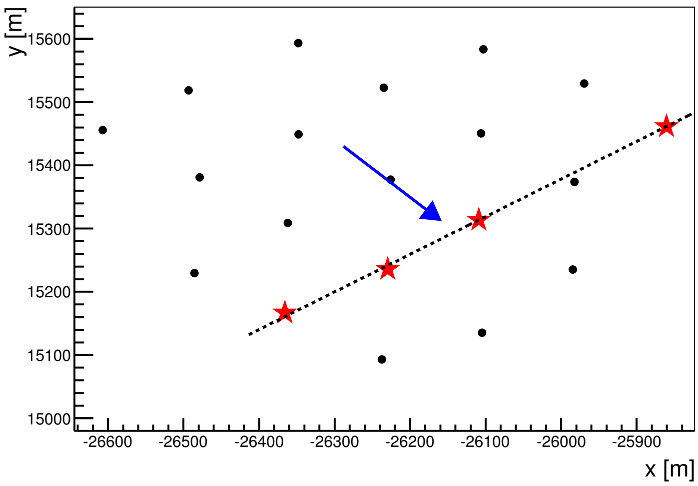

Figure 8.10: Example of a stretched station configuration. Black dots are all AERA radio stations. The red stars are the triggered radio stations. The blue arrow is the arrival direction of the air shower.

The idea of this algorithm is illustrated in figure 8.13. When two events arrive within a time t_C from approximately the same direction, both events are rejected. The algorithm has two parameters. The cone time t_C and the minimal allowed angular separation between two events r_C.
The choice of the cone cut parameters must be a compromise between a good background reduction rate and a good efficiency for cosmic rays. We find that $t_C = 5$ min and $r_C = 10°$ lead to reasonable results. 87,321 events (from which ∼45,000 events are contained in region one) survive this cut, i.e. the background is reduced by a factor of ∼150 and still 9 from initially 16 coincident events are contained in the data set.

8.5.3 Wavelet Similarity Cut

As a third filter, the wavelet similarity is used to reduce the data set further. We require a wavelet similarity of 12.3 which corresponds to a cosmic ray efficiency of 50%. This cut reduces the number of events in region one from ∼45,000 to 324, i.e. the background is reduced by a factor of 138 and six out of nine cosmic rays survive this cut.

To evaluate the cosmic ray similarity of the remaining events we use two indicators. As the dominant emission process is the geo-magnetic emission, the incoming directions of most of the remaining events should have angles perpendicular to the magnetic field of the earth. The histograms in figure 8.14 show the distributions of the sine of this angle α before and after the wavelet cut and the relative change of this distribution due to the wavelet similarity cut. The sine of α is used because the emission strength is proportional to $\sin(\alpha)$ (cf. eq. 2.9).

The relative change in the two distributions is calculated as follows:

$$\frac{H_{WaveletCut} - H_{all}}{H_{all}}, \tag{8.9}$$

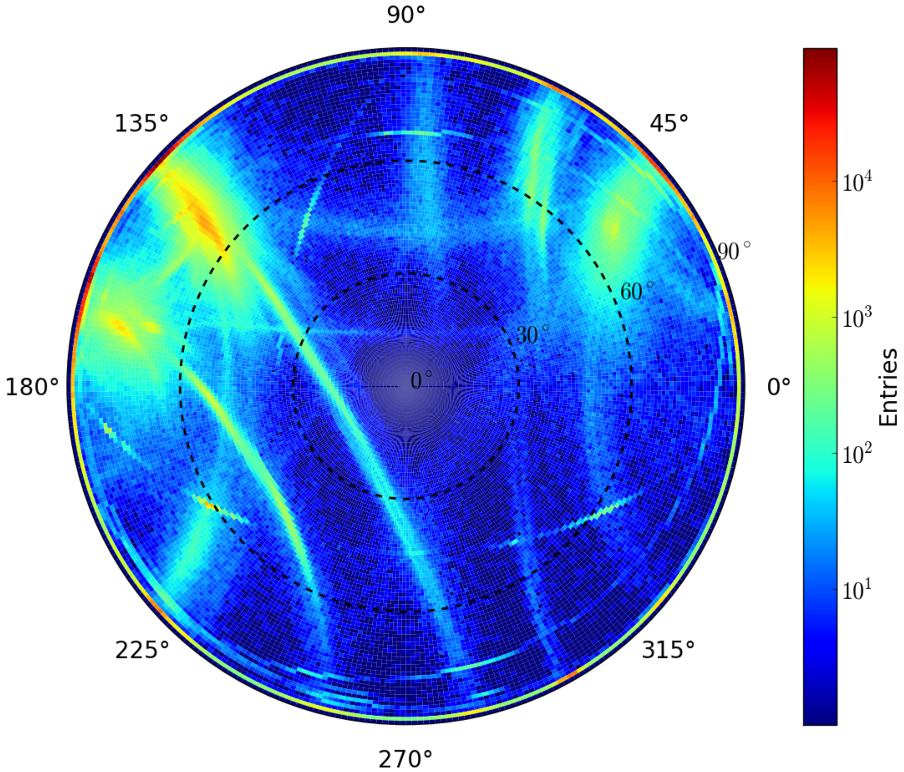

Figure 8.11: Skymap of all events that are rejected because of the geometry discriminator cut. The bow like structures are indeed due to stretched geometrical configuration of the triggered radio stations.

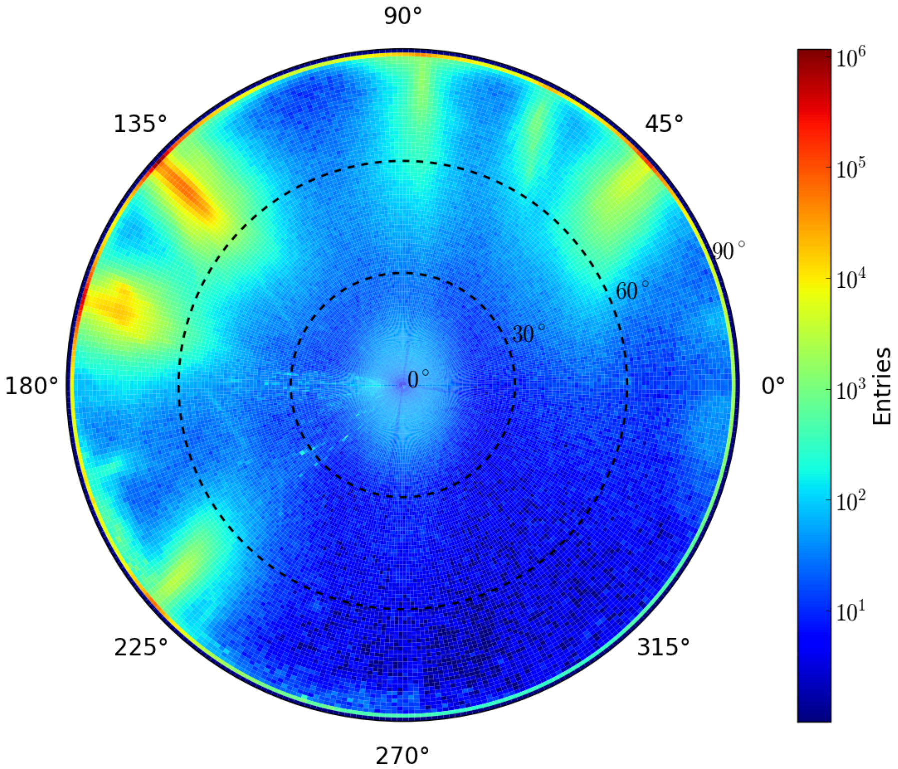

Figure 8.12: Skymap of all self-triggered events after the geometry discriminator cut. All bow like structures are removed whereas the smeared hotspots at the horizon are still visible.

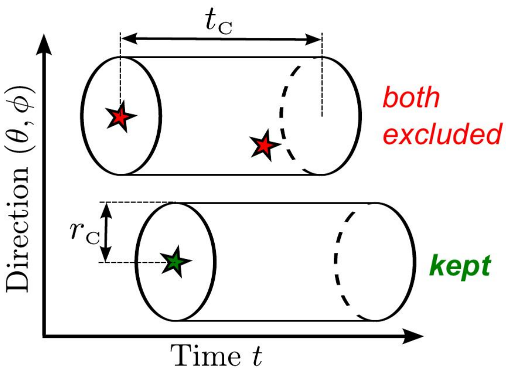

Figure 8.13: Sketch of the cone cut algorithm. Each event (star symbol) defines an angular region with a radius r_C and a length in time t_C counted from the time the signal was detected. If a second event falls into this space, both events are rejected. Only events that are separated in time and space are treated as candidates for air showers and kept for further analysis. Figure and caption taken from [5].

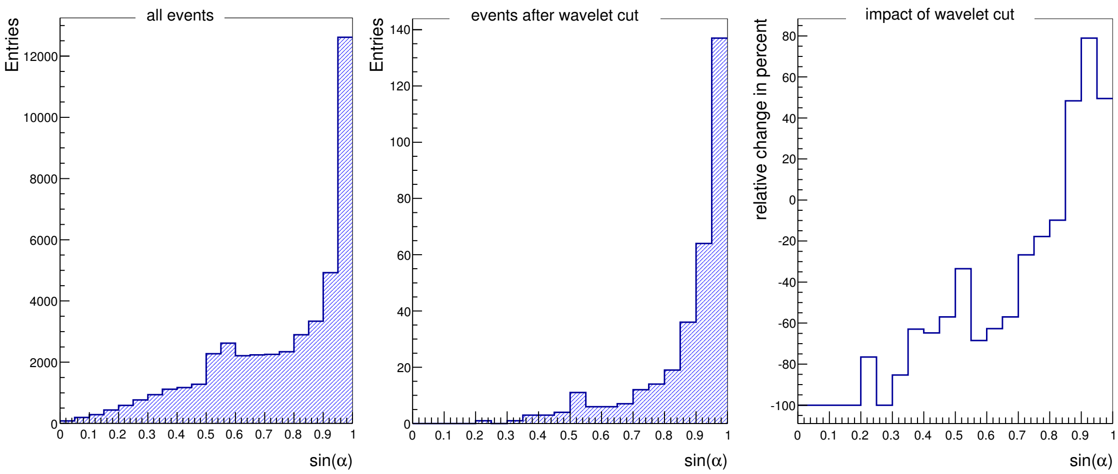

Figure 8.14: Sine of the angle between shower axis and magnetic field of the earth. (*left*) Distribution before the wavelet similarity cut. (*middle*) Distribution after the wavelet similarity cut. (*right*) Relative change of these distributions due to the wavelet similarity cut.

where $H_{WaveletCut}$ and H_{all} are the normalized histograms before and after the wavelet similarity cut.
Figure 8.14 right shows that after the wavelet similarity cut the number of events with incoming directions perpendicular to the earth's magnetic field is enhanced.

The second indicator is the Lorentz angle, i.e. the angle between the direction of the electric field vector and the Lorentz force acting on the particles of the air shower when traversing through the atmosphere. For cosmic rays a small Lorentz angle is expected (cf. chapter 6.4). Figure 8.15 shows the distribution of this angle before and after the wavelet similarity cut and the relative change in the two distributions. A significant increase of events with a small Lorentz angle is observed.

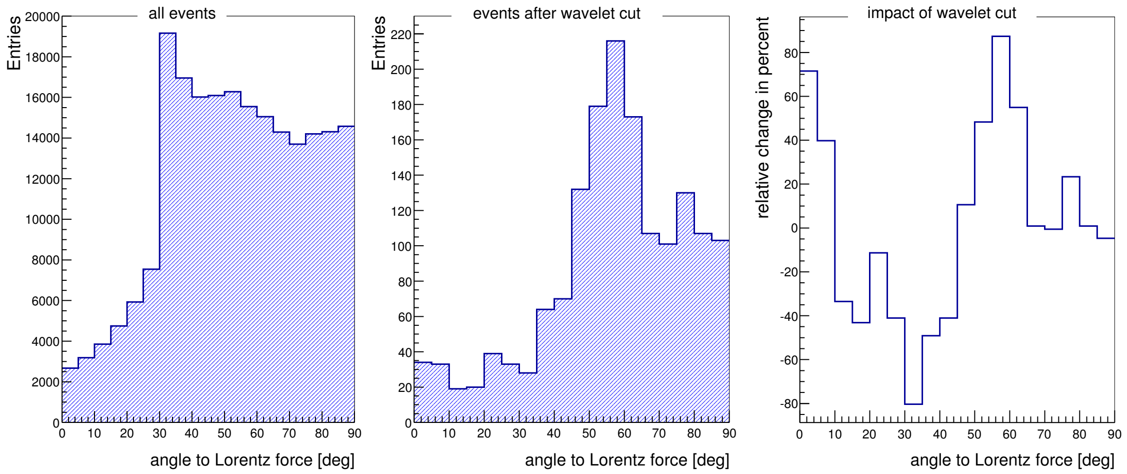

Figure 8.15: Impact of wavelet similarity cut on the Lorentz angle distribution. For cosmic rays a small Lorentz angle is expected. (*left*) Distribution before the wavelet similarity cut. Histogram contains 214,129 entries. This is more than the number of events because the Lorentz angle is determined for each station participating in an event. (*middle*) Distribution after wavelet similarity cut (1588 entries). (*right*) Relative change of the Lorentz angle distribution due to the wavelet similarity cut.

These two observations indicate that the remaining events are enhanced with cosmic rays. Furthermore, still six known cosmic ray events are present after the cut. The data set can be reduced further without loosing the known cosmic ray events by requiring an average Lorentz angle of less than 25° as proposed in a previous analysis [89]. After this cut 30 events remain. The arrival directions before and after this additional cut can be seen in the skyplots in figure 8.16 and 8.17.

The quality of this method can be judged by calculating the obtained cosmic ray efficiency and purity. The overall cosmic ray efficiency of this method is at least

$$\varepsilon \geq \frac{6}{16} \cong 38\,\% \,. \tag{8.10}$$

The cosmic ray efficiency of the wavelet similarity cut after the geometry cuts (geometry discriminator and cone cut) is at least

$$\varepsilon \geq \frac{6}{9} \cong 67\,\% \,. \tag{8.11}$$

The purity after all cuts is at least

$$\rho \geq \frac{6}{30} \cong 20\% \tag{8.12}$$

and without the last Lorentz angle cut

$$\rho \geq \frac{6}{324} \cong 2\,\% \,. \tag{8.13}$$

These numbers has to be related to the purity of the whole data set of $\rho \cong 16/25$ million $\cong 6.4\cdot 10^{-7}$ and the purity after the geometry cuts of $\rho \cong 9/45{,}000 \cong 0.02\%$.

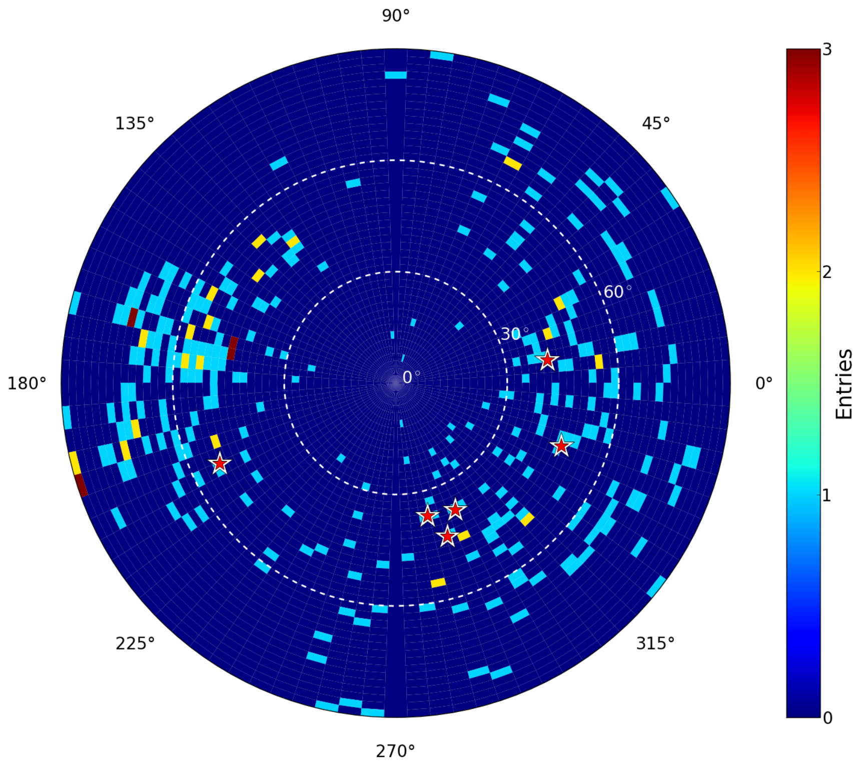

Figure 8.16: Skyplot of all events that survive the wavelet similarity cut. The red stars are the known cosmic ray events that are contained in this skyplot.

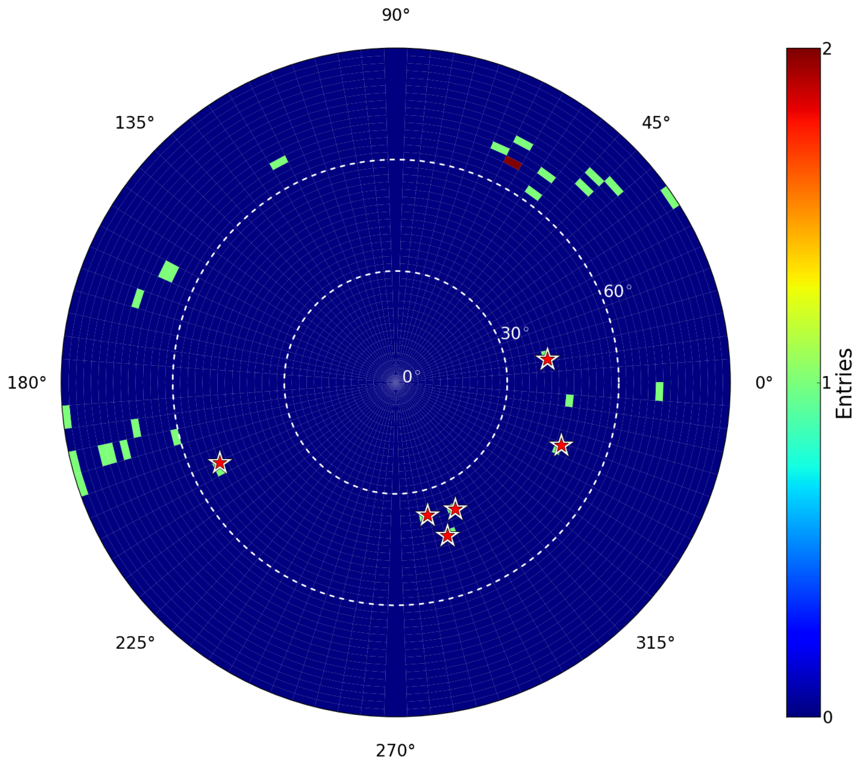

Figure 8.17: Skyplot of all events that survive the wavelet similarity cut and have an average Lorentz angle of smaller than 25°. The red stars are the known cosmic ray events that are contained in this skyplot.

9. Summary

The Pierre Auger Observatory (PAO) is a well calibrated hybrid cosmic ray detector consisting of 1600 Cherenkov surface detectors and 27 fluorescence telescopes. The measurement of the fluorescence light produced by an extensive air shower enables a direct measurement of the cosmic ray energy and is used to calibrate the surface detector. Thus, the PAO provides a perfect environment for the development and calibration of future detector technologies.

The Auger Engineering Radio Array (AERA) at the PAO currently consists of 21 self-triggered radio stations and is successfully operating since April 2011. Several tens of cosmic rays have been measured in coincidence with the surface detector. AERA is thoroughly calibrated through the entire signal chain, and modern station electronics enable the real time implementation of advanced trigger algorithms.

For the reconstruction of radio data, the modular software framework $\overline{\text{Off}}\underline{\text{line}}$ is used and developed further within this thesis. It provides advanced signal processing routines such as upsampling and noise filtering. A module to reconstruct the incoming direction of the air shower using different wave front models has been implemented. The knowledge of the incoming direction of the air shower combined with the well calibrated antennas enables the reconstruction of the three dimensional electric field at each radio station.

A method to simulate radio pulses with realistic noise background has been developed to determine the influence of noise on reconstructed quantities such as the signal amplitude. We determined a relation between the SNR of a measured radio pulse and the uncertainty of the signal strength and polarisation.

It is observed that the measured radio signals from extensive air showers exhibit a strong polarisation which can be explained by the geo-magnetic emission process. Small deviations from the geo-magnetic expectation that are not compatible within the uncertainties show that another second order emission process exists. The most favourable candidate for this process is the charge excess.

An estimator for the cosmic ray energy is further developed. To measure the cosmic ray energy, the radio signal has to be corrected for the incoming direction and the distance to the shower axis. The dominating geo-magnetic emission process implicates that the emission strength depends on the angle between the shower axis and the earth's magnetic field. Thus, the electric field amplitude is corrected for this effect. For the second correction, we interpolate the lateral signal falloff between the discrete data points using an exponential function with two free parameters. The dominating uncertainty is the position of the shower core which is obtained from the surface detector reconstruction. This uncertainty is taken into account using Monte Carlo technique.

We define the energy estimator as the corrected signal strength at a specific distance from the shower axis and find that a distance of 110 m leads to the best energy resolution for the current data set. Performing an energy calibration using the surface detector information, we observe that the defined radio energy estimator provides a linear dependency on the cosmic ray energy. The accuracy of the energy reconstruction with radio is determined to 31% including the surface detector resolution.

As a further contribution within this thesis, a new trigger strategy using wavelet technique is developed. The Morlet wavelet is used to expand the measured radio signal into its wavelet coefficients. In this basis each measured event is compared to the expectation for a cosmic ray signal which is obtained from the measured high quality cosmic ray radio events. By comparing the "wavelet similarity" of the known cosmic ray events to all self-triggered events of our data set we find that the background can be reduced by a factor of 79 for a cosmic ray efficiency of 50%. Thereby, the background reduction rate varies depending on the specific time and trigger settings.

For a measurement period with relatively good background reduction rate that also contains all known cosmic ray events, the wavelet trigger is used to find cosmic ray events. First, the background is reduced by geometry arguments. Then, a minimal "wavelet similarity" which corresponds to a cosmic ray efficiency of 50% is required. The distributions of the incoming direction and polarisation indicate that the resulting sample of 324 from former several million events is enriched with cosmic rays. By examining the known cosmic ray events we can set lower limits on the achieved efficiency and purity. The overall cosmic ray efficiency is at least 38% at a purity of the sample of at least 2%. The purity can be improved further by an additional cut on the polarisation to at least 20% without loosing cosmic ray efficiency.

A. Appendix

A.1 Influence of Thunderstorms on Radio Emission

During thunderstorms, strong electric fields are present in the atmosphere. These electric fields lead to an additional amplification or an attenuation of the radio pulse from extensive air showers depending on the geometry of the air shower and the atmospheric electric fields (see fig. A.1 for an illustration) [87, 97]. Thereby, usually only the events that experience an amplification can be measured because, otherwise, the radio signal gets too low to be detectable. Furthermore, the polarisation of the radio signal is to be altered by the presence of additional electric fields in the atmosphere.

Thunderstorms can be detected by monitoring the atmospheric electric field on ground level. At the Central Radio Station at the AERA site, the atmospheric electric field is continuously monitored. The algorithm described in [86, chapter 3.3.2] - which was already used at LOPES - is used to find thunderstorms. For all cosmic ray radio events, the atmospheric electric field data is analysed to check whether it was recorded during a thunderstorm or not. In our cosmic ray data set, two events were identified as thunderstorm events. Figure A.2 shows the development of the atmospheric electric field 15 minutes before one of the cosmic ray radio events that has been identified as thunderstorm event.

Both thunderstorm events show a very clear signal in all triggered radio stations and a nice lateral signal falloff (cf. fig. A.3) but the polarisation of the radio pulse differ

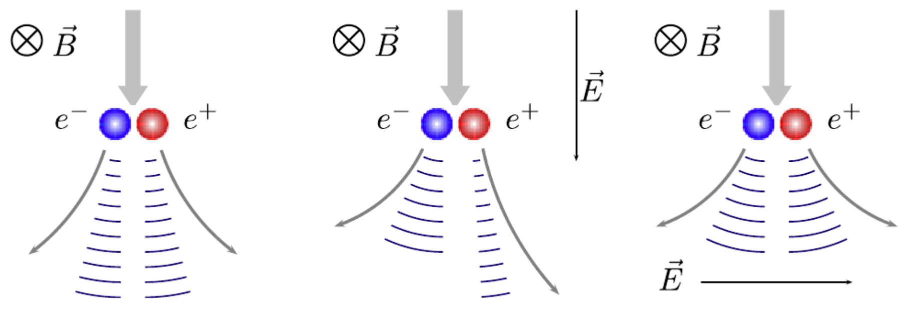

Figure A.1: (*left*) Normal shower development. (*middle*) and (*right*) Influence of atmospheric electric fields on the shower development. Figure taken from [97].

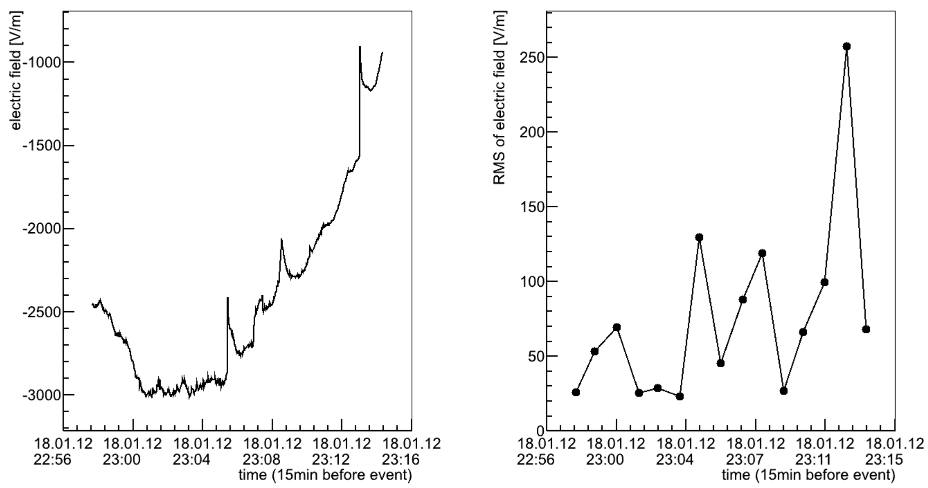

Figure A.2: Atmospheric electric field (left) and RMS of the atmospheric electric field (calculated over one minute) (right) measured at the Central Radio Station 15 minutes before the radio event 39992.

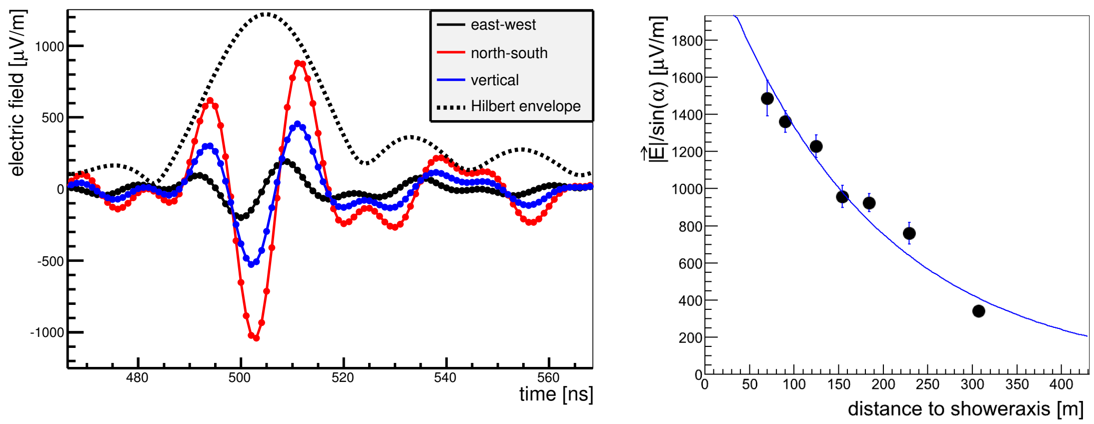

Figure A.3: (*left*) Radio pulse of event no. 39992 that has been measured during a thunderstorm. The radio pulse is clearly visible. (*right*) Lateral signal distribution of this event.

completely from the expectation for cosmic ray radio pulses. The Lorentz angle is almost 90° in all participating stations (cf. fig. A.3right, the expectation for cosmic rays is a Lorentz angle close to zero cf. fig. 6.14 right).

Figure A.4 right shows that the estimated energy, using the radio energy estimator, is much higher (almost one order of magnitude) then the cosmic ray energy reconstructed by the surface detector. As the energy estimator scales approximately linear with the signal strength, the measured radio signal is almost one order of magnitude higher than it should be.

From these two observations we conclude that thunderstorms strongly influence the radio emission from extensive air showers. In the case of these two events the radio signal has been amplified strongly by the additional electric fields in the atmosphere.

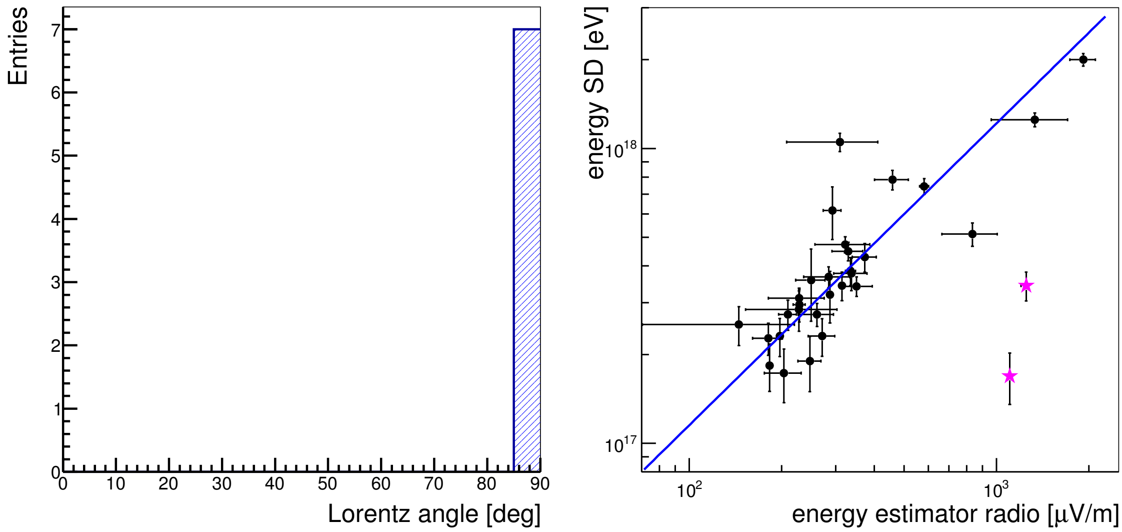

Figure A.4: (*left*) Lorentz angle of event 39992. All stations exhibit a polarisation exactly opposite to the cosmic ray expectation. (*right*) Energy calibration of the radio energy estimator with the energy information from the surface detector. The two events recorded during a thunderstorm (star) show a clear overestimation of the cosmic ray energy.

A.2 Additional Plots

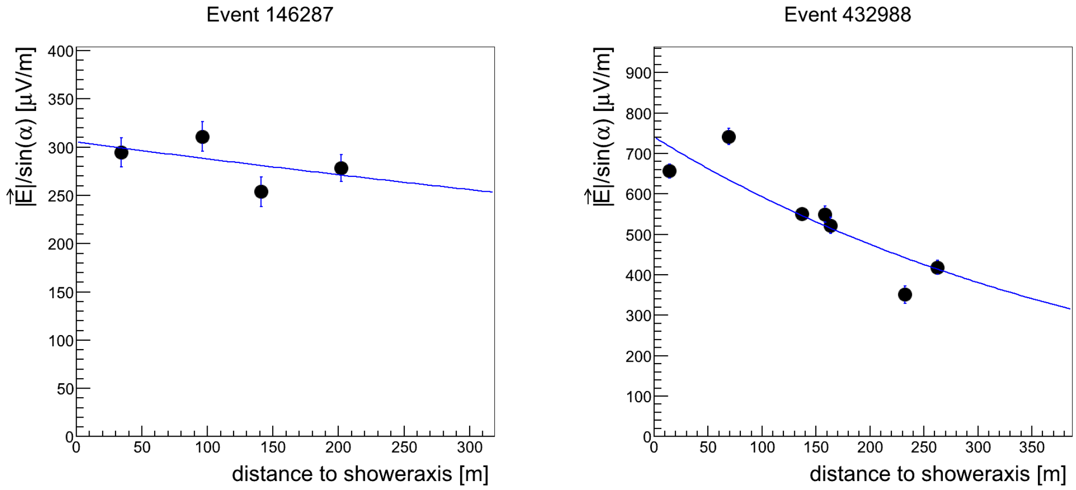

Figure A.5: Two examples of the lateral signal falloff and interpolation with an exponential function.

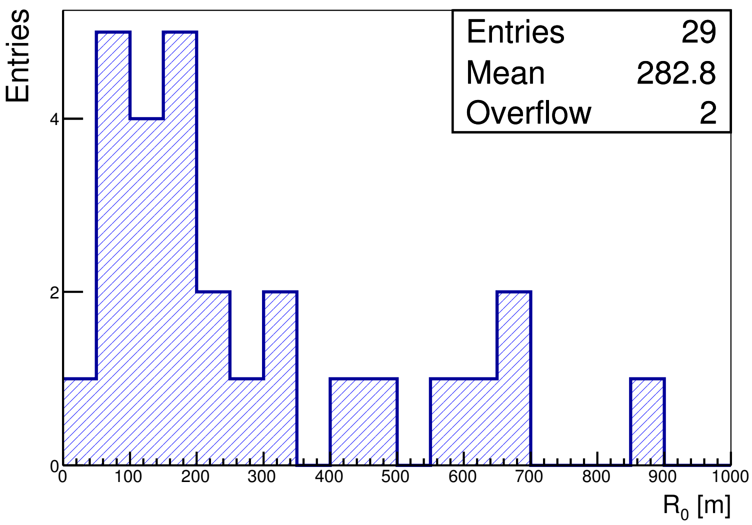

Figure A.6: Histogram of slope parameters of the exponential function (cf. eq. 7.1) used to interpolate the lateral signal falloff. This histogram contains two events in the overflow bin $R_0 = 1534$ m and $R_0 = 10,000$ m.

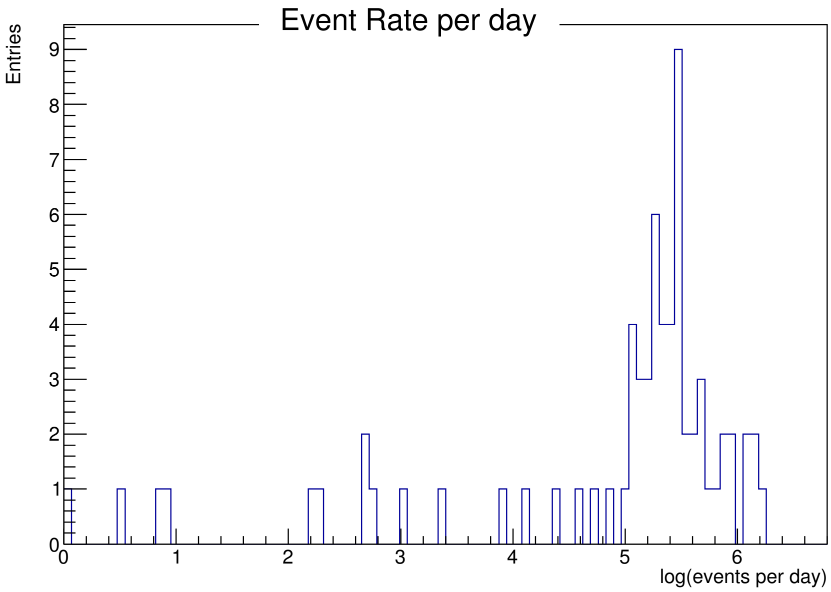

Figure A.7: Events rate of the self-triggered data set AERA21.

References

[1] L. Evans P. Bryant. *LHC Machine*. Journal of Instrumentation, 3(08): p. 8001 (2008). doi:10.1088/1748-0221/3/08/S08001.

[2] V. Hess. *Über Beobachtungen der durchdringenden Strahlung bei sieben Freiballonfahrten*. Physik. Zeitschriften, XIII: pp. 1084–1091 (1912).

[3] P. Auger, P. Ehrenfest, R. Maze, J. Daudin R. A. Fréon. *Extensive Cosmic-Ray Showers*. Rev. Mod. Phys., 11: pp. 288–291 (1939). doi:10.1103/RevModPhys.11.288.

[4] W. Kolhörster, I. Matthes E. Weber. *Gekoppelte Höhenstrahlen*. Naturwissenschaften, 26: pp. 576–576 (1938). doi:10.1007/BF01773491.

[5] S. Fliescher. *Antenna Devices and Measurement of Radio Emission from Cosmic Ray induced Air Showers at the Pierre Auger Observatory*. Ph.D. thesis, RWTH Aachen University (2011).

[6] P. Marrocchesi. *Future balloon experiments for electron and positron measurements at high energy*. Nucl. Instrum. Methods Phys. Res., Sect. A, 630(1): pp. 296 – 300 (2011). doi:10.1016/j.nima.2010.06.087. Proceedings of the 2nd RICAP conference 2009, Rome Italy.

[7] M. Casolino P. Picozza. *The PAMELA experiment: A space-borne observatory for heliospheric phenomena*. Advances in Space Research, 41(12): pp. 2043 – 2049 (2008). doi:10.1016/j.asr.2007.06.061.

[8] S. Gentile for the AMS-02 Collaboration. *The Alpha Magnetic Spectrometer on the International Space Station* (2003). Proceedings of the 28th ICRC, Tsukuba Japan.

[9] P. K. F. Grieder. *Extensive Air Showers - High Energy Phenomena and Astrophysical Aspects*, vol. 1. Springer (2010). doi:10.1016/B978-044450710-5/50003-8.

[10] P. Abreu, M. Aglietta, E. J. Ahn et al. *The Pierre Auger Observatory I: The Cosmic Ray Energy Spectrum and Related Measurements*. Proceedings of 32nd ICRC 2011, Beijing China. arxiv:1107.4809.

[11] K. Greisen. *End to the cosmic ray spectrum?* Phys. Rev. Lett., 16(17): pp. 748–750 (1966). doi:10.1103/PhysRevLett.16.748.

[12] G. Zatsepin V. Kuzmin. *Upper Limit of the Spectrum of Cosmic Rays*. JETP Lett., 4: pp. 78–80 (1966).

[13] T. Stanev, R. Engel, A. Mücke, R. J. Protheroe J. P. Rachen. *Propagation of ultrahigh energy protons in the nearby universe.* Phys. Rev. D, 62: p. 093005 (2000). doi:10.1103/PhysRevD.62.093005.

[14] E. Khan, S. Goriely, D. Allard et al. *Photodisintegration of ultra-high-energy cosmic rays revisited.* Astroparticle Physics, 23(2): pp. 191 – 201 (2005). doi: 10.1016/j.astropartphys.2004.12.007.

[15] J. W. Cronin. *Cosmic rays: the most energetic particles in the universe.* Review of Modern Physics, 71: pp. 165–172 (1999). doi:10.1103/RevModPhys.71.S165.

[16] K. Nakamura P. D. Group. *Review of Particle Physics.* J. Phys. G: Nucl. Part. Phys., 37(7A): p. 075021 (2010). doi:10.1088/0954-3899/37/7A/075021.

[17] T. Antoni, W. Apel, A. Badea et al. *KASCADE measurements of energy spectra for elemental groups of cosmic rays: Results and open problems.* Astropart. Phys., 24(1-2): pp. 1 – 25 (2005). doi:10.1016/j.astropartphys.2005.04.001.

[18] W. Apel, J. Arteaga, A. Badea et al. *Energy spectra of elemental groups of cosmic rays: Update on the KASCADE unfolding analysis.* Astropart. Phys., 31(2): pp. 86 – 91 (2009). doi:10.1016/j.astropartphys.2008.11.008.

[19] W. D. Apel, J. C. Arteaga-Velázquez, K. Bekk et al. *Kneelike Structure in the Spectrum of the Heavy Component of Cosmic Rays Observed with KASCADE-Grande.* Phys. Rev. Lett., 107: p. 171104 (2011). doi:10.1103/PhysRevLett.107.171104.

[20] J. Abraham, P. Abreu, M. Aglietta et al. *Measurement of the Depth of Maximum of Extensive Air Showers above* 10^{18} eV. Phys. Rev. Lett., 104: p. 091101 (2010). doi:10.1103/PhysRevLett.104.091101.

[21] J. Blümer, R. Engel J. R. Hörandel. *Cosmic rays from the knee to the highest energies.* Progress in Particle and Nuclear Physics, 63(2): pp. 293 – 338 (2009). doi:10.1016/j.ppnp.2009.05.002.

[22] E. Fermi. *On the Origin of the Cosmic Radiation.* Phys. Rev., 75: pp. 1169–1174 (1949). doi:10.1103/PhysRev.75.1169.

[23] D. F. Torres L. A. Anchordoqui. *Astrophysical origins of ultrahigh energy cosmic rays.* Reports on Progress in Physics, 67(9): p. 1663 (2004). doi:10.1088/0034-4885/67/9/R03.

[24] A. M. Hillas. *The Origin of Ultra-High-Energy Cosmic Rays.* Annual review of astronomy and astrophysics, 22: pp. 425–444 (1984).

[25] M. Actis, G. Agnetta, F. Aharonian et al. *Design concepts for the Cherenkov Telescope Array CTA: an advanced facility for ground-based high-energy gamma-ray astronomy.* Experimental Astronomy, 32: pp. 193–316 (2011). doi:10.1007/s10686-011-9247-0.

[26] T. Gaisser A. Hillas. Proceedings of the 15th ICRC (1977).

[27] K. Kamata J. Nishimura. *The Lateral and the Angular Structure Functions of Electron Showers*. Prog. Theor. Phys. Supp., 6: pp. 93–155 (1958). doi: 10.1143/PTPS.6.93.

[28] K. Greisen. *Progress in Cosmic Ray Physics*. vol III , North-Holland Publishing Company, Amsterdam (1965).

[29] M. A. Lawrence, R. J. O. Reid A. A. Watson. *The cosmic ray energy spectrum above* $4{\cdot}10^{17}$ *eV as measured by the Haverah Park array*. J. Phys. G: Nucl. Part. Phys., 17(5): p. 733 (1991). doi:10.1088/0954-3899/17/5/019.

[30] T. Antoni, W. Apel, F. Badea et al. *The cosmic-ray experiment KASCADE*. Nucl. Instrum. Methods Phys. Res., Sect. A, 513(3): pp. 490 – 510 (2003). doi:10.1016/S0168-9002(03)02076-X.

[31] I. Allekotte, A. Barbosa, P. Bauleo et al. *The surface detector system of the Pierre Auger Observatory*. Nucl. Instrum. Methods Phys. Res., Sect. A, 586(3): pp. 409 – 420 (2008). doi:10.1016/j.nima.2007.12.016.

[32] J. Jelley. *Cerenkov radiation in the atmosphere and its application to the study of extensive air showers*. Il Nuovo Cimento (1955-1965), 8: pp. 578–584 (1958). doi:10.1007/BF02962576.

[33] G. Askaryan. *Excess negative charge of an electron-photon shower*. Sov. Phys. JETP, 14: p. 441 (1962).

[34] J. V. Jelley, J. H. Fruin, N. A. Porter et al. *Radio Pulses from Extensive Cosmic-Ray Air Showers*. Nature, 205(4969): pp. 327 – 328 (1965). doi:10.1038/205327a0.

[35] H. R. Allan, R. W. Clay J. K. Jones. *Radio Pulses from Extensive Air Showers*. Nature, 227: pp. 1116–1118 (1970). doi:10.1038/2271116a0.

[36] H. Allan. *Radio Emission from Extensive Air Showers*. Progress in elementary particle and cosmic ray physics, North-Holland Publishing, X: pp. 171–302 (1971).

[37] T. Huege, W. Apel, J. Arteaga et al. *The LOPES experiment - Recent results, status and perspectives*. Nucl. Instrum. Methods Phys. Res., Sect. A, 662, Supplement 1(0): pp. 72 – 79 (2012). doi:10.1016/j.nima.2010.11.081. Proceedings of the 4th ARENA workshop, Nantes France.

[38] O. Ravel for the Pierre Auger Collaboration. *The CODALEMA experiment*. Nucl. Instrum. Methods Phys. Res., Sect. A, 662, Supplement 1(0): pp. S89 – S94 (2012). doi:10.1016/j.nima.2010.12.057. Proceedings of the 4th ARENA workshop, Nantes France.

[39] W. D. Apel, J. C. Arteaga, L. Bähren et al. *Experimental evidence for the sensitivity of the air-shower radio signal to the longitudinal shower development.* Phys. Rev. D, 85: p. 071101 (2012). doi:10.1103/PhysRevD.85.071101.

[40] H. Schoorlemmer. *Polarization of Radio Showers.* Ph.D. thesis, Radboud University Nijmegen (2012).

[41] H. Falcke P. Gorham. *Detecting radio emission from cosmic ray air showers and neutrinos with a digital radio telescope.* Astropart. Phys., 19(4): pp. 477 – 494 (2003). doi:10.1016/S0927-6505(02)00245-1.

[42] D. Ardouin, A. Belletoile, C. Berat et al. *Geomagnetic origin of the radio emission from cosmic ray induced air showers observed by CODALEMA.* Astropart. Phys., 31(3): pp. 192 – 200 (2009). doi:10.1016/j.astropartphys.2009.01.001.

[43] B. Revenu for the Pierre Auger Collaboration. *Radio detection of cosmic ray air showers by the RAuger experiment, a fully autonomous and self-triggered system installed at the Pierre Auger Observatory.* Nucl. Instrum. Methods Phys. Res., Sect. A, 662, Supplement 1: pp. 130 – 133 (2012). doi:10.1016/j.nima.2010.11.087. Proceedings of 4th ARENA workshop 2010, Nantes France.

[44] P. W. Gorham, N. G. Lehtinen, G. S. Varner et al. *Observations of microwave continuum emission from air shower plasmas.* Phys. Rev. D, 78: p. 032007 (2008). doi:10.1103/PhysRevD.78.032007.

[45] R. Engel. *GHz detection activities for air showers: Experiments, axxelerator measurementes, theory.* 5th ARENA workshop 2012, Erlangen Germany.

[46] P. S. Allison for the Pierre Auger Collaboration. *Microwave detection of cosmic ray showers at the Pierre Auger Observatory* (2011). Proceedings of the 32nd ICRC, Beijing China.

[47] R. Smida. *Cosmic-Ray Observation via Microwave Emission (CROME).* 5th ARENA workshop 2012, Erlangen Germany.

[48] F. Werner. *On the microwave signal of air showers measured with CROME.* 5th ARENA workshop 2012, Erlangen Germany.

[49] S. Fliescher for the Pierre Auger Collaboration. *Radio detection of cosmic ray induced air showers at the Pierre Auger Observatory.* Nucl. Instrum. Methods Phys. Res., Sect. A, 662, Supplement 1: pp. 124 – 129 (2012). doi:10.1016/j.nima.2010.11.045. Proceedings of 4th ARENA workshop 2010, Nantes France.

[50] B. Keilhauer. *Investigation of Atmospheric Effects on the Development of Extensive Air Showers and their Detection with the Pierre Auger Observatory.* Ph.D. thesis, Karlsruhe Institute of Technology (2004).

[51] B. M. Bolotovskii. *Vavilov – Cherenkov radiation: its discovery and application.* Physics-Uspekhi, 52(11): p. 1099 (2009). doi:10.3367/UFNe.0179.200911c.1161.

[52] J. Abraham, P. Abreu, M. Aglietta et al. *Trigger and aperture of the surface detector array of the Pierre Auger Observatory*. Nucl. Instrum. Methods Phys. Res., Sect. A, 613(1): pp. 29 – 39 (2010). doi:10.1016/j.nima.2009.11.018.

[53] C. Bonifazi. *The angular resolution of the Pierre Auger Observatory*. Nucl. Phys. B, Proc. Suppl., 190(0): pp. 20 – 25 (2009). doi:10.1016/j.nuclphysbps.2009.03.063. Proceedings of the Cosmic Ray International Seminars.

[54] J. Abraham, P. Abreu, M. Aglietta et al. *The fluorescence detector of the Pierre Auger Observatory*. Nucl. Instrum. Methods Phys. Res., Sect. A, 620(2-3): pp. 227 – 251 (2010). doi:10.1016/j.nima.2010.04.023.

[55] B. R. Dawson for the Pierre Auger Collaboration. *Hybrid Performance of the Pierre Auger Observatory*. Proceedings of 30th ICRC 2007, Merida Mexico. arxiv:0706.1105.

[56] M. Mostafa for the Pierre Auger Collaboration. *Atmospheric Monitoring for the Pierre Auger Fluorescence Detector*. Proceedings of 28th ICRC 2003, Tsukuba Japan. arxiv:astro-ph/0308442.

[57] F. Kakimoto, E. Loh, M. Nagano et al. *A measurement of the air fluorescence yield*. Nucl. Instrum. Methods Phys. Res., Sect. A, 372(3): pp. 527 – 533 (1996). doi:10.1016/0168-9002(95)01423-3.

[58] M. Nagano, K. Kobayakawa, N. Sakaki K. Ando. *New measurement on photon yields from air and the application to the energy estimation of primary cosmic rays*. Astropart. Phys., 22(3-4): pp. 235 – 248 (2004). doi:10.1016/j.astropartphys.2004.08.002.

[59] R. Pesce for the Pierre Auger Collaboration. *Energy calibration of data recorded with the surface detectors of the Pierre Auger Observatory: an update*. Proceedings of 32nd ICRC 2011, Beijing China. arxiv:1107.4809.

[60] D. Newton, J. Knapp A. Watson. *The optimum distance at which to determine the size of a giant air shower*. Astropart. Phys., 26(6): pp. 414 – 419 (2007). doi:10.1016/j.astropartphys.2006.08.003.

[61] P. Abreu, M. Aglietta, E. J. Ahn et al. *The Pierre Auger Observatory V: Enhancements*. Proceedings of 32nd ICRC 2011, Beijing China. arxiv:1107.4807.

[62] J. Kelley for the Pierre Auger Collaboration. *AERA: the Auger Engineering Radio Array*. Proceedings of 32nd ICRC 2011, Beijing China. arxiv:1107.4807.

[63] K. Weidenhaupt. *LPDA-Antennas for Large Scale Radio Detection of Cosmic Rays at the Pierre-Auger-Observatory*. Diploma Thesis (2009). RWTH Aachen University.

[64] M. Erdmann, S. Fliescher, B. Philipps K. Weidenhaupt. *Antenna Alignment for the first 24 Stations of AERA*. GAP-2010-083 (2010). Internal note of the Pierre Auger Observatory.

[65] T. P. A. Collaboration, D. Charrier L. Denis. *Antennas for Waveform Detection of Coherent Radio Emission from Cosmic Ray induced Air Showers at the Pierre Auger Obervatory*. Submitted to Journal of Instrumentation (2011).

[66] M. Stephan. *Design and Test of a Low Noice Amplifier for the Auger Radio Detector*. Diploma Thesis (2009). RWTH Aachen University.

[67] M. Stephan for the Pierre Auger Collaboration. *Antennas, Filters and Preamplifiers designed for the Radio Detection of Ultra-High-Energy Cosmic Rays*. Proceedings of Asia-Pacific Microwave Conference, TH3G-49 (2010).

[68] J. L. Kelley for the Pierre Auger Collaboration. *Data Acquisition, Triggering, and Filtering at the Auger Engineering Radio Array*. Proceedings of the Very Large Volume Neutrino Telescope Workshop 2011, Erlangen Germany.

[69] Z. Szadkowski, E. Fraenkel A. M. van den Berg. *FPGA/NIOS implementation of an adaptive FIR filter using linear prediction to reduce narrow-band RFI for radio detection of cosmic rays* (2012). Proceedings of the IEEE-NPSS Real Time Conference, Berkeley USA.

[70] A. Nelles, K. Weidenhaupt, J. Kelley et al. *A Survey of Narrowband and Broadband Radio-frequency Interference at AERA*. GAP-2011-062 (2011). Internal note of the Pierre Auger Observatory.

[71] J. Kelley C. Timmermans. *Calibration of the AERA Phase 1 Digitizer*. GAP-2011-028 (2011). Internal note of the Pierre Auger Observatory.

[72] G. Burke A. Poggio. *Numerical Electromagnetics Code (NEC) method of moments, parts I,II,III*. Tech. rep., Lawrence Livermore National Laboratory (1983).

[73] O. Seeger. *Absolute Clibration of the Small Black Soider Antenna for the Pierre Auger Observatory*. Diploma Thesis (2010). RWTH Aachen University.

[74] Rohde Schwarz. *Handheld Spectrum Analyzer 100 kHz to 3.6 GHz with preamplifier, tracking generator and internal VSWR bridge*. FSH4 (model 24).

[75] S. Argiro, S. Barroso, J. Gonzalez et al. *The offline software framework of the Pierre Auger Observatory*. Nucl. Instrum. Methods Phys. Res., Sect. A, 580(3): pp. 1485 – 1496 (2007). doi:10.1016/j.nima.2007.07.010.

[76] T. P. A. Collaboration, P. Abreu, M. Aglietta et al. *Advanced functionality for radio analysis in the Offline software framework of the Pierre Auger Observatory*. Nucl.Instrum.Meth.A, 635:92-102,2011 (2011). doi:10.1016/j.nima.2011.01.049.

[77] I. Antcheva, M. Ballintijn, B. Bellenot et al. *ROOT - A C++ framework for petabyte data storage, statistical analysis and visualization*. Comput. Phys. Commun., 180(12): pp. 2499 – 2512 (2009). doi:10.1016/j.cpc.2009.08.005.

[78] R. U. Ioana C. Maris, Fabian Schuessler M. Unger. *Data Summary Trees and Shower Visualization for Reconstructed Auger Events*. GAP-2006-081 (2006). Internal note of the Pierre Auger Observatory.

[79] C. Shannon. *Communication in the Presence of Noise*. Proceedings of the IRE, 37(1): pp. 10 – 21 (1949). doi:10.1109/JRPROC.1949.232969.

[80] A. V. Oppenheim R. W. Schafer. *Discrete-Time Signal Processing*. Prentice Hall, 2nd edition ed. (1999).

[81] T. Asch. *Self-Triggering of Radio Signals from Cosmic Ray Air Showers*. Ph.D. thesis, Forschungszentrum Karlsruhe (2009).

[82] B. Boashash. *Estimating and interpreting the instantaneous frequency of a signal. I. Fundamentals*. Proceedings of the IEEE, 80(4): pp. 520 –538 (1992). doi:10.1109/5.135376.

[83] L. Mohrmann. *Measurement of Radio Emission from Cosmic Ray induced Air Showers at the Pierre Auger Observatory with a Spherical Wave Reconstruction*. Master's thesis, RWTH Aachen (2011).

[84] F. Schröder. *Instruments and Methods for the Radio Detection of High Energy Cosmic Rays*. Ph.D. thesis, Fakultät für Physik Institut für Kernphysik (IKP) (2011).

[85] *Top 500 Supercomputers*. http://www.top500.org.

[86] S. Nehls. *Calibrated Measurements of the Radio Emission of Cosmic Ray Air Showers*. Ph.D. thesis, Institut für Kernphysik, Universität Karlsruhe (2008).

[87] M. Enders for the Pierre Auger Collaboration. *Radio Emission of Extensive Air Showers during Thunderstorms*. Proceedings of the 31st ICRC, Lodz Poland (2009).

[88] F. Schroeder, W. Apel, J. Arteaga et al. *On noise treatment in radio measurements of cosmic ray air showers*. Nucl. Instrum. Methods Phys. Res., Sect. A, 662, Supplement 1(0): pp. S238 – S241 (2012). doi:10.1016/j.nima.2010.11.009. Proceedings of the 4th ARENA workshop, Nantes France.

[89] M. Erdmann, S. Fliescher, L. Mohrmann K. Weidenhaupt. *A Novel Method of Selecting Cosmic Ray Candidates*. GAP-2011-108 (2011). Internal note of the Pierre Auger Observatory.

[90] K. Weidenhaupt for the Pierre Auger Collaboration. *The Auger Engineering Radio Array* (2012). Proceedings of the Vulcano Workshop, 28. May - 2. June 2012, Vulcano Italy.

[91] A. Nelles. *Measuring Cosmic Rays with LOFAR*. 5th ARENA workshop 2012, Erlangen Germany.

[92] I. Sidelnik, D. Melo, A. Tapia et al. *Infill reconstruction using the Auger Offline Software*. GAP-2011-013 (2011). Internal note of the Pierre Auger Observatory.

[93] T. Huege, R. Ulrich R. Engel. *Dependence of geosynchrotron radio emission on the energy and depth of maximum of cosmic ray showers*. Astropart. Phys., 30(2): pp. 96 – 104 (2008). doi:10.1016/j.astropartphys.2008.07.003.

[94] S. Knurenko, V. Kozlov, Z. Petrov M. Pravdin. *Experimental results of radio observations at the Yakutsk EAS in 2009-2011* (2012). Proceedings of the ECRS, Moskov Russia.

[95] C. Glaser for the Pierre Auger Collaboration. *Energy Estimation for Cosmic Rays Measured with the Auger Engineering Radio Array*. 5th ARENA workshop 2012, Erlangen Germany.

[96] D. Jordan, R. W. Miksad E. J. Powers. *Implementation of the continuous wavelet transform for digital time series analysis*. Rev. Sci. Instrum., 68(3): pp. 1484–1494 (1997). doi:10.1063/1.1147636.

[97] W. Apel, J. Arteaga, L. Bähren et al. *Thunderstorm observations by air-shower radio antenna arrays*. Advances in Space Research, 48(7): pp. 1295 – 1303 (2011). doi:10.1016/j.asr.2011.06.003.

Erklärung

Hiermit versichere ich, dass ich diese Arbeit einschließlich beigefügter Zeichnungen, Darstellungen und Tabellen selbstständig angefertigt und keine anderen als die angegebenen Hilfsmittel und Quellen verwendet habe. Alle Stellen, die dem Wortlaut oder dem Sinn nach anderen Werken entnommen sind, habe ich in jedem einzelnen Fall unter genauer Angabe der Quelle deutlich als Entlehnung kenntlich gemacht.

Aachen, den 23. August 2012

Christian Glaser